Design, Modeling, and Control of an Active Prosthetic Knee

By

Roozbeh Borjian

A thesis

presented to the University of Waterloo

in fulfillment of the

thesis requirement for the degree of

Master of Applied Science

in

Mechanical Engineering

Waterloo, Ontario, Canada, 2008

AUTHOR'S DECLARATION

I hereby declare that I am the sole author of this thesis. This is a true copy of the thesis, including any required final revisions, as accepted by my examiners.

I understand that my thesis may be made electronically available to the public.

Roozbeh Borjian

ABSTRACT

The few microcontroller based active/semi-active prosthetic knee joints available commercially are extremely expensive and do not consider the uncertainties of inputs sensory information. Progressing in the controller of the current prosthetic devices and creating artificial lower limbs compatible with different users may lead to more effective and low-cost prostheses. This can affect the life style of lots of amputees specially the land-mine victims in developing war-torn countries who are unable to partake in the advancement of the current intelligent prosthetic knees. The purpose of the proposed Active Prosthetic Knee (APK) design is to investigate a new schema that allows the device to provide the full necessary torque at the knee joint based on echoing the state of the intact leg. This study involves the design features of the mechanical aspects, sensing system, communication, and knowledge-based controller to implement a cost-effective APK. The proposed microcontroller based prosthesis utilizes a ball screw system accompanied by a high-speed brushed servomotor to provide one degree of freedom for the fabricated prototype. Moreover, a modular test-bed is manufactured to mimic the lower limb motion which contributes investigating different controllers for the prototype. Thus, the test bed allows assessing the primary performance of the APK before testing on a human subject. Different types of sensing systems (electromyography and lower limb inclination angles) are investigated to extract signals from the user's healthy leg and send the captured data to the APK controller. The methodology to measure each type of signal is described, and comparison analyses are provided. Wireless communication between the sensory part and actuator is established. A knowledge-based control mechanism is developed that takes advantage of an Adaptive-Network-based Fuzzy Inference System (ANFIS) to determine knee torque as a function of the echoing angular state of the able leg considering the uncertainty of inputs. Therefore, the developed controller can make the APK serviceable for different users. The fuzzy membership function's parameters and rules define the knowledge-base of the system. This knowledge is based on existing experience and known facts about the walking cycle.

ACKNOWLEDGMENTS

I would like to express my gratitude towards my supervisor Dr. Behrad Khamesee for allowing me to engage in this project, and for his guidance in exploring new ideas and new challenges. He gave me the courage and self confidence to explore and conduct research.

I would also like to acknowledge the contribution of Dr. William Melek and his guidance and kind answers in responding to any questions that I posed to him.

I would also like to acknowledge Prof. John Medley not only for taking the time to review my thesis and giving me advantageous feedback, but also for his effort to provide financial support for me during my master program. Without his support this work would not have been possible. I must also express my appreciation to Arthur F. Church for his donation.

I would like to thank all those who contributed to this work. Thanks to my colleague, James Lim, for his support for the past two years. James was not only my colleague in this project, but also he is a really good friend of mine. A great deal of this research is inspired and made possible through the teamwork of undergraduate students in the last year. I am also grateful for the help provided by Robert Wagner in setting up our system hardware.

I also appreciate the support that all my friends, especially Ehsan Shameli, Babak Ebrahimi, and Mohammad BiglarBegian gave me for the last two years. I would like to thank Soroosh Hassanpur for reading my thesis and helping me to edit it.

I would like also thank Lida Ashrafi for her patience and dedication during past years.

DEDICATION

This thesis is dedicated to

My Parents

and

in loving memory of
Shahrooz and Shirin

TABLE OF CONTENTS

LIST OF FIGURES

LIST OF TABLES

Chapter 1

INTRODUCTION

In the past, the only resources available for the people who lost their lower limb were walkers, wheelchairs, wooden pegleg, and crutches. However, nowadays, people with this form of disability can take the advantages of advances in medical science and technology by using lower limb motorized prosthetic.

Leg and knee play crucial roles in the body. Leg contributes to keep the body balanced and supported while standing up. Knee locomotion joins the upper and lower legs together and provides the bending motion that allows us to walk.

The few microcontroller based active/semi-active prosthetic knee joints available commercially, such as Otto Bock's prosthetic C-Leg, are extremely expensive and do not consider the uncertainties of the input sensory information. Therefore, they are only affordable by a few, and despite their high cost, they suffer from sensitivity to input uncertainty which could impact their performance. Hence, the motivation of this research is to design a cost-effective Active Prosthetic Knee (APK) with modular control/sensing

architecture. The drive mechanism of the APK should be simple to enable easy maintenance and high robustness.

1.1 Thesis Statement

1.1.1 Motivation

The need for advanced prosthetic technologies is in critical demand, as war amputee numbers continue to climb [1]. The millions of unexploded ordinance (UXO) devices pervade parts of Africa, the Middle East, and Southeast Asia. Each year, hundreds and thousands of civilians fall victim to these atrocities. Looking just at the effect of war gives us a perception of the demand for prosthetics in war torn nations:

> "Afghanistan, Angola and Cambodia have suffered 85 percent of the world's land-mine casualties. Overall, African children live on the most mine-plagued continent, with an estimated 37 million mines embedded in the soil of at least 19 countries. Angola alone has an estimated 10 million land-mines and an amputee population of 70,000, of whom 8,000 are children [2]."

In addition to land mine explosions, other factors such as diabetes, gangrene, infections, ischemic disease, farming accidents and even motor vehicle accidents can result in lower limb amputation.

Amputees not only lose their limbs but they also experience job loss, limited freedom of mobility, and increasing difficulties in day to day life. Advanced lower limb prostheses that are currently available are accessible to those in developed countries. The developing world on the other hand, continues to use devices that were developed nearly a half century ago. Hence, there is a tremendous need to develop and promote new, advanced lower limb prostheses for the developing word.

The Active Prosthetic Knee (APK) is a trans-femoral prosthetic knee device, suitable for those with one amputation and one healthy leg. Rather than utilizing the limited energy of the user, the APK provides active power at the knee joint to allow improved efficiency and minimal energy depletion when moving. Most of the current intelligent lower limb prostheses rely on sensors embedded in themselves. However, the proposed APK gains information from the intact contra-lateral leg. The innovation of the APK's mechanical design and unique controller provides a possible future in intelligent feedback design.

1.1.2 Research Justification

Mobility is oftentimes a task that does not require much thought for the able-bodied. However, for patients of amputation, it is a task that is painstakingly difficult. Daily livelihood is a difficult one, as war affected citizens struggle not only with their own physical limitations, but due to limited infrastructure to support them. The amount of time, energy and investments in rehabilitation can be significant, due to the aging technologies available in developing nations. Also, poor terrain and lack of funding resources are also a hurdle [1]. Once amputees are fitted with prosthetics, life with it is much improved than not having an assistive device. However, the overall fitting process is rather crude and can be further improved.

"Because a child's bones grow faster than the surrounding tissue, a wound may require repeated amputation and a new artificial limb as often as every six months [2]." Unfortunately, the excessive cost associated with so many prostheses leads to deprivation in developing countries.

The central focus of this thesis is to design a cost-effective prosthetic knee joint that allows a full range of motion, while allowing comfort and durability to withstand harsh terrain and other physical demands. The "active" in Active Prosthetic Knee refers to the energy being transferred from a power source used to mimic the natural gait cycle. A novel method of human gait phase recognition for cadence control is introduced in this work by utilizing a knowledge-based intelligent system. This knowledge is based on existing experience and known facts about the walking cycle. The proposed knowledge-

based control system takes advantage of an Adaptive-Network-based Fuzzy Inference System (ANFIS) to control the knee torque as a function of echoing the angular state of the able leg.

The principle task of APK is to assist the user in walking as normal gait cycle as possible. The APK research in this thesis combines a mechanical system design and an intelligent fuzzy-logic control system implementation that allows for developing an active prosthetic device for human locomotion.

1.1.3 Delimitations

Related areas of research that will not be investigated in this work include:

• Internal knee replacements used to substitute damaged knee joints. This thesis will only focus on full prosthetics for subjects without a knee.

• Socket for the user that covers the remnant stump and must be connected to the prosthesis. This thesis will only focus on full prosthetics and not interface between the APK and the leg stump.

• Material analysis. Materials are certainly an important aspect of APK design since varying the materials alters important APK properties such as weight and strength. Summary of Finite Element Analysis (FEA) of the APK and expansion part performed by other members of our research group are presented in [3]. However, the effect of material characteristics on APK mechanism performance will not be considered.

• Stability analysis of the overall system comprising the prosthetic leg. Since the ankle joint has not been manufactured up to the moment of publishing this manuscript, the stability analysis of the leg has not been studied which highly depends on center of rotation of the knee and the contact point of the foot and ground. Therefore, this work will be considered in future research.

• Cordless power supply. At this stage the power supply is plugged in, and as a result the APK is tethered. Further research is required to replace the current power supply with battery to energize the APK's actuator.

1.1.4 Potential Impact of the Research

This thesis may direct to continued development to the ankle as well as to research in other compliant prosthetics. The technology used in this study may be used in developing a low cost active ankle joint in future. Additionally, the specific control framework advancements achieved through this work may be possible to use in other non-prosthetic rehabilitation applications like muscles stimulation for paralyzed people. The wireless communication methodology between sensing system and the controller, which is achieved through this research, can be also used in other biomechanics applications. More significant will be the possible social impact of the compliant prosthetic knee. An active prosthetic knee with good functionality for a fraction of the cost of a standard prosthesis is what developing countries and war-torn nations desperately need.

1.1.5 Thesis Outline

This thesis proposes a novel approach for APK design that utilizes information from the healthy leg to drive an electromechanical actuator to enable the subject to follow a normal gait cycle. The thesis outline can be summarized as follows:

Chapter 1 presents relevant excerpts from the literature, but begins with a brief overview of gait phases, and knee anatomy.

Chapter 2 details the mechanical design of the APK. Moreover, the design of shank, passive ankle, and foot is also discussed in this chapter.

Chapter 3 covers the design of the test-bed developed to mimic the entire gait motion with the purpose of evaluating the performance of the APK.

Chapter 4 presents the equations of motion for human locomotion and the fabricated prototype.

Chapter 5 investigates and compares different sensing methodology to provide inputs data for the implemented control system.

Chapter 6 presents the proposed method of communication between the sensing modules and the controller and actuator of the APK.

Chapter 7 discloses the proposed control framework. Different fuzzy inference systems are investigated to select a suitable knowledge-based system for the APK.

Chapter 8 provides a summary of the thesis conclusion and suggestions for future works.

1.2 Background

1.2.1 Anatomy Defined

Between the hip and ankle joints, four main bones exist: femur, patella, tibia, and fibula. The longest and strongest bone of the human skeleton, femur, extends from the pelvis to the knee. Tibia and fibula are two long bones in the human leg between the knee and ankle. Tibia is the interior and thicker whereas, the fibula is the exterior and thinner one. The upper end of tibia joins femur to form the knee joint (Figure 1-1) which is the most complex joint in the human body. The femur has two lower rounded ends (condyles). The one toward the center of the body called the medial condyle, and the one to the outside called the lateral condyle. Above the condyles on both sides are epicondyles which work as sites for muscle and ligament attachment. The cruciate ligaments attach to the space between the two condyles called intracondylar fossa. Cruciate ligaments are the most important ligaments in the knee joint and they serve to stabilize it and guide its motion. The patella (kneecap) protects the knee joint and increases the quadriceps lever arm thus allowing the quadriceps to apply force to the tibia more effectively during extension. This triangular-shaped bone is not connected to femur or tibia directly. The patella is connected to the femur by being contained within the patellar tendon that connects the quadriceps muscles to the tibia. Fibula has no contact with the knee and attaches to the tibia by ligaments below the tibial bearing surfaces of the knee.
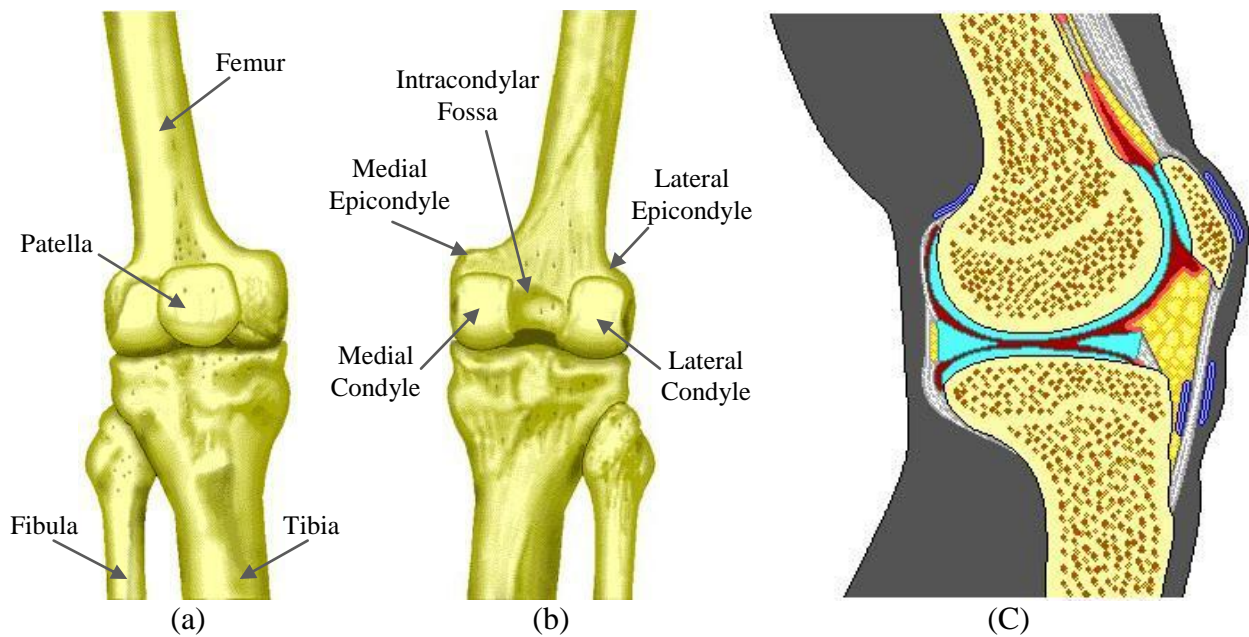
Figure 1-1: The skeletal view of the knee joint (a) anterior view (b) posterior view (c) cut view [4]

1.2.2 Movement

The three axes and planes of rotation of the biological knee joints are depicted in Figure 1-2. The anatomical planes allow for position/orientation representation of the knee in any of its three original planes. The line connecting medial and lateral femoral condyles defines flexion-extension motion, ϕ. The line along the tibia determines the axis of rotation for the internal-external angle, ψ. The perpendicular axis to the other two axes defines as the abduction-adduction angle, θ.
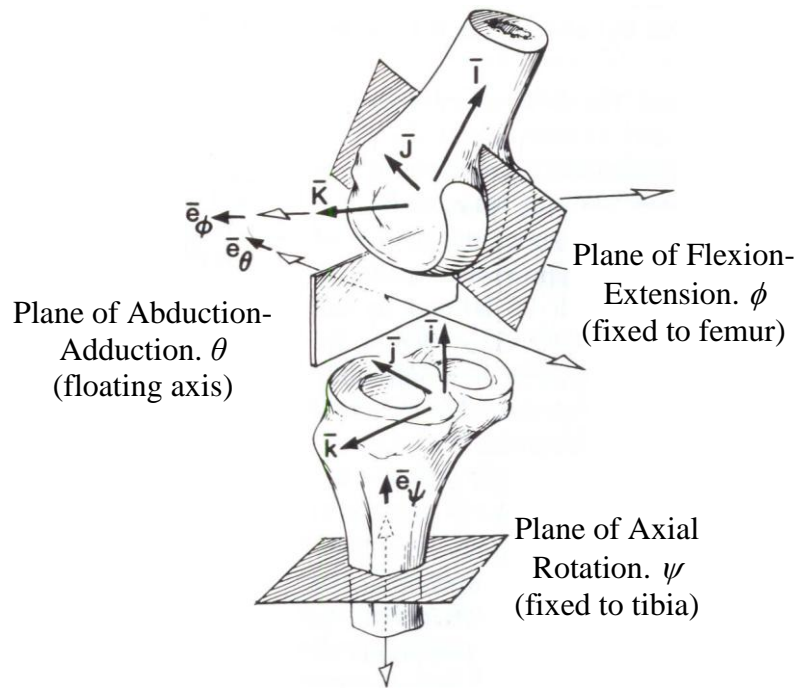
Figure 1-2: The axes and planes of rotation of the biological knee joint [6]

1.2.2.1 Sagittal (median) Plane

An upright plane passing from front to back; separate the body into right and left halves.

1.2.2.2 Coronal (frontal) Plane

A perpendicular plane running from side to side; splits the body into anterior and posterior parts.

1.2.2.3 Transverse (horizontal) Plane

A flat plane; divides the body into upper and lower portion.
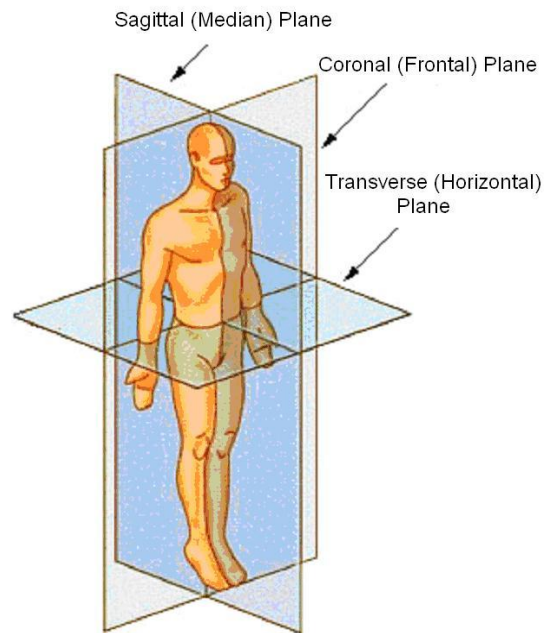
Figure 1-3: Anatomical planes [5]

1.2.3 Gait Cycle

Throughout a normal walking cycle, repetitive events occur. The repetitive pattern can be divided into two distinct events: 1) foot strike and 2) toe-off. When in a walking cycle, both legs contribute to four different events: 1) foot strike, 2) opposite toe-off, 3) opposite foot-strike, and 4) toe-off. Since the events occur in a similar sequence and are independent of time, the gait cycle can be described in terms of percentage, rather than time, thus allowing normalization of the data for multiple subjects. The initial foot strike occurs at 0%, and occurs again at 100% (0-100%). The opposite leg undergoes the same events, only out of phase by 180 degrees, with the opposite foot strike occurring at the 50% mark, and the second opposite foot strike occurring at 150% [6].

Each stride represents one gait cycle and is divided into two periods (main phases): *stance and swing* (Figure 1-4). Stance is the period when the foot is in contact with the support surface and constitutes 62% of the gate cycle. The remaining 38% of the gait cycle constitutes the swing period that is initiated as the toe leaves the ground. The stance phase is divided into four phases: *initial double support, mid-stance*, *terminal stance*, and *second double support.*

The initial double support (phase #1) extends from foot strike to opposite toe-off (0-12%). The initial limb support is characterized by a very rapid weight acceptance onto the forward limb with shock absorption and slowing of the body's forward momentum. Mid-stance (phase #2) and terminal stance (phase #3) are involved in the task of single limb support when the weight of the body is fully supported by the reference limb (from opposite toe-off to opposite foot strike). The mid-stance phase (10-30%) initiates with lifting of the opposite foot and continues until body weight is aligned over the supporting foot. The terminal stance (30-50%) commences when the heel rises and continues until the opposite foot strikes the ground. Body weight progresses beyond the reference foot during this phase. The second double support (phase #4), which is also called pre-swing, prepares the limb to swing; it begins after the opposite limb has reached the floor and begins to accept weight. Transfer of body weight from the reference limb to the opposite

limb takes place in this stage; the length of this phase is exactly the same as that for phase #1 (50-62%).

The swing period can be subdivided into three phases: *Initial swing, mid-swing, and terminal swing.* Initial swing (phase #5) starts with toe-off and ends with foot clearance when the swinging foot is opposite the stance foot (62-75%). Mid-swing (phase #6) continues from the end point of the initial swing and continues until the swinging limb is in front of the body and the tibia is vertical (75-85%). In the terminal swing (phase #7), the limb is decelerated and finally strikes the ground for the second time (85-100%). Limb advancement is performed during the pre-swing phase and throughout the entire swing period.
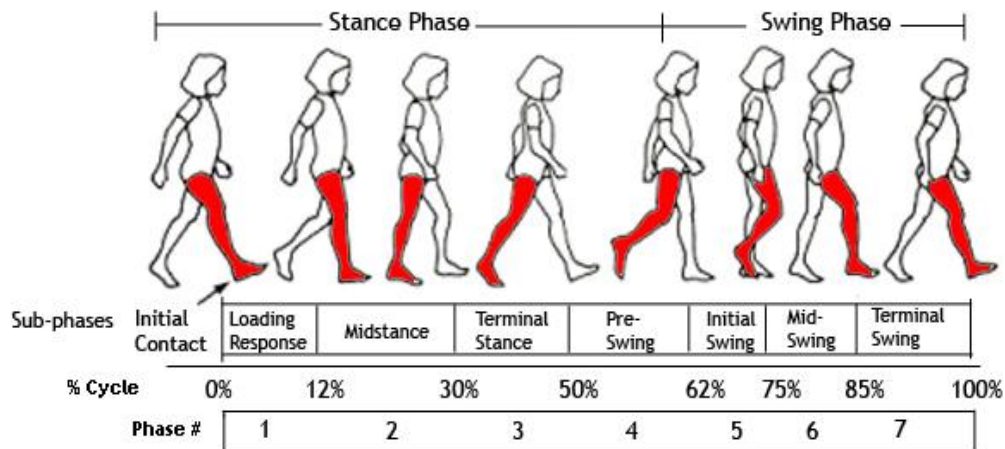
Figure 1-4: Gait phases [7]

1.3 Human Compatibility

The APK device is non-invasive, hence biomaterial concerns do not exist. However, the prosthetic must be able to withstand rigorous physical demands while also being light enough and durable for prolonged use. However, due to maintaining lower costs along with providing these necessary traits, the materials required a reasonable compromise.

1.3.1 Anthropometric Analysis

The APK must be adaptable to a broad demographic range. Hence a modular design and ability to conform to a broad range of human fitment plays is necessary to achieve such adaptability. The study of anthropometry is one that focuses on the human body, where individual human height is fractionally calculated to determine bone length [8]. The APK design was based upon anthropometric data obtained from the University of Waterloo's Department of Kinesiology, focusing solely on North American demographics. Since detailed anthropometric data is not readily available for demographics based on developing regions, a typical North American stature was used at this stage in the research. The issue of how many sizes should be offered and exactly what they will be is beyond the scope of the present thesis.

The data obtained from the University of Waterloo's Department of Kinesiology is that of a healthy male subject, 172 cm in height and with a body mass of 56.7 kg. Based on the corresponding anthropometric scales [8] and the actual measurements of the test subject, the leg segment length is found to be 42.5 cm. The leg segment is defined as the length from the lateral epicondyle of the thigh (the knee joint) down to the lateral malleolus (ankle joint), as shown in Figure 1-5(a).

In Figure 1-5(b), the variable H is the overall height of the subject. It is found that the tibial portion is calculated as $0.246H$, which corresponds to 42.3 cm. From those measurements, the total length of the APK (without the tibial extension) is estimated to be 27.5 cm. Hopefully, this size would provide a good fit for a fairly wide range of patients.

Furthermore, the weight can be calculated using anthropometric data. Since the device must have a good fit with the body and be compatible with a broad demographic length range, the weight component of existing data also applies. As such, the segment weight of the leg portion (as defined above) is $0.0465\ M$, where M is the total weight of the entire body. In this case, a person weighting 56.7 kg has a corresponding leg mass of 2.63 kg. In this research, the proposed APK weighs 1.63 kg. This provides leeway for approximately

one kilogram of additional weight to accommodate the tibial extension and additional foot peripherals.
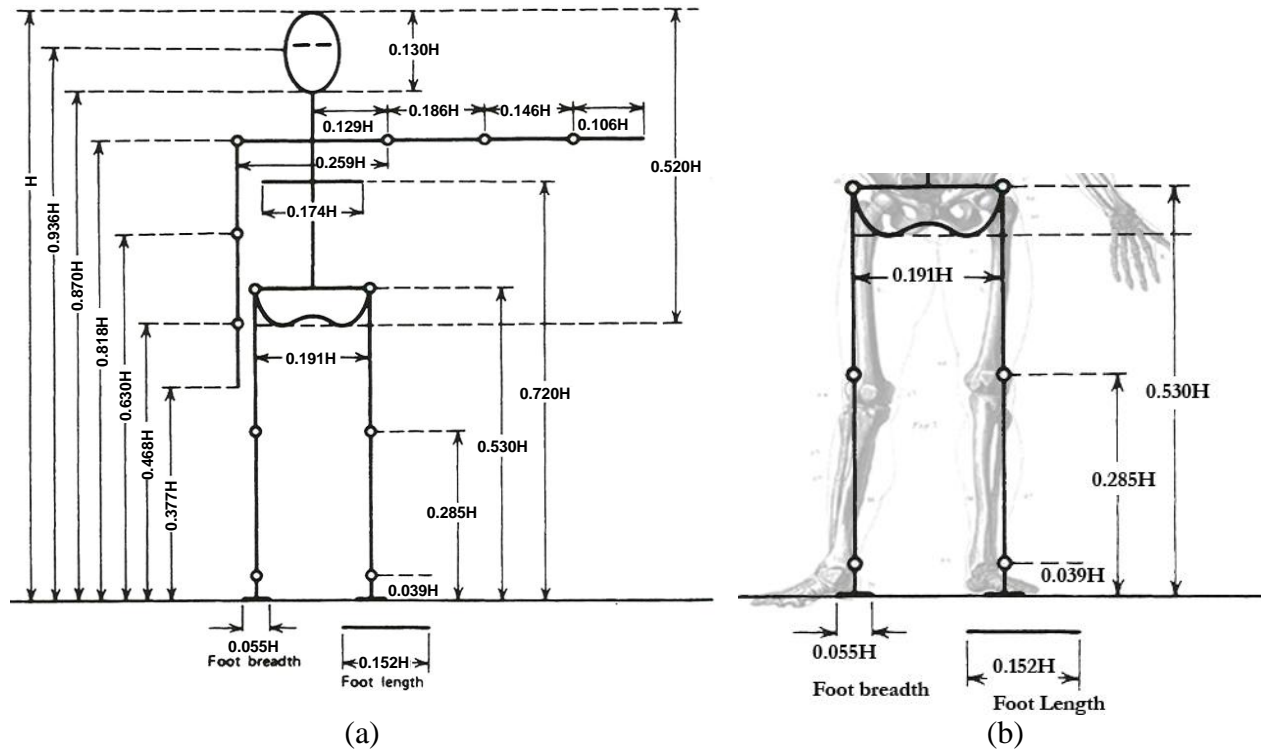
Figure 1-5: Anthropometric data for (a) a skeletal system (b) the lower body [6].

1.4 Different Types of Prosthetic Knees

1.4.1 Passive Knees

The knee joint is the most crucial part of lower limb. Muscle action provides power for a biological knee in two ways; the active force is applied by muscles contraction, also variable stiffness is provided by muscles. Only the latter action is used in "passive" prosthetic knee.

"Passive" prosthetic knees can be categorized into two groups: "simple-passive" and "semi-passive". There is no automated control over prosthesis stiffness in "simple-passive" knees. However, the level of stiffness can be adjusted manually. During the weight bearing, the leg can be kept from buckling and stumbling by means of i) manual lock, ii) weight activated stance mechanisms, iii) fluid resistance, or iv) polycentric

mechanisms. One manual locking knee is presented in Figure 1-6(a). A remote release cable is utilized in this device to provide stability in knee extension. This device leads to high energy cost during ambulation. In weight-activated knee, a constant-friction is used to provide high stability during the stance phase. Transferring the body weight to the knee activates an embedded brake that prevents buckling. This brake will release when the knee becomes unloaded. However, a constant friction still presents during the swing phase which results in inefficient gait. An energy storing element such as spring can also accompany the knee during the swing phase. It is loaded in weight bearing and is released during swing phase. An example of this type of prosthesis is depicted in Figure 1-6(b). Fluid resistive knees consist of hydraulic or pneumatic cylinders to provide variable resistance. Therefore, amputee would be able to have different walking speed. Piston of the cylinder is attached to a hinge joint in the thigh section behind the knee joint. From the other end, cylinder is connected to a pivot in shank. Hydraulic knees are more efficient than pneumatic ones. However, the pneumatic knees are lighter, cheaper, and cleaner than hydraulic ones. Polycentric knees have multiple axes of rotation. These prosthetic devices are kinetically locked during mid-stance and provide stability. An example of polycentric knees is depicted in Figure 1-6(c). To provide variable walking speed for amputees, pneumatic or hydraulic cylinder can be embedded in polycentric knees. The aforementioned "simple-passive" knees are low-cost compare to the other types of prosthetic knees. Therefore, most consumers of these devices are children since they need to change their prostheses as they grow up.

(a)   (b)   (c)
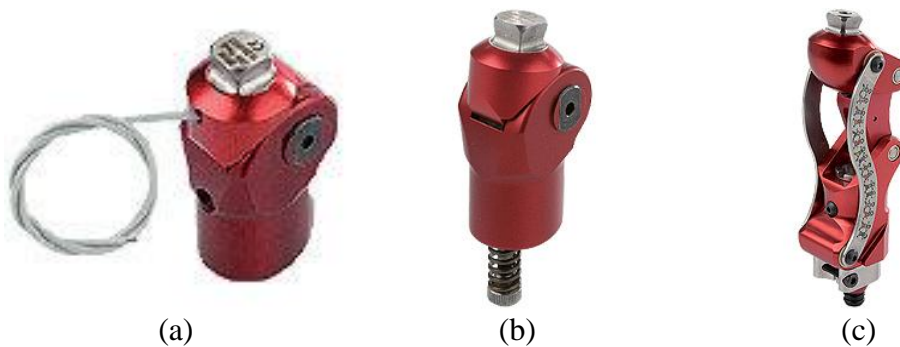
Figure 1-6: (a) manual locking knee (3R39, Otto Bock Healthcare GmbH) (b) weight-activated knee (3R38, Otto Bock Healthcare GmbH) (c) Polycentric knee (3R66, Otto Bock Healthcare GmbH) [9]

In a microcontroller based passive knee joint, the controller changes the knee impedance (damping and/or stiffness) based on sensory information. This resistive torque for the knee joint can be provided by electric brakes, or by hydraulic, pneumatic, Magneto-Rheological (MR) dampers. These types of knee joints are called "semi-passive" prostheses since their stiffness can be altered by the controller.

Aeyels et al [34] developed the first micro-controller based knee joint which comprised of an electromagnetic brake. A gear box accompanies the brake to increase the applied resistive torque to 50 Nm. The resistive moment is varied continuously based on the sensory information from the remnant stump and prosthesis state.

The hydraulic damper with variable impedance comprises a double acting cylinder where two sides of the piston are connected through a valve. The commands determine the position of a valve that controls the flow of oil from one chamber to the other [11]. The drawback of hydraulic based knees is the presence of a minimum level of damping during all phases of the gait cycle, even when it is not needed. Carlson et al [12] and Kim et al [13] replaced the hydraulic damper with an MR damper to achieve a faster response for different speeds of the gait cycle. The problems with MR dampers are their susceptibility to: degradation of the MR fluids, sealant failure, leakage, and performance problems as well as high cost for commercial applications.

1.4.2 Active Knees

Although lower limb prostheses have traditionally been passive, there have been attempts at providing active versions.

Most of the developed hydraulic and pneumatic powered knees are tethered to an external power supply because associated prostheses suffer from high energy consumption. Flowers and Mann [12] and Stein and Flowers [15] suggested a powered electro-hydraulic knee joint tethered to a power source. They used a hydraulic cylinder controlled by a 4/3 servo valve to actuate the knee. Recently, Sup [16] developed a pneumatically

actuated powered-tethered lower limb which is controlled by a computer to alter the impedance of the actuators.

One of the commercialized pneumatic knee joints is Intelligent Prosthesis, IP, (Chas A. Blatchford and Sons, Ltd.). A pneumatic cylinder is employed to provide the rotary motion of the knee joint during the swing phase. One stepper motor is used to adjust the position of a needle valve (orifice) which controls the flow rate between two sides of the piston. The stepper motor is controlled by a microcontroller based on the sensory information according to the swing speed of the prosthetic leg. Buckley et al [16] revealed rationale for the commercialized IP when they compared the energy cost of the IP and conventional artificial knee joint. Although IP is not tethered like the other aforementioned hydraulically/pneumatically actuated knee joints, its utilized system mobilized the knee joint only during the swing phase.

Wang et al [18] proposed a hydraulic system, which compresses the fluid in an accumulator during stance, and then energizes and controls the knee during swing by using a needle valve. The hydraulic circuit consisted of an accumulator, two cylinders (one for the ankle joint and one for the knee joint), and two flow control valves. Also, the motion of the ankle joint causes the motion of a piston in an ankle cylinder. This piston is connected to a control rod that switches the shut valve to control fluid flow from the knee cylinder to the accumulator. A stepper motor actuates a needle valve which controls the flow rate between accumulator and knee cylinder. The problems of low efficiency and large size are the main flaws of the aforementioned system.

It is worth noting that Saito [18] developed a tethered lower limb active orthosis equipped with a bilateral-servo actuator to mimic the function of a bi-articular muscle. Orthosis is an added support mechanism, usually a brace, to help a disabled person function. Saito accomplished such task by using master and slave hydraulic cylinders. A ball screw mechanism accompanied with a stepper motor controlled the master hydraulic cylinder. The slave side system comprised of a cylinder and two piston rods acts as a bi-articular muscle. Both master and slave cylinders can be controlled by open-shut solenoid valves.

Sawicki et al [20] proposed a wearable bilateral lower limb orthosis. They used pneumatic artificial muscles attached to the orthoses to provide flexion and extension torque at individual joints. Although these pneumatic artificial muscles are light-weight and suitable for lower limb exoskeleton and orthosis, they cannot generate enough power for fully active lower limb prosthesis.

Recently, Kapti and Yucenur [21] proposed a tethered fully active knee powered by an electro motor and a gear reduction system. They tried to decrease the user's energy cost by providing a fully powered trans-femoral joint. Popovic et al [22] presented a methodology to determine the optimal motor size for a motorized prosthetic knee.

Chapter 2

MECHANICAL DESIGN

2.1 Design Features

Although the author has contributed to the APK mechanical design, most of the works done in section 2.1 are provided by the other member of the research group: J. Lim [3]. However, the author has mainly undertaken the rest of the thesis[1].

The Active Prosthetic Leg (APK) was developed through three design phases [3]. Through several iterations, the final design was identified and prototyped. The primary objective of the APK was to design a transfemoral device that is light and small enough to be utilized by a broad demographic range. Utilizing anthropometry and human system analysis, the APK was designed within the bounds of a broad demographic range. Moreover, to be adequately light and agile, the APK was design using aluminum 6061. Although it was found that more expensive and rare alloys provided less weight and

---

[1] It is worth noting that the author has contributed in this endeavour since the APK project was launched.

greater structural integrity, due to budgetary constraints and other variables, aluminum was selected. With the exception of purchased, pre-manufactured components, all structural parts were made of aluminum. Furthermore, the design does not include the femoral "stump" socket and the tibial extension.

The tibial component is the primary constituent of the APK, where the greatest loads and applied pressures are exerted onto. The APK is designed with this in mind, but also with irregular cyclical high impacts acting on it. Moreover, the APK must be rigid in order to resist difficult and rough terrains that the subject may walk through

All the joints on the APK are simple 1-DOF components of high-precision bearings in dual parallel setup, providing additional torsional stability. The ball-screw that allows the device to move the knee joint is a high-speed, austenitic-chromium-nickel-manganese 202 stainless steel device. The APK design is based on 70 kilograms subject.

Figure 2-1 reveals the proposed APK. Component (1) is distal to the knee joint, the primary part that provides the load bearing for the entire system above it. The tibial component (2) provides the most of the load bearing from the human subject's weight acting on the leg. The tibial component is found to be semi-circular, allowing compression resistance in the coronal plane. Additionally, the design allows improved stress resistance in the transverse plane. The tibial component is connected to the torque arm (3), the component that provides the necessary active torque to the knee joint system. The ball-screw (4) is the principal mechanism of the entire device, not only providing motion, but also withstanding a great proportion of the weight. The ball-screw is contained within the motor carrier (5), onto which the servomotor is also mounted.
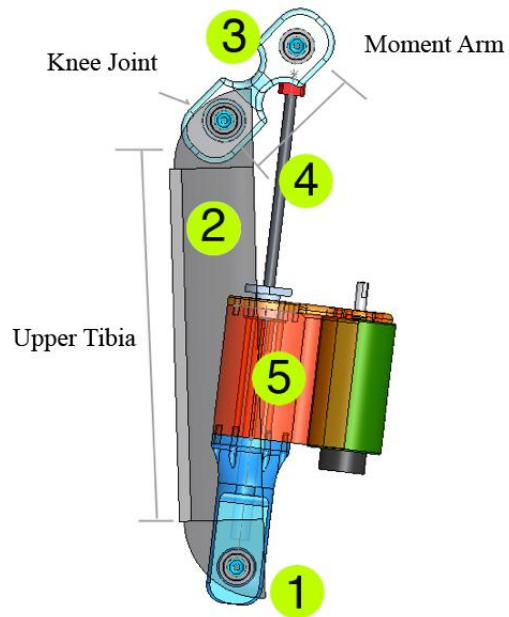
Figure 2-1: Profile view of the APK

Figure 2-2: Three dimensional rendering of the APK on a person

Figure 2-2 shows that the desired implantation of the APK on subject's body . The designed APK is small enough to fit a wide demographic range. The three dimensional figure highlights the overall dimensions of the design, with its lightness and compact size, promotes and allows manoeuvrability and agility.

Figure 2-3 shows an exploded view of the APK system. The view shows the 12 bearings, 18 unique screws and 13 individual parts that make up the entire APK system.
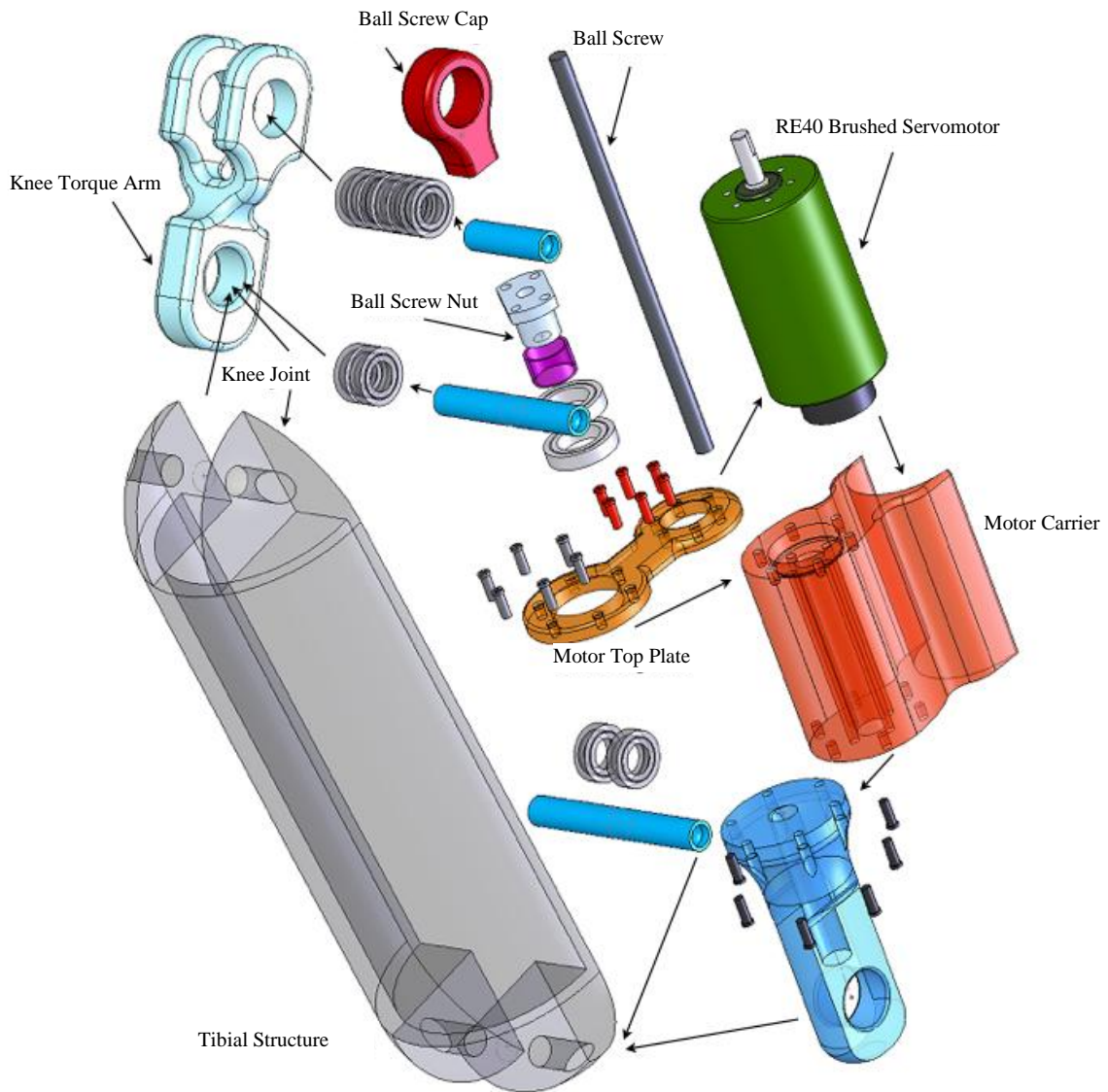
Figure 2-3: Three dimensional exploded view of the APK

Top View

Front View

Rotary
motion

Translational
motion

Ball-screw

Electro-motor

Side View
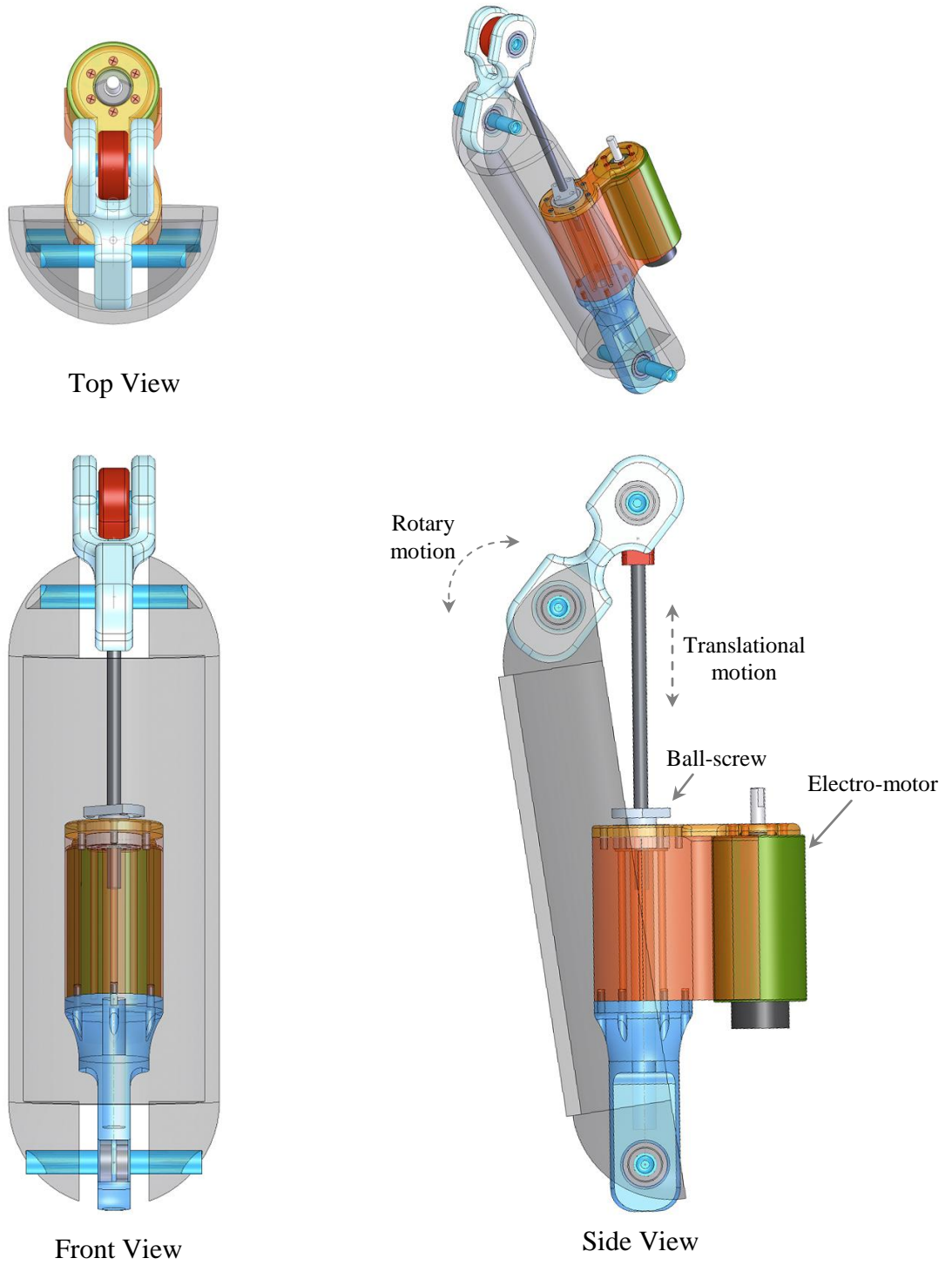
Figure 2-4: Final assembly of the APK
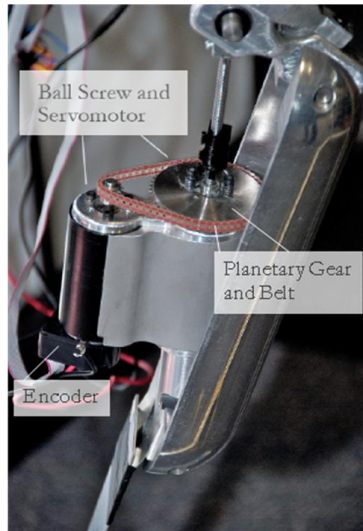
Figure 2-5: APK

Figure 2-6: APK knee joint

2.2 Mechanical System

The APK shown in Figure 2-5 has a high-speed motor, that also produces sufficient torque to derive the prosthesis. The operating peak speed required for the system is 7,468 rpm, where it produces the optimal speed and torque output. Utilizing a gear reduction connected through a ball-screw mechanism, allows for the final gear output to move at a slower rotational velocity, with higher outputs of torque. The servomotor is attached in parallel to the ball-screw, and mobilizes its nut by utilizing the belt-drive. The nut is embedded in two bearings. Therefore, both the electro-motor and the nut are fixed in their place and do not have any relative motion with respect to each other. They just rotate in their place. The rotation of the ball-screw, connected adjacent to the belt-drive system allows for the translational motion that produces the motions of the knee joint.

Figure 2-1 shows a CAD drawing of the APK. In this figure, t_1 and t_2 are the number of teeth of gears for pulley system – that can be adjusted and made specific to the user's needs. Furthermore, r represents the length of the arm that is fixed between the knee joint and the upper end of the ball-screw. The angle between the axis of aforementioned arm and the central ball-screw axis is called α. The angular velocity and angular acceleration

can be calculated using the first and second order time differentiation. Firstly, the angular velocity, ω, is represented in rpm, where ω_k denotes the knee rotational velocity and ω_m representing the motor angular velocity. The lead of the screw, l, is the multiplication of the pitch and the number of starts. In the case of the APK, the lead is 0.001 meters. The correlation between the linear velocity of the axis of the ball screw, V, and knee angular velocity is:

$$\omega_k = \frac{V}{r \sin \alpha} \tag{2.1}$$

This linear velocity is the consequence of the rotation of the ball-screw's nut. In other words,

$$V = \frac{l}{2\pi} \omega_{B.-S.} \tag{2.2}$$

while the angular velocity of the ball screw, $\omega_{B.-S.}$, depends on the gear reduction and velocity of the driver motor:

$$\omega_m = \frac{t_2}{t_1} \omega_{B.-S.} \tag{2.3}$$
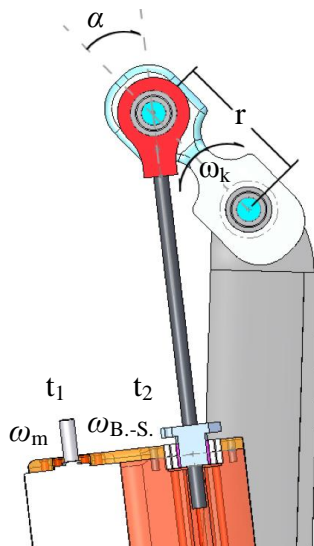
Figure 2-7: The mechanics of the APK

Replacing (2.2) in (2.1) and substituting the outcome in (2.3), the motor velocity can be found based on the knee velocity:

$$\omega_m = \omega_k \left[\left(\frac{l}{2\pi} \right) \left(\frac{1}{r.\sin(\alpha)} \right) \left(\frac{t_1}{t_2} \right) \right]^{-1} \tag{2.4}$$

The rotary speed of the APK is assumed as 0.5 rev/sec (30 rpm). For this desired angular velocity, from (2.4) the maximum motor speed with respect to α is calculated as 5,775.8 rpm.

The correlation between the generated knee torque, τ_k, and the applied force from the ball-screw, F, is

$$\tau_k = F.r \sin \alpha \tag{2.5}$$

The torque required in the nut of the ball-screw to provide the force to push and pull the arm can be calculated as [23]:

$$\tau_{B.-S.} = \frac{F.l}{2\pi \eta} \tag{2.6}$$

where $\tau_{B.-S.}$ is the applied torque from the ball-screw (nut) and η is the efficiency. In (2.6) it is assumed that the frication is negligible. The correlation between produced torque in ball-screw and applied torque from the electro-motor, τ_m, is

$$\tau_{B.-S.} = \frac{t_2}{t_1} \tau_m \tag{2.7}$$

Substituting (2.6) and (2.7) in (2.5), the correlation between the knee torque and applied torque from the electro-motor can be obtained as

$$\tau_k = \tau_m \left[\left(\frac{2\pi}{l} \right) \left(\frac{t_1}{t_2} \right) r \eta_t \sin \alpha \right] \tag{2.8}$$

24

The overall efficiency, η_t, which is the product of all the moving parts, is found to be 46.4%. Using (2.8), in the APK operating range, the maximum torque output is 23.44 Nm. This value is applied at the point of mid-stance into toe-off. The maximum knee torque is a critical parameter in selecting the proper electro-motor.

Further details of Figure 2-7 such as free body diagram are given in the subsequence dynamics chapter.

2.3 Degrees of Freedom

The APK's overall movements are calculated using Gruebler's Mobility Equation with Kutzbach's modification for planar mechanisms [24]. The overall number of degree of freedom of the system can be calculated using the following equation:

$$M = 3(n-1) - 2f_1 - f_2 \tag{2.9}$$

where M represents the degrees of freedom for the overall system, n, the total number of fixed link segments, f_1, the joints with one degree of freedom (DOF) and f_2, the joints with two degrees of freedom. The overall system is found to have 5-DOF, where the main knee joint has 1-DOF. The human knee in comparison has 6-DOF, a much more complex system. However, to maintain mechanical durability and remain within the bounds of a low-cost device, the APK knee joint is simplified to a hinge-type 1-DOF mechanism. The APK contains three anatomically equivalent parts – the upper tibia, knee joint and the moment arm that represents the active knee joint.

2.4 Servomotor Integration

The APK utilizes servomotor, which provides the necessary power to produce the required torque of the knee. The motor, Maxon RE40, is a graphite brushed, capable of operating constantly at 8,200 rpm while outputting 0.201 Nm. The RE40 motor measures 40 mm (outer diameter) and the total length is 91.3 mm.

Figure 2-8(a) represents the RE40's operating ranges. The dark components illustrate the peak operating range for the motor. Figure 2-8(b) is representative of key specifications for the RE40.
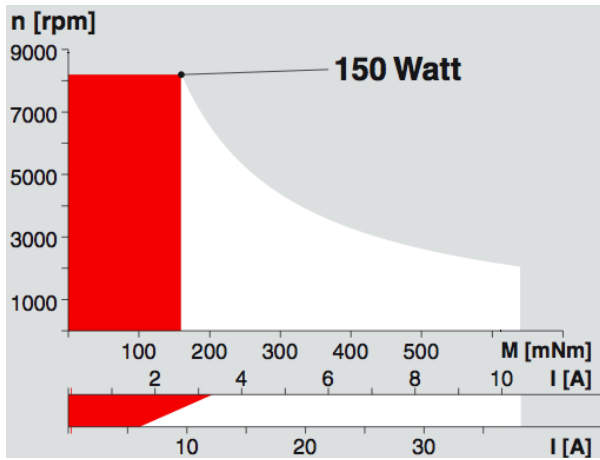
Power Rating	150 W
Nominal Voltage	48 V
No Load Speed	7580 rpm
Stall Torque	2.5 Nm
Torque Constant	60.3 nMm/A
Speed Constant	158 rpm/V
Max. Permissible Speed	8,200 rpm
Max Continuous Torque	0.201 Nm

(a)   (b)

Figure 2-8: Maxon RE40 Program Operating Range and Specification Table (Maxon, 2005)

2.5 Expanding APK by Designing a Below Knee Section

This section focuses on the extension of the APK and the design of a shank and 1-DOF passive ankle for the prosthesis. Adding a shank and foot to the prosthesis will make us capable to test the APK. This section is at prototyping stage and the fabrication has been finished at the moment of writing this manuscript (Aug. 2008).

The shank and ankle design must meet the following requirements: i) Offering at least one degree of freedom for the ankle at sagittal plane, ii) Providing the range of rotary motion same as biological foot for dorsiflexion and plantar flexion in sagittal plane, iii) Capable of absorbing the impact of the ground reaction force, iv) Withstanding 1.2 times of the user weight (equals to the maximum Ground Reaction Force (GRF) [8]), and v) Having the foot length of 15.2% of the height of the user (please refer to anthropometric data in section 1.3.1). In addition, the cost, weight, and simplicity of the designed below knee prosthesis are the important criteria in designing.

One off-the shelf Solid Ankle Cushioned Heel (SACH) prosthetic foot was purchased to complete this part of the APK. This basic prosthetic foot consists of neoprene moulded over a wood keel. It has a good energy absorption capability for impact loading. As shown in Figure 2-9(c) one torsion spring is embedded in the ankle pivot to provide the required stiffness for the leg. Also the spring brings back the foot into the normal condition when no GRF applies to the foot. In addition, one stopper is designed to restrict the rotation of the foot around the pivot joint.

The shank consists of two parts (upper and lower parts) and has an adjustable length. The upper shank (or pylon) is Y shape, and the lower part is an inverted T shape ($\perp$). The upper part will connect to the APK from one head and to the lower part from the other head. Five holes on the upper and lower parts are extruded to achieve this purpose. To adjoin the upper and lower parts, two bolts and nuts are required to prevent the leg from rotatting sideways. This enables four levels of length adjustments using such a configuration.

The designed ankle is bolted from its bottom side to the plastic foot. The ankle portion and lower part of the shank form the ankle joint. The shank lower head is situated in the middle of the ankle portion, and one pin is used to form the pivot and hold the ankle and the shank together. The torsion spring will be located between the ankle and the lower shank in the posterior of the foot. As a result, two slots are designed on the lower shank and ankle to hold the spring legs. The spring is always compressed, and it applies continuous torque to the foot. The spring legs are placed in the thin slot as shown in Figure 2-9. A final assembly of the shank/ankle/foot (the knee extension) is illustrated in Figure 2-10.

(a)

(b)

Torsion Spring

(c)

(d)
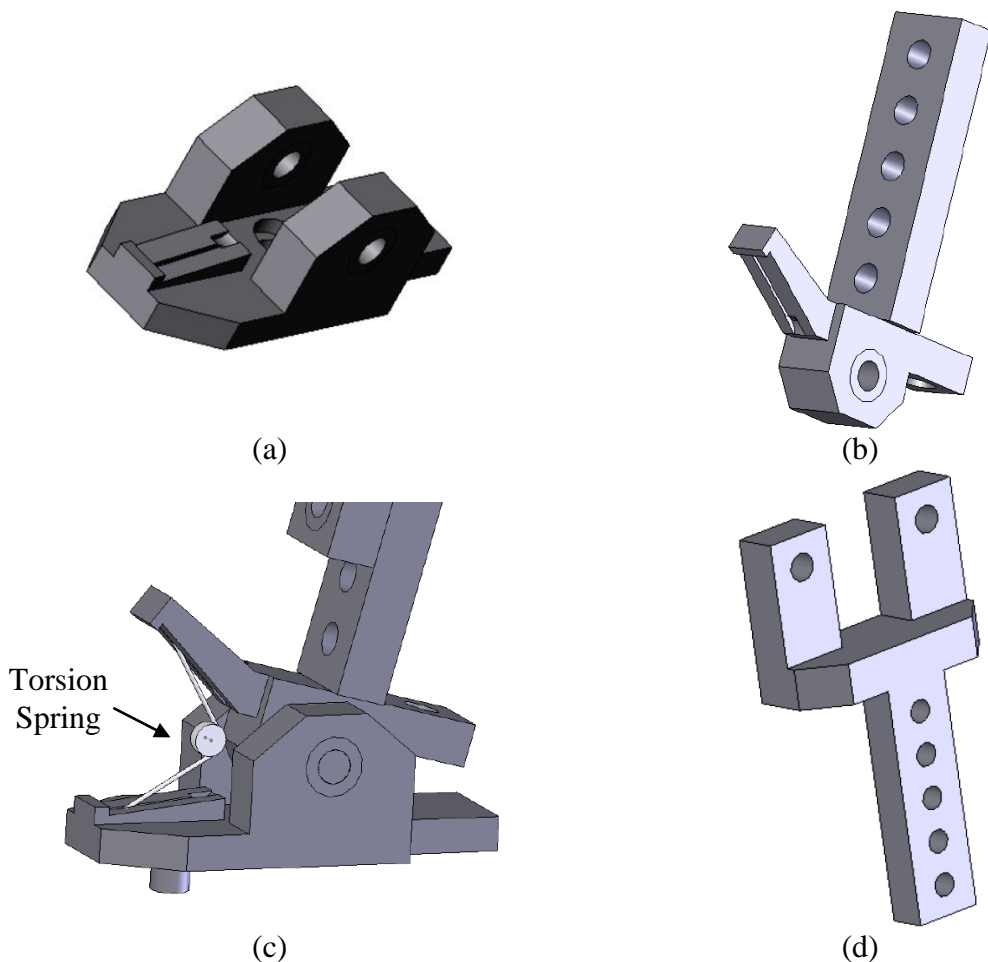
Figure 2-9: The extension parts of the APK: (a) and (b) ankle and its connector to thee foot weighs 397 and 307.6 grams, respectively, (c) assembled ankle and torsional spring, and (d) shank weighs 598.6 grams.

Top view   3D view

Front view   Side view
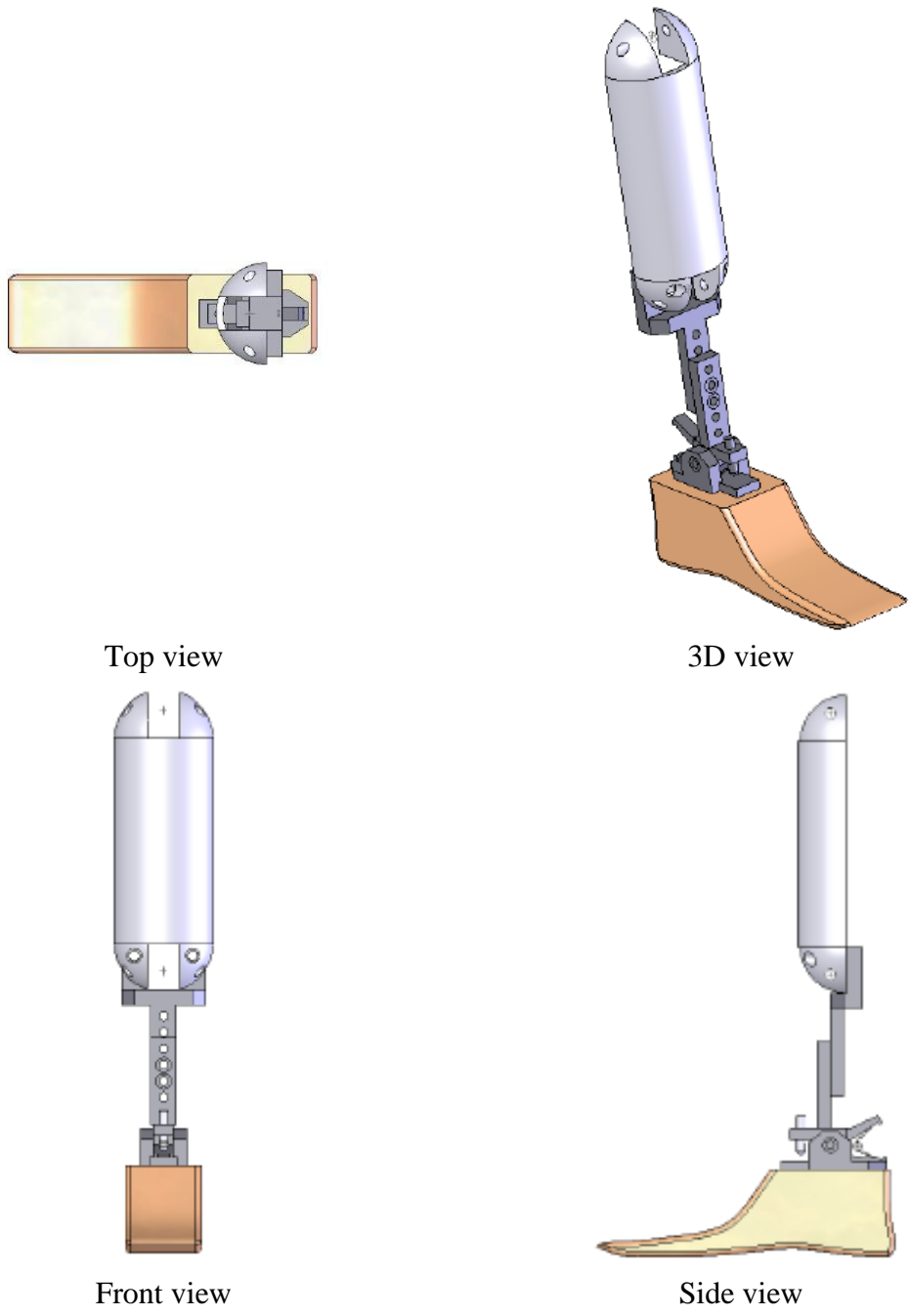
Figure 2-10: Standard views of the APK extension

2.5.1 Calculating the Spring Stiffness

The horizontal position of the centre of gravity of the foot was obtained by balancing the foot on top of a thin ruler. The foot was shifted back and forth until it became evenly balanced on top of the foot.
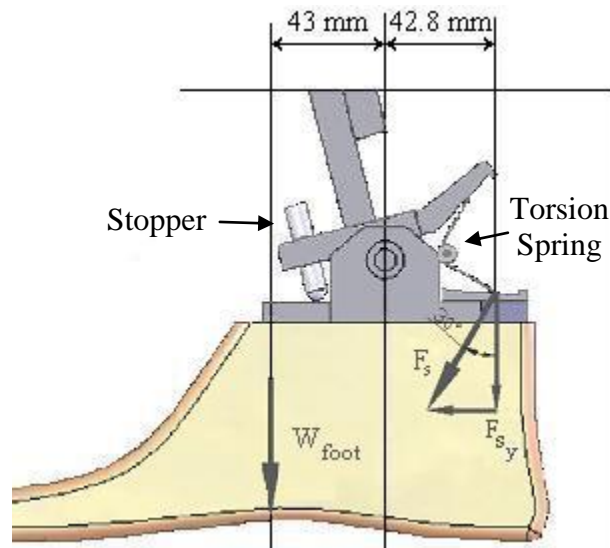
Figure 2-11: The spring force versus the weight of the foot

As depicted in Figure 2-11, the center of gravity is located 43mm far from the ankle joint. Moreover, the distance between the ankle center of rotation and the end of the spring leg is 42.8 mm. Morever, we can define:

$$F_{S_y} = \frac{W_{foot} \times 43\text{mm} \times FOS}{42.8\text{mm}}$$
(2.10)

where W_{foot} is the foot weight equal to $(0.608 \times 9.81)= 5.9645$ N; FOS is Factor of Safety equal to 1.25; F_{S_y} is the Y-component of the spring force. From the above equation F_{S_y} is calculated as 7.49 N. Therefore, the spring force is

$$F_S = \frac{F_{S_y}}{\cos 30} = \frac{7.49\,\text{N}}{\cos 30} = 8.65\,\text{N}$$
(2.11)

In Figure 2-11, the spring is bent 90 degrees, and the force is applied 25mm away from the spring axis, thus r =25mm. The stiffness of torsional spring can be calculated from

$$\tau = k.\Delta\theta \qquad\qquad (2.12)$$

$$k = \tau / \Delta\theta = F.r / \Delta\theta = (8.65\,\text{N} \times 25\text{mm})/90° = 2.4\,\text{Nmm}/°$$

Based on the above calculations, a spring model that fits the required specifications is selected. The parameters of the spring are shown in Table 2-1.

Table 2-1: The specifications of the selected torsion spring

Manufacturer	Vanel Springs
External Diameter	7.5mm
Wire Diameter	1.0 mm
Number of coils	2
Leg Length	30.0 mm
Spring Rate	3.8733 Nmm/ °

Chapter 3
TEST–BED

3.1 Introduction

A test bed was designed and fabricated to evaluate the performance of the prosthetic knee before actual testing on human. The test bed allows lower-limb motion experimentation to mimic the entire gait motion by mobilizing the femur and the hip joint and to provide ground reaction force for the leg. This section incorporates the design and development of the modular test stand.

The test stand required five major components: i) a structural frame to hold the entire system, ii) a hip unit to hold the hip joint and provide restricted motion for it, iii) a simple rod to act as the femur, iv) a pneumatic system to mobilize the femur, and v) a treadmill to simulate ground reaction force. Each of these components is discussed in the following sections. Before the aforementioned components, especially the hip unit, are discussed, it is necessary to describe the displacement of the human hip and pelvis in the normal walking.

3.1.1 Hip Joint/Pelvis Displacements

Since it has not been possible to test the fabricated prosthesis on a volunteer amputee so far, we have tried to mimic human locomotion such as sagittal motion of the center of gravity on the test setup as much as possible. During normal human gait cycling, the center of gravity follows sinusoidal curves on both the sagittal and transverse planes. The sinusoidal path on the plane of progression is lowest in double support and highest in mid-stance phase. Therefore, the period of the vertical oscillation of the center of gravity is half of a stride time (two times the frequency of the stride). The center of mass also moves horizontally as mid-stance alternates between the right and the left leg. However, the frequency of this movement is half of the frequency of the vertical displacement. The actual displacement is approximately 5cm vertically and 5cm horizontally [10]. Figure 3-1(a) below shows the displacement of the center of gravity for a human body during normal level walking on a level surface.

(a)   (b)
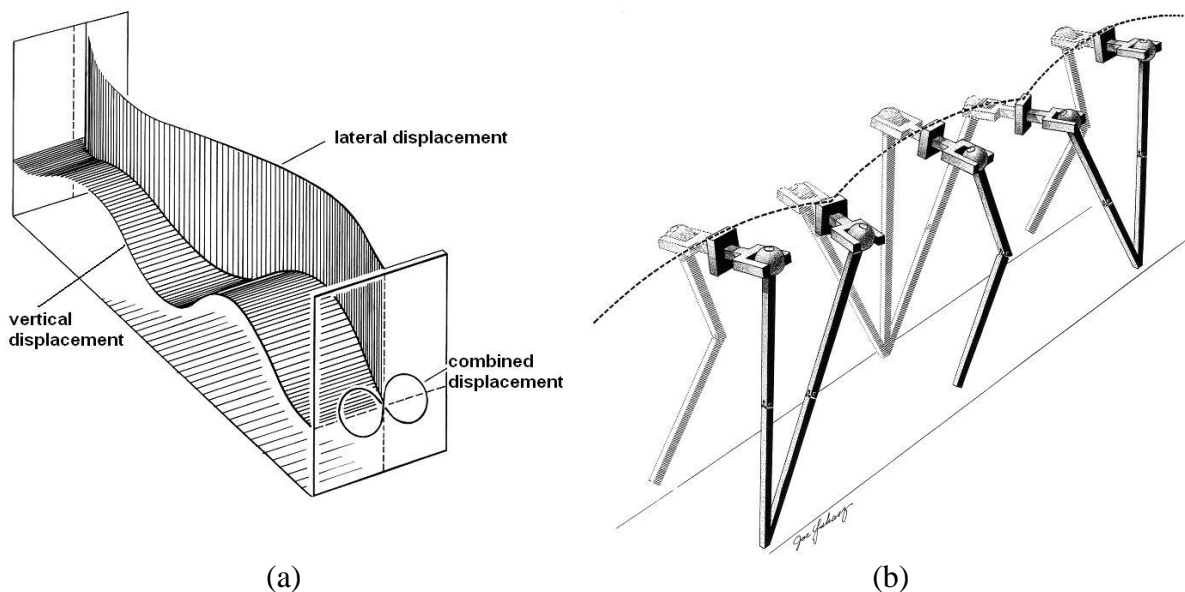
Figure 3-1: The exaggerated displacement of center of mass during one stride (a) lateral and vertical displacements in transverse and sagittal planes. Combination of these to displacements onto a plane perpendicular to the plane of progression is shown too [6]. (b) a simplified model showing bipedal locomotion; the vertical motion of the pelvis is indicated by dash lines [6].

The hip joint and pelvic displacements are correlated to the displacement of the center of gravity. Figure 3-1(b) illustrates the pelvic and hip joint motion. Therefore, two springs are added to the fabricated test rig to mimic the vertical motion of hip joint. Further details will be discussed in the hip unit design section.

3.2 Stand

The test stand is a rigid, aluminum structure made from a Bosch Rexroth modular profile system. An $\frac{1}{8}$ inch Plexiglas layer is placed on the top face of the frame, allowing a space to place the electronic testing equipment. The hip unit and pneumatic systems are embedded into the frame with bolts.

3.3 Hip Unit

The hip unit design consists of four main parts: i) the main body ii) upper plate iii) side palates iv) two springs. Figure 3-2 presents a 3D view of the hip unit.

The main body comprises the hip joint which acts as a pivot joint for the femur. The hip unit adjoins the test-rig frame through the upper plate. This plate is bolted to the frame. Two springs are located between the upper plate and main body to provide the sinusoidal motion for the hip joint. The upper plate holds the main body with the assistance of two side plates welded to it. Each of these plates has a slot that guides the traveling pin attached to the main body.

Two screws that attach the upper plate to the frame must be long enough to provide guidance for the two springs. Clearance holes are drilled on the top face of the main body to let two long screws move up and down. To attach the springs firmly into place two shallow holes are cut from the upper face of the main body.

The embedded springs not only must provide the vertical displacement for the hip joint, but also must act as a shock absorber against the ground reaction impact. In order to choose a correct spring, stiffness of the spring is calculated using Hooke's Law:

$$F = k.x$$

$$k = F / x \qquad (3.1)$$

Since there are two spring, each springs need to resist half of the Ground Reaction Force (GRF). The hip vertical stroke, h, can be obtain through gathered data using reference [8]. Therefore, (3.1) can be re-expressed as

$$k = \frac{(GRF/2)}{h} \qquad (3.2)$$

The displacement of the spring is equal or less than the displacement of the hip joint, which is 53mm. The ground reaction force is 789N. Therefore, the optimal stiffness of the spring is 7.45N/mm. Unfortunately, there is no standard compression spring available with the same stiffness. Instead, two off-the-shelf springs, Lee Spring Part Number: LC 120M 06 M, are used. This spring has solid length of 25.374mm and free length of 63.500mm, and provides a spring force of 346 N at the solid height.
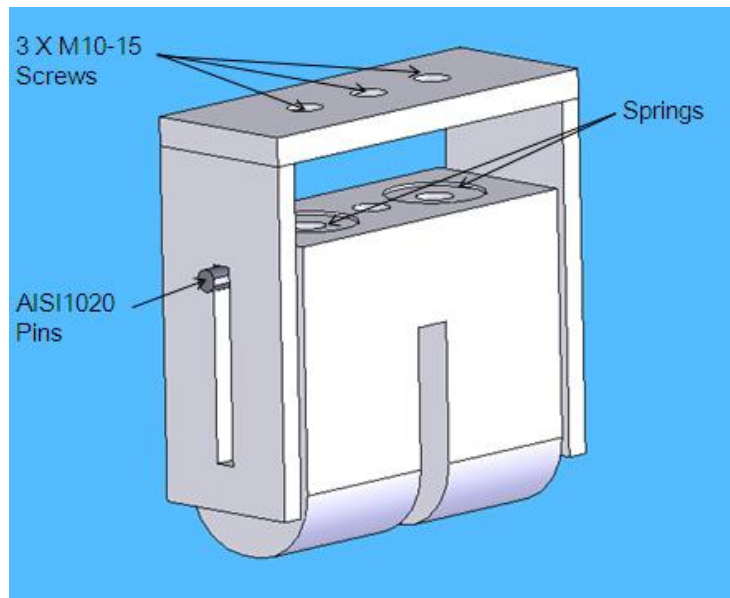
Figure 3-2: 3D CAD model of hip unit

3.4 Femoral Linkage

The femur is depicted in Figure 3-3 in red. One end of the femur is round in shape and acts as the hip joint; this end is inserted in the main body of hip unit. The other end is bolted to the APK. The yellow link acts as the pivot for the pneumatic cylinder. The pneumatic system is connected to the femur through this link.
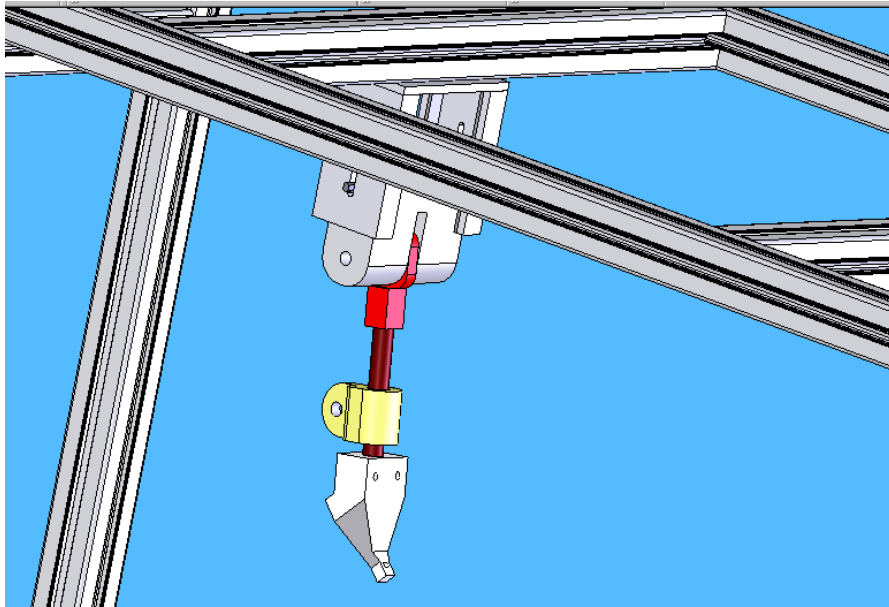
Figure 3-3: Hip joint assembly attached to test stand, femur link is marked by red

3.5 The Femoral Pneumatic System

A pneumatic cylinder is used to provide locomotion for the femoral component. The total range of motion of the femur is set to ±30 degrees. The femur, pneumatic cylinder, and frame constitute a three linkage mechanism with a variable length link. Hence, the reciprocal motion of the piston leads to rotary motion of the femur around its pivot (Figure 3-4). As a result, the knee is able to move back and forth with respect to the main body above the hip.
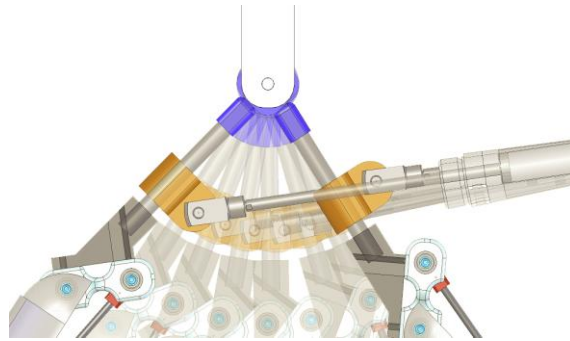
Figure 3-4: The femur is actuated by the pivot piston

To provide an automated reciprocal movement with variable speed for the piston, a fully pneumatic circuit is developed (Figure 3-5). One 5/2 – double remote air pilot – valve (V2) is used to control the air flow direction to the double acting pneumatic cylinder (C1). Two flow control valves or throttle valves (FLC1-2) are installed at the outflow of the cylinder to reduce its speed. The automated back and forth motion of the piston is provided by two 3/2 – one way air pilot – one way spring return – valves (V3-4). One 3/2 valve (V1) – controlled by a lever – is used as the flow shut-off valve to switch the whole circuit ON or OFF.

The indicated pneumatic circuit shows the normal or initial condition of the system before V1 becomes activated. As soon as the user pushes the lever, flow passes through V3, V4, V2, and FLC2; both pilots of V2, 12 and 14, become pressurized; however, V2 remains un-actuated due to the identical pressure for pilot lines 12 and 14. Since C1 is fully retracted, after a while, pressure in the supply line builds up and pilot 110 of the 3/2 valve (V4) is activated. As a result, the force generated by the pressurized pilot overcomes the spring force. Therefore, the flow is blocked in V4 and the pilot 12 of V2 is will be connected to the atmosphere. Consequently, the pressurized pilot 14 cause V2 to switch over and extend C1. When the position of V2 is changed, the pilot line of V4 (110) connects to the atmosphere and the spring returns V4 to it neutral position. The pilot line 12 of V2 becomes pressurized again; however, the position of V2 remains unchanged because of identical pressure at 12 and 14. As soon as the cylinder hits the end, the pressure in the extension part of C1 builds up, V3 switches over, pilot line 14

becomes un-energized, and thus, V2 switches over and retracts C1. This automatic back and forth motion continues until V1 is deactivated.

The main flaw of the circuit used is the non-adjustable spring force of V3 and V4. Due to this issue if the opposite force acting on the cylinder increases, the built up pressure cause the cylinder to retract before reaching its stroke. The circuit must be modified in a way to adjust the threshold pressure applied to V3 and V4.
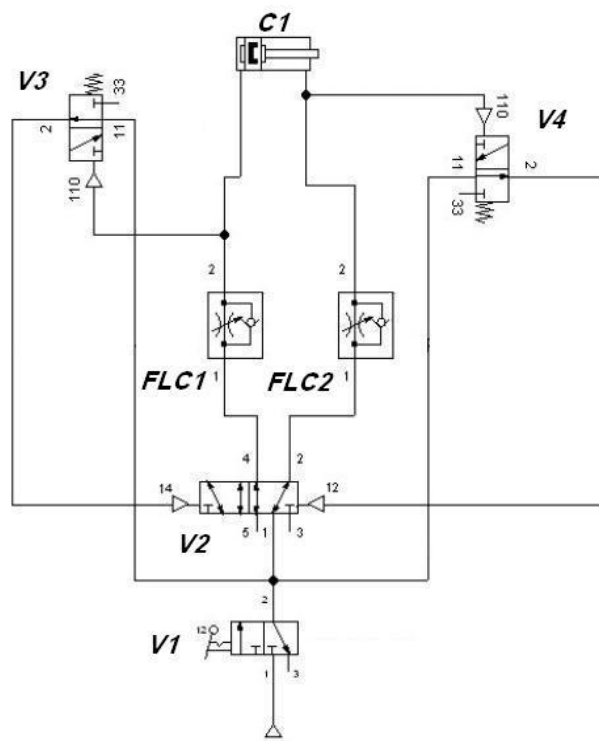
Figure 3-5: The pneumatic circuit used to provide automatic reciprocal motion for the femur link. The italic letters indicate the component number.

3.6 Treadmill System

Since the designed hip unit does not provide the horizontal movement, one treadmill must be used underneath the foot of APK to not only provide the relative horizontal motion, but also to simulate the ground reaction force. A commercial treadmill is modified and

embedded in the test-rig. The actual photo of the track is shown in Figure 3-6(a). The thickness of the track is 20mm. A new height adjustable frame (made of steel) is constructed to support the treadmill track as shown in Figure 3-6(b). To minimize fabrication effort, standard off-the-shelf hollow hot rolled steel beams were used to build the treadmill frame.
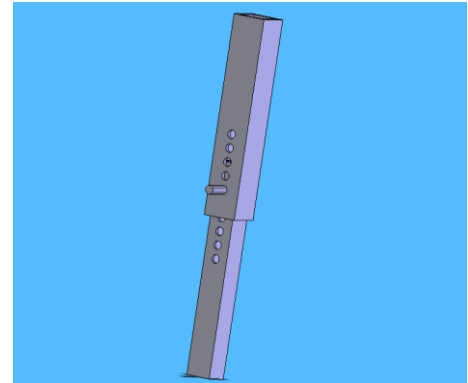
(a)   (b)

Figure 3-6: Treadmill and its frame (a) Top View of Treadmill Track (b) Designed frame for the treadmill, the small cylindrical rod represent a steel bolt that would be inserted to fix the height.

3.7 Discussion

The most important purpose of the test-bed is to replicate the lower limb motion. Moreover, the test stand provides a platform for running experiments. The designed test-bed mobilizes the femur, provides vertical displacement for the hip joint, and produces relative motion of the entire leg in respect to the ground in sagittal plane. Hence, the abduction and adduction motions of the hip joint in coronal plane were neglected in designing the test-bed.

However, this test bed is the first tried prototype and still needs additional design effort. The main problem exists in the hip unit and the spring intended to mimic the sinusoidal motion for the pelvic. The spring can provide the highest position of the hip at the mid stance when the foot has a complete contact with the treadmill. However, during swing phase, when the leg must be on the air, the hip joint will be at its lowest position due to the gravity. This contradicts the real case. In the swing phase of human walking cycle, the

pelvic is not at its minimal vertical position since the other leg, which is in stance phase, holds the pelvis up. Therefore, in reality, the sinusoidal path on plane of progression is lowest in double support. This deficiency of the hip unit leads to lack of foot clearance during mid/terminal swing phase. We can partially overcome this drawback by bending the knee more than usual during the mid/terminal swing phase, yet the foot will not be able to mimic the heel contact properly.

The author proposes to use an active system to provide motion for the hip joint such as crank mechanism (Figure 3-7) used to generate motion in an internal combustion engine. The fly-wheel shaft can be connected to a rotary electro-motor. By utilizing this electrical motor, the pelvic remains up during the swing phase. The author proposes to add this endeavor to the future work of this thesis.
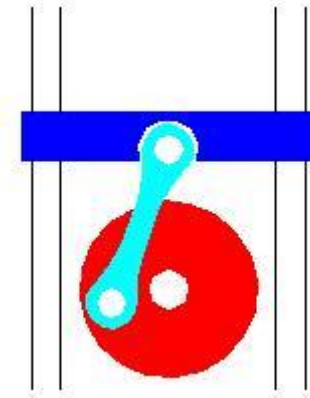
Figure 3-7: Piston-crank mechanism

Chapter 4

DYNAMICS

4.1 Introduction

The main objective of this chapter is to derive the system of second-order ordinary differential equations (ODE) governing the motion of the human leg/prosthetic leg. A human leg or prosthetic leg can be modeled as a serial manipulator with rigid links. In this case, the equations of motion can be obtained readily. To obtain the equations of motion for a system with serial kinematic chain, two methods can be used: Newton-Euler and Lagrangian formulation.

Both Newton-Euler and Lagrangian formulation are equivalent and give similar equations of motion. The Newton-Euler is based on Newton's Second Law of Motion, and on analysis of forces and moments of constraints acting between adjacent links. The resultant equations include the coupling forces and moments, and thus extra mathematical procedures are demanded to eliminate these extra terms. Conversely, the straightforward Lagrangian formulation is an energy-based approach to dynamics and automatically all

workless forces such as internal forces are ignored in this approach. Hence, Lagrangian dynamics is simpler than Newton-Euler. Therefore, Lagrangian formulation is utilized in this work to drive the equation of motion and solve the inverse dynamics of the system which is essential for torque control of actuators.

4.2 Dynamic Model Derivation by Lagrangian Formulation

In an inverse dynamic model of a robotic system, the inputs are the desired trajectories that refer to a time history of the given position, velocity, and acceleration of each joint. Using the knowledge of these histories, the torque/force required to be applied at different actuated joints are determined as the output of such inverse dynamic model.

4.2.1 Simplified Model of Human Lower Limb by Fixed Ankle

Figure 4-1 (a) illustrates the simplified model of human leg. As indicated, a sinusoidal motion is considered for pelvis. The other assumptions in this model are i) that the joint center of rotation is a fixed position point, ii) that the center of mass in each segment is fixed iii) that the segments are rigid bodies, and iv) the mass of the trunk is neglected. The reason for the last assumption will be discussed in the next section.

In Figure 4-1(a), r_1 and r_2 are the distance between the center of mass of each link (thigh and shank) and its upper joint (hip and knee joint, respectively); L_1 and L_2 are the length of femur and tibia, respectively. Those dimensions can be found by the Anthropometric data for the lower body in section 1.3.1. θ_1 and θ_2 are angular position of femur and tibia with respect to the global y-axis. Therefore, if the trunk is considered to be completely vertical, the hip angle is equal to θ_1, and knee angle is the relative angular position of thigh and shank; in other words

$$\theta_{\text{hip}} = \theta_1$$
$$\theta_{\text{Knee}} = \theta_1 - \theta_2$$

The free body diagram of the model is depicted in Figure 4-1(b). Hip and knee torques,

which are imposed by forces acting through the tendons and ligaments, are presented by τ_1 and τ_2. F_1 and F_2 represent the horizontal and vertical components of ground reaction force applied at the Center Of Pressure (COP). The COP is the plantar position of vertical GRF. F_{a_x} and F_{a_y} represent the forces acting on the femoral head that are applied by the socket.

| (a) | (b) |
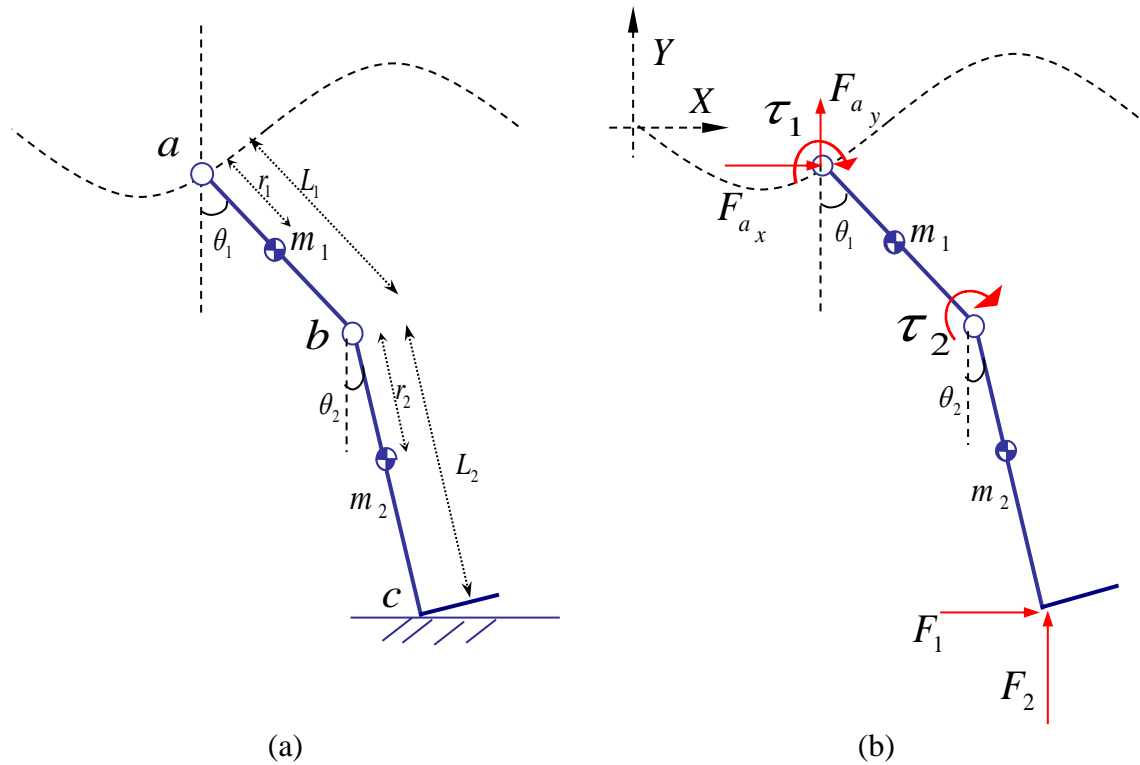
Figure 4-1: Human lower limb model: (a) the simplified model, (b) free body diagram

The hip joint, knee joint, and COP are labeled by a, b, and c, respectively, in Figure 4-1(b); and their positions can be defined as $(x_a \ y_a)$, $(x_b \ y_b)$, and $(x_c \ y_c)$ with respect to the global frame XY. As shown in Figure 4-1(b), the model of human lower limb can be simplified to a planar serial robotic manipulator. As described before, the inverse dynamics computation of this robot can be developed using the Lagrangian energy method. It is worth noting that in our case, the time history of position, velocity, and acceleration for the hip joint, point a, is predetermined from the gate cycle data.

Therefore, instead of considering the unknown applied forces F_{a_x} and F_{a_y} in deriving equations of motion, the known kinematic parameters of point a ($x_a, y_a, x'_a, y'_a, x''_a,$ and y''_a) are used. Hence, in the following calculations, F_{a_x} and F_{a_y} are not involved.

To utilize the Lagrangian method, the Cartesian coordinates of center of mass for each link, (x_1 y_1) and (x_2 y_2), are defined as

$$x_1 = x_a + r_1 \sin \theta_1$$
$$y_1 = y_a - r_1 \cos \theta_1$$

(4.1)

$$x_2 = x_a + L_1 \sin \theta_1 + r_2 \sin \theta_2$$
$$y_2 = y_a - L_1 \cos \theta_1 - r_2 \cos \theta_2$$

(4.2)

All angular and linear positions are time dependent. In other words $x_j = x_j(t)$, $y_j = y_j(t), \theta_i = \theta_i(t)$ where $j = 1, 2, a$ and $i = 1, 2$. However, to simplify the notations in the forgoing and following equations, term time, t, is omitted. The time derivative of displacement of center of mass for each link is calculated according to (4.3) and (4.4).

$$\frac{d}{dt} x_1 = x'_a + r_1 \theta'_1 \cos \theta_1$$
$$\frac{d}{dt} y_1 = y'_a + r_1 \theta'_1 \sin \theta_1$$

(4.3)

$$\frac{d}{dt} x_2 = x'_2 = x'_a + L_1 \theta'_1 \cos \theta_1 + r_2 \theta'_2 \cos \theta_2$$
$$\frac{d}{dt} y_2 = y'_2 = y'_a + L_1 \theta'_1 \sin \theta_1 + r_2 \theta'_2 \sin \theta_2$$

(4.4)

The time derivative of each time-dependent variable like $f, \frac{df}{dt}$, is indicated by prime, f', for simplicity. The kinetic energy of the whole system, T, is the summation of kinetic energy of individual links, and can be written as

44

$$T = \tfrac{1}{2} m_1 (x_1'^2 + y_1'^2) + \tfrac{1}{2} I_1 \theta_1'^2 + \tfrac{1}{2} m_2 (x_2'^2 + y_2'^2) + \tfrac{1}{2} I_2 \theta_2'^2 \tag{4.5}$$

The first two terms in (4.5) are the kinetic energy of first link due to the linear and angular velocity of the first link's (femur) center of mass. The last two terms represent the kinetic energy of the second link (tibia).

The total potential energy of system, U, can be obtained by

$$U = m_1 y_1 g + m_2 y_2 g \tag{4.6}$$

As indicated in (4.6), the total potential energy is the sum of the potential energy of each link.

The Lagrangian, L, is a scalar function that is defined as the difference between kinetic and potential energy of the mechanical system. In other words,

$$L = T - U \tag{4.7}$$

The equations of motion for the manipulator are derived using the Lagrangian in (4.7) an the following:

$$\mathbf{Q}_{total} = \frac{d}{dt}\left(\frac{\partial L}{\partial q'} \right) - \frac{\partial L}{\partial q} \qquad q = \theta_1, \theta_2 \tag{4.8}$$

where Q is the non-conservative generalized forces. All forces and moments applying on the links except gravity, constrains forces, and internal forces are considered as the generalized forces. In the case under study, hip and knee torques are applied to each joint (τ_1 and τ_2) and the ground reaction force is applied to the endpoint (point c). The generalized forces can be obtained using the theory of virtual work, δW, [25]. Thus:

$$\mathbf{Q}_{total} = \begin{bmatrix} \dfrac{\delta W}{\delta \theta_1} \\[2mm] \dfrac{\delta W}{\delta \theta_2} \end{bmatrix} = \begin{bmatrix} \tau_1 - \tau_2 \\ \tau_2 \end{bmatrix} + \mathbf{J}^T \begin{bmatrix} F_1 \\ F_2 \end{bmatrix} \tag{4.9}$$

where **J** is called Jacobian matrix which is the differential relationship between the joint displacements and end-effecter position, $(x_c \quad y_c)$. The components of the Jacobian are the partial derivatives of end-point Cartesian position with respect to joint displacement. Thus, they depend on the manipulator configuration. The Jacobian matrix for the serial system in Figure 4-1 is computed in (4.10).

$$\mathbf{J} = \begin{bmatrix} \dfrac{\partial}{\partial \theta_1} x_C & \dfrac{\partial}{\partial \theta_2} x_C \\ \dfrac{\partial}{\partial \theta_1} y_C & \dfrac{\partial}{\partial \theta_2} y_C \end{bmatrix} = \begin{bmatrix} L_1 \cos \theta_1 & L_2 \cos \theta_2 \\ L_1 \sin \theta_1 & L_2 \sin \theta_2 \end{bmatrix} \tag{4.10}$$

Substituting (4.8) and (4.10) in (4.9) the torque vector can be found by (4.11).

$$\begin{bmatrix} \tau_1 - \tau_2 \\ \tau_2 \end{bmatrix} = \begin{bmatrix} \dfrac{d}{dt}\left(\dfrac{\partial L}{\partial \theta_1'}\right) - \dfrac{\partial L}{\partial \theta_1} \\ \dfrac{d}{dt}\left(\dfrac{\partial L}{\partial \theta_2'}\right) - \dfrac{\partial L}{\partial \theta_2} \end{bmatrix} - \begin{bmatrix} L_1 \cos \theta_1 & L_1 \sin \theta_1 \\ L_2 \cos \theta_2 & L_2 \sin \theta_2 \end{bmatrix}\begin{bmatrix} F_1 \\ F_2 \end{bmatrix} \tag{4.11}$$

Substituting (4.3) and (4.4) in (4.5); and (4.1) and (4.2) in (4.6); and rewriting (4.11) we can obtain the applied torque at each joint. The hip and knee torque expressions can be written as

$$\begin{aligned}
\tau_1 &= m_1 r_1 \left[r_1 \theta_1'' + x_a'' \cos \theta_1 + y_a'' \sin \theta_1 + g \sin \theta_1 \right] + \\
&\quad m_2 L_1 \left[L_1 \theta_1'' + x_a'' \cos \theta_1 + y_a'' \sin \theta_1 + g \sin \theta_1 \right] + \\
&\quad m_2 r_2 \left[-r_2 \theta_2'' + g \sin \theta_2 + x_a'' \cos \theta_2 + y_a'' \sin \theta_2 \right. \\
&\quad \left. + L_1\left(\theta_1'' + \theta_2''\right)\cos\left(\theta_1 - \theta_2\right) + L_1\left(\theta_1'^2 + \theta_2''\right)\sin\left(\theta_1 - \theta_2\right) \right] + \\
&\quad I_2 \theta_2'' + I_1 \theta_1'' - L_2 F_1 \cos \theta_2 - L_1 F_1 \cos \theta_1 - L_2 F_2 \sin \theta_2 - L_1 F_2 \sin \theta_1
\end{aligned} \tag{4.12}$$

$$\begin{aligned}
\tau_2 &= m_2 r_2 \left[r_2 \theta_2'' + x_a'' \cos \theta_2 + y_a'' \sin \theta_2 + L_1 \theta_1'' \cos\left(\theta_1 - \theta_2\right) - L_1 \theta_1'^2 \sin\left(\theta_1 + \theta_2\right) \right. \\
&\quad \left. + g \sin \theta_2 \right] + I_2 \theta_2'' - L_2 F_1 \cos \theta_2 - L_2 F_2 \sin \theta_2
\end{aligned} \tag{4.13}$$

It is worth to note that the center of pressure is not constant during walking cadence, and it is varying along the foot (from heel to forepart). Therefore, the Jacobian matrix is not constant in terms of the length of the end-point with respect to the knee joint.

4.2.2 Motion Equations for the Fabricated Prototype

Figure 4-2(a) presents the planar model of the prototype. F_{a_y} is the spring force and F_{a_x} and is the constrain force apply from the hip unit since this part acts as a sliding mechanism. As described in Chapter 2, the knee joint becomes activated by embedding a ball-screw inside the leg (link *ef*), and the femur is actuated by a pneumatic cylinder (link *hd*). The new introduced dimensions are L_d : the distance between hip joint and the cylinder connection (*ad*), L_e : the distance from hip to screw connection on the femur link (*ae*), L_f : the distance between knee joint and ball-screw connection (link *bf*).

(a)   (b)
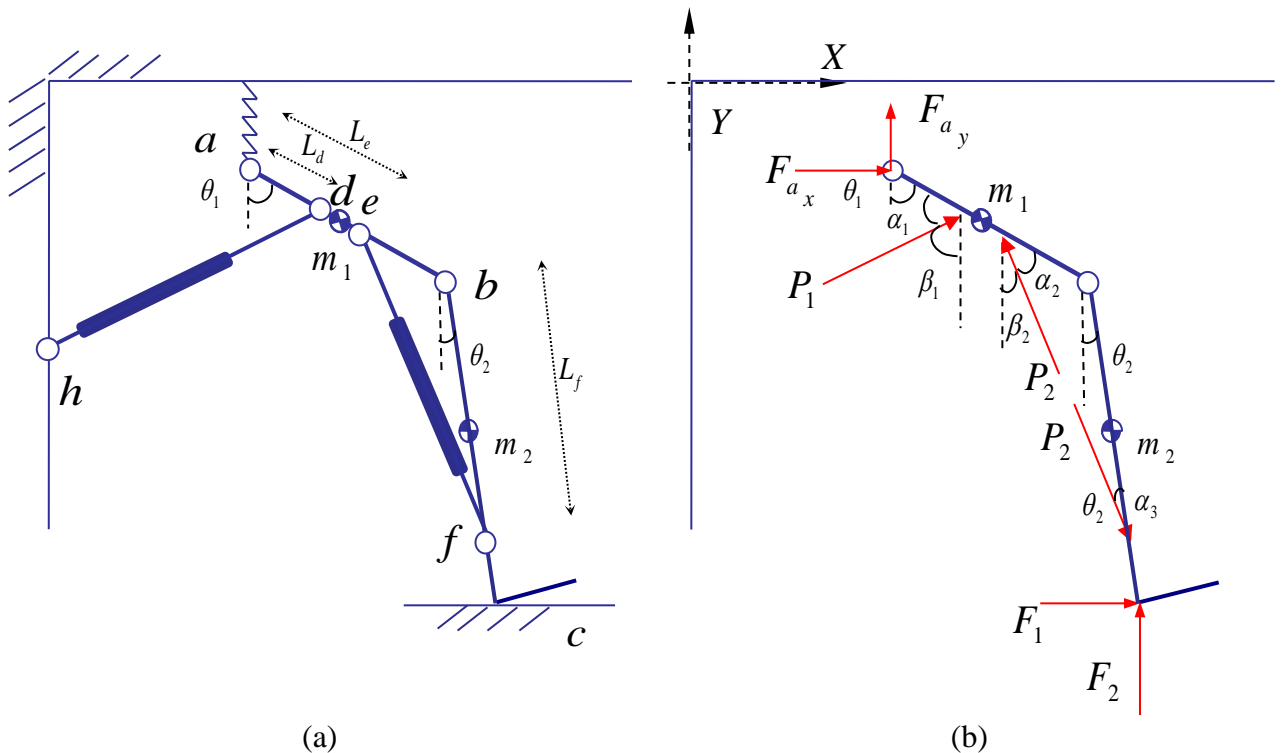
Figure 4-2: Planar model of fabricated prototype: (a) simplified model, (b) its free body of diagram

The angles in Figure 4-2 are: β_1: the inclination angle of pneumatic cylinder in respect to y-axis, β_2: the inclination angle of ball-screw in respect to y-axis, α_1: the angle between ad and hd, α_2: the angle between femur and ball screw, and α_3: the angle between tibia and ball screw. Figure 4-2(b) shows the free body diagram of the prototype. P_1 is the acting force from the pneumatic cylinder to the femur. The couple force P_2 is applied to femur and tibia link by the ball-screw.

As presented in Figure 4-2(b), the planer model of the designed leg can be modeled as a serial robot manipulator if the following assumptions are made:

i) the location of center of mass is constant for pneumatic cylinder and ball screw. However, in reality, due to motion of piston and screw the center of mass for these components are not fixed in place., ii) the mass of the cylinder and ball-screw are negligible.

With the aforementioned assumption, the prototype model becomes similar to the simplified model of human leg in Figure 4-1 while instead of applying the hip and knee torque directly to the joints, P_1 and P_2 are acting on the corresponding links. The applied torque to the hip and knee joints (τ_1 and τ_2, respectively) can be derived as

$$\tau_1 = L_d P_1 \sin \alpha_1 + L_e P_2 \sin \alpha_2 \tag{4.14}$$

$$\tau_2 = L_f P_2 \sin \alpha_3 \tag{4.15}$$

The correlation between β_1, α_1, and θ_1 can be obtained by

$$\alpha_1 = \pi - (\beta_1 + \theta_1)$$

where

$$\beta_1 = \tan^{-1}\left(\frac{x_h - x_d}{y_h - y_d}\right)$$

The correlation between β_2, α_2, α_3, and θ_2 can be obtained by

$$\beta_2 = \tan^{-1}\left(\frac{x_f - x_e}{y_f - y_e}\right)$$
$$\alpha_2 = \theta_1 - \beta_2$$
$$\alpha_3 = \beta_2 - \theta_2$$

Equations (4.14) and (4.15) can be represented in matrix format as shown in (4.16) where P_1 and P_2 are expressed based on τ_1 and τ_2:

$$\begin{bmatrix} P_1 \\ P_2 \end{bmatrix} = \begin{bmatrix} L_d \sin\alpha_1 & L_e \sin\alpha_2 \\ 0 & L_f \sin\alpha_3 \end{bmatrix}^{-1} \begin{bmatrix} \tau_1 \\ \tau_2 \end{bmatrix} \qquad (4.16)$$

The torque vector $[\tau_1 \ \tau_2]^{\mathrm{T}}$ can be obtained using (4.12) and (4.13).

4.3 Discussion

In this chapter, the equations of motion for the simplified human model and the APK prototype were derived by utilizing Lagrangian method. Since, the actual mathematical dynamic model of human walking is complex and nonlinear, it is not possible to control the prosthetic just by using traditional controller such as PID. Fuzzy logic can provide us a knowledge-based system that makes us independent from equations of motion. In the following chapter (control), fuzzy inference systems are utilized to control the prosthetic actuator, and thus the equations of motion for the human walking are not used. However, equations of motions are derived in this chapter to enable the reader to design model-based controller for APK. In addition, without having real model, we can examine the performance of different controller on the obtained mathematical model in simulation.

In the case of using classical method to control the APK, much accurate modeling is required to derive the equations of motion, such as considering the ankle as an active joint, the trajectory path of the center of pressure during stance phase, and the damping and stiffness of each joint.

Chapter 5

SENSING SYSTEM

5.1 Introduction

The objective of this chapter is to develop a sensing system that can capture sensory signals from the user's able leg. The sensory signals will serve as input data to a microcontroller that will compute the necessary command knee torque required to drive the actuator of the prosthesis to replicate the human locomotion.

Two different types of input signals are investigated in this chapter: electromyography (EMG) and the inclination angle. The methodologies to measure each type of signal are described, and finally a comparison between the different sensing methods is provided to identify the most suitable approach to acquire sensory information from the subject's able leg.

5.2 Electromyography (EMG)

In a normal walk, lower limb muscles contract and relax in an orchestrated fashion. Figure 5-1 presents phasic action of major muscle groups in a gait cycle. As depicted, during each sub-phase of the gait cycle, some of the muscles are activated while the others are at rest. This harmonic pattern of contraction and relaxation of lower limb muscles can be utilized to provide information for the controller of the prosthesis.
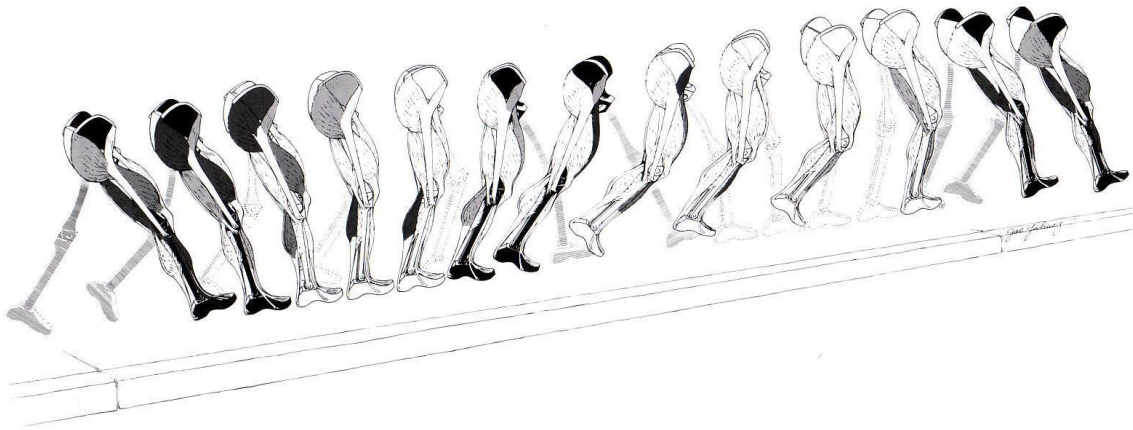
Figure 5-1: Phasic action of major muscle groups [6]. As it shown in these figures, the most activity of muscles is during the initiation of the swing phase and stance phase (or end of the stance phase). This implies that the muscles are mostly involved in accelerating and decelerating the leg during the walking cycle.

EMG analysis is a non-invasive technique that can give information about muscle physiology. This method can measure the electrical output voltage generated during muscle contraction. Currently, EMG is a popular technique in rehabilitation such as recognizing neural injuries. Moreover, there are quite a few researches that utilized EMG signals from either remnant muscles of the stump or muscles of the healthy leg to control either a prosthetic or an assistive leg [26], [20].

When a motor unit becomes activated, a depolarization of muscle membrane occurs that produces a detectable voltage. This voltage is called motor unit action potential (m.u.a.p) which is a specific attribute of that motor unit. Motor unit is the functional and anatomic grouping of all the muscle fibers innervated a single motor neuron (Figure 5-2). Details

of muscle fibers are out of the scope of this research; however, the reader can be referred to reference [6] for more details.
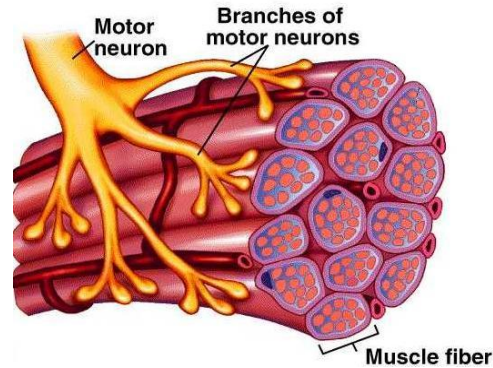
Figure 5-2: Motor unit [27]

The EMG signal is an algebraic summation of all motor unit action potentials that are activated at that moment [31]. The amplitude of the EMG signal is correlated to the force generated by the muscle of interest. If the number of motor units that are activated increases to reach the demanding force, the magnitude of the extracted EMG signal rises as well [6].

Typically, there are two types of electrodes for measuring EMG signals: Indwelling and Surface electrodes. Indwelling electrodes that use invasive needles are suitable for measuring signals from deep muscles. In this study, surface electrodes, which are attached to the skin to measure electrical activity, are selected since they are more convenient and more repeatable for day-to-day use. In addition, surface electrodes can cover wider area of muscles.

Surface electrodes are used in pairs to detect the voltage from two different locations on the muscle. A ground electrode (the third electrode) identifies any other signals from the environment that the subject may have conducted with. The voltage recorded from sensors usually has a maximum amplitude of 5mV peak to peak;` therefore, these reading signals must be fed into a differential amplifier in order to amplify the reading of the voltage difference between two electrodes. Moreover, the differential amplifier improves the specificity of the EMG signal by reducing the sensitivity to noise.

52

Literature reports on different methods to process raw EMG signals to obtain a pattern for each voluntary movement [28]-[29]. The methodology adopted in this research was proposed by Inman et al [30]. In this method as illustrated in Figure 5-3, the raw EMG signal is fully rectified and then passed through a low-pass filter. The cut-off frequency of the filter has been a controversial issue, and investigators reported different values for different activities. Many researchers investigate the EMG signal for muscles contractions during different phases of the gait cycle.
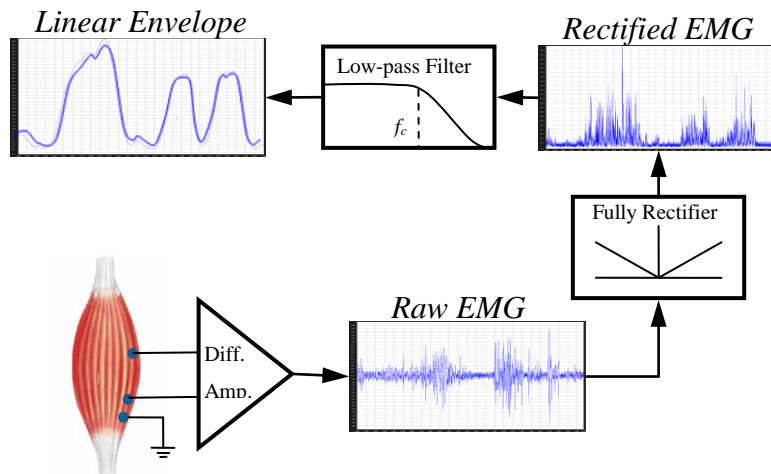
Figure 5-3: Linear envelope EMG process

Winter [31] provides the EMG linear envelope for different muscles during the walking cycle by utilizing a second-order low-pass filter with a 3-Hz cut-off frequency, as well as, the normalized data obtained for each stride. Figure 5-4 depicts the normalized EMG linear envelope for different activated muscles during one stride gathered by Winter [31]. The dotted lines show the variability in measured data due to different trials and varying subjects.
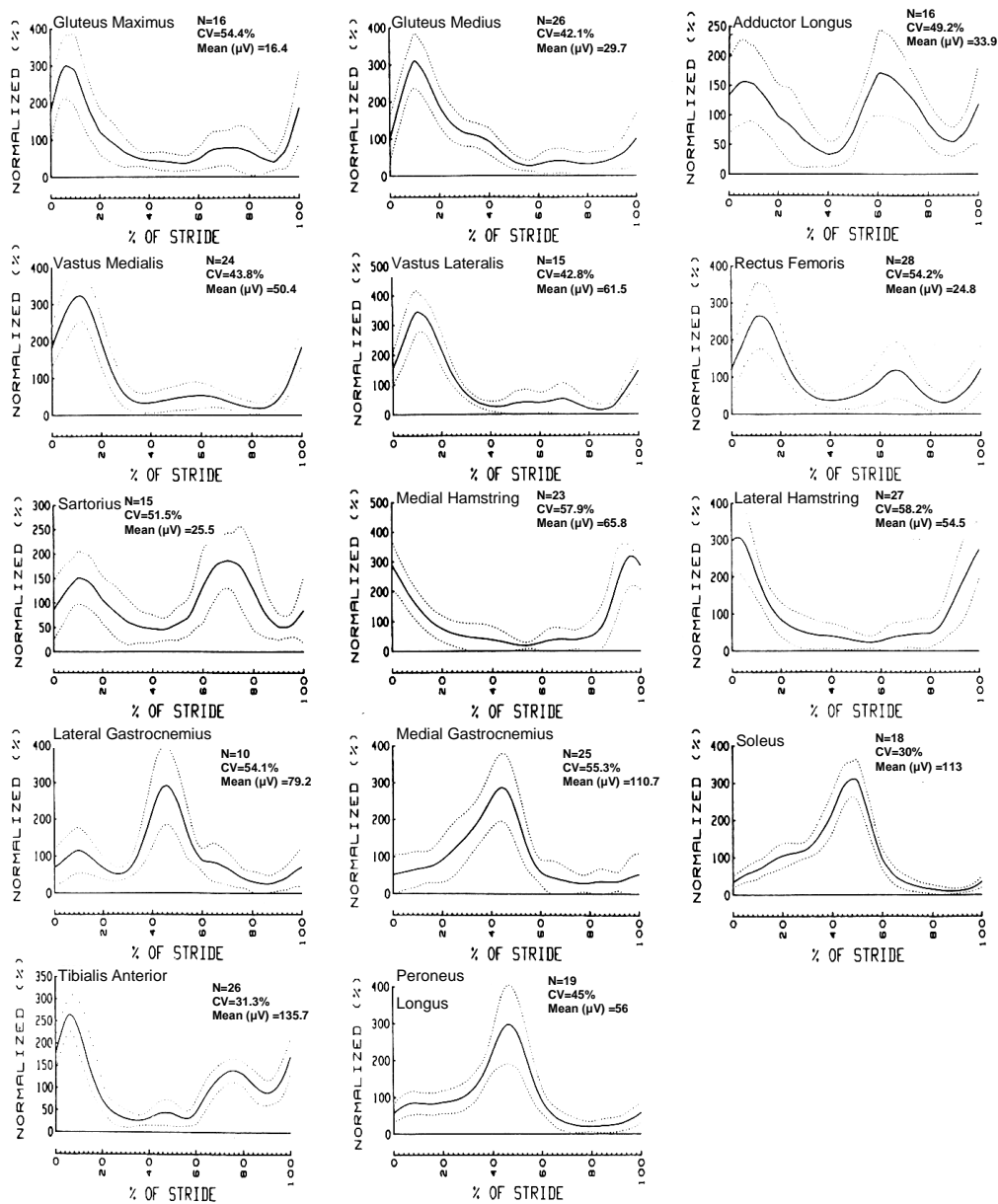
Figure 5-4: Average EMG profiles of lower limb muscles during one stride: Each subject's mean EMG was normalized to 100% prior to averaging. The distance of the pair of electrodes was set to 2cm to obtain these EMG signals [31].

In this research, we considered using these harmonic linear envelope EMG signals as references in a pattern recognition system to control the prosthetic leg. The input envelope EMG signal to the controller can be compared with the reference data obtained by the Winter's data, and the correlated output can be used to drive the APK actuator.

54

It is not convenient to record EMG signals from all the muscles listed in Figure 5-4 due to the complexity and cost. Therefore, only four muscles are selected as the source of the EMG signal: rectus femoris, vastus lateralis, semitendinosus (medial hamstring), and adductor longus. The location of these muscles is depicted in Figure 5-5.
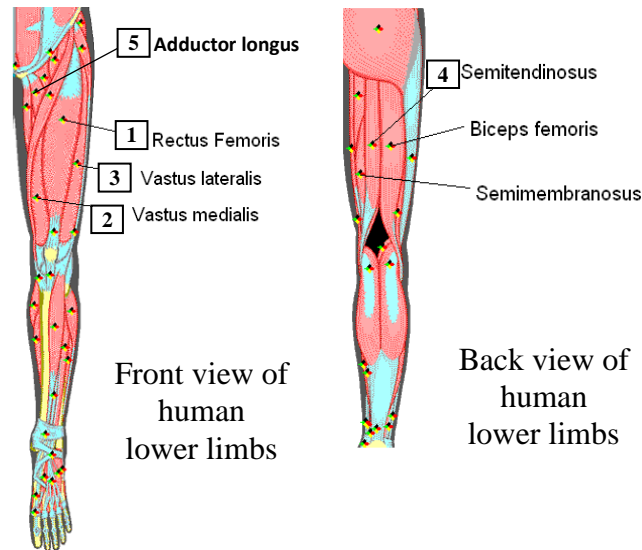
Figure 5-5: Location of selected muscles as the source of EMG signals to control the prosthesis.

The aforementioned muscles are chosen based on their different envelope EMG patterns. In other words, the extrema of the linear envelope EMG signal for different muscles must occur in different points. To gain a better perceptive of the different EMG patterns of the selected muscles, the linear envelopes of those muscles are illustrated on the same graph (Figure 5-6). The vertical dashed lines indicate the sub-phases of the gait cycle.

As illustrated in Figure 5-6, two summits exist in the rectus femoris' EMG envelope signal. This muscle is mainly activated during the end of the swing phase up to mid-stance. The EMG envelope reaches its maximum value during load response when it resists the knee flexion. The minor peak occurs at the initiation of the swing phase when the hip flexes to advance the swinging limb. The major activity of medial hamstring starts at the terminal swing phase to decelerate the leg and foot. It also involves in controlling the thigh rotation at heel contact. Adductor longus is the only selected muscle that has the

same level of major activity at two different periods within the gait cycle. Firstly, it helps hip muscles to accept the weight during the early stance period. Secondly, it assists rectus femoris to accelerate the leg at the beginning of swing period. The EMG of the vastus lateralis has the same trend as the EMG signal of the rectus femoris; however, the un-normalized EMG signal from the vastus lateralis has a much higher voltage magnitude.
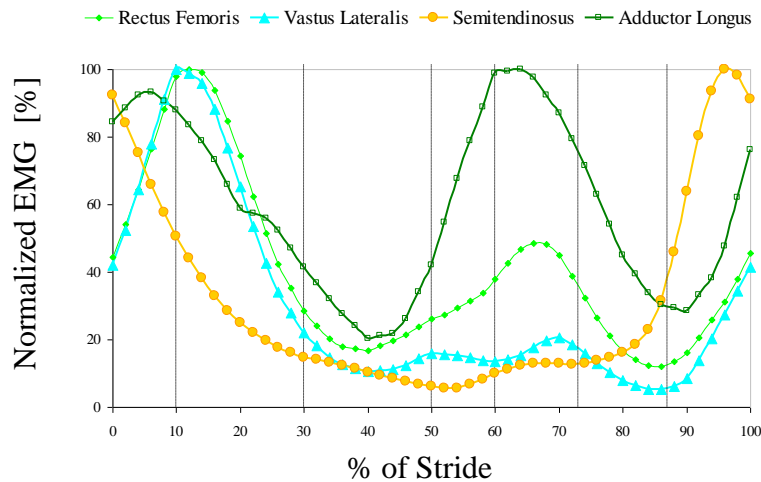
Figure 5-6: The normalized EMG linear envelope for four selected muscles: The variation of data due to different subjects and trials is not plotted in this figure. The solid lines represent the mean of the measured data.

The un-normalized EMG linear envelopes of the stated muscles are shown in Figure 5-7. The next section describes the process and the instruments utilized to record similar EMG signals from the chosen group of muscles.
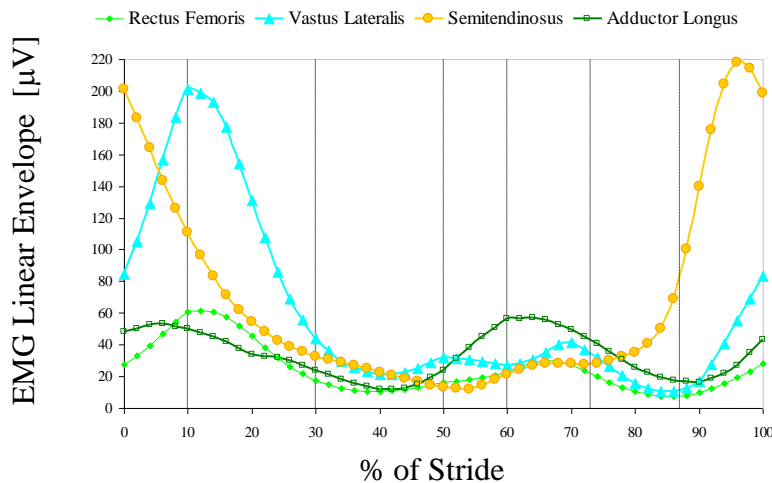
Figure 5-7: Un-normalized EMG linear envelope for selected muscles

5.2.1 Collection and Processing of EMG Signals

Surface EMG electrodes require very fine skin contact; therefore, to reduce the skin impedance, each electrode site is rubbed with a 50/50 water/ethanol solution. The electrodes are placed 4cm apart (center to center). The setup of electrodes during the experiment is illustrated in Figure 5-8. The chosen Surface EMG electrodes are plastic encased silver/silver chloride electrodes that have a very low DC offset potential, minimal motion artifact, and good low frequency response. An EMG bio-amplifier (differential amplifier), model AMT-8, Bortec, is set up to feed the raw EMG from the selected muscle group to the Analog to Digital Converter system (ADC). The gain of the amplifier (common-mode rejection ratio 115dB at 60Hz) is set to 100. It was assured that the gain is not too high in order to avoid saturation; moreover, the sample rate of 1024 Hz was selected for the 12 bit ADC based on the Nyquist–Shannon sampling theorem. The range of frequency for the surface EMG signal is 10-500 Hz and the majority of the signal power is concentrated between 20 and 200Hz [31]. A National Instrument ADC board was used to collect data coordinated with NIAD software on the PC. The recorded EMG signals are shown in Figure 5-9. Compared to Figure 5-7, the obtained EMG signals had a very similar trend to the data gathered by Winter. For instance, the vastus lateralis and the medial hamstring have the highest voltage values and their peaks are after one another. The adductor longus has two main bursts of activity at the mid stance and initial swing phase.
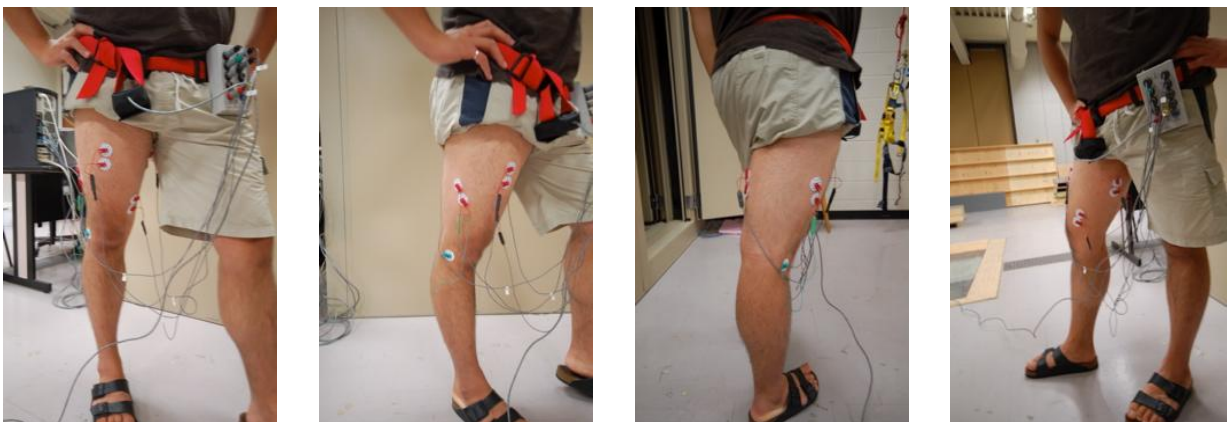
Figure 5-8: Setup of electrodes during the experiment. Instead of allocating one electrode as ground for each muscle, one electrode was devoted as the ground for all the muscles (marked in green).
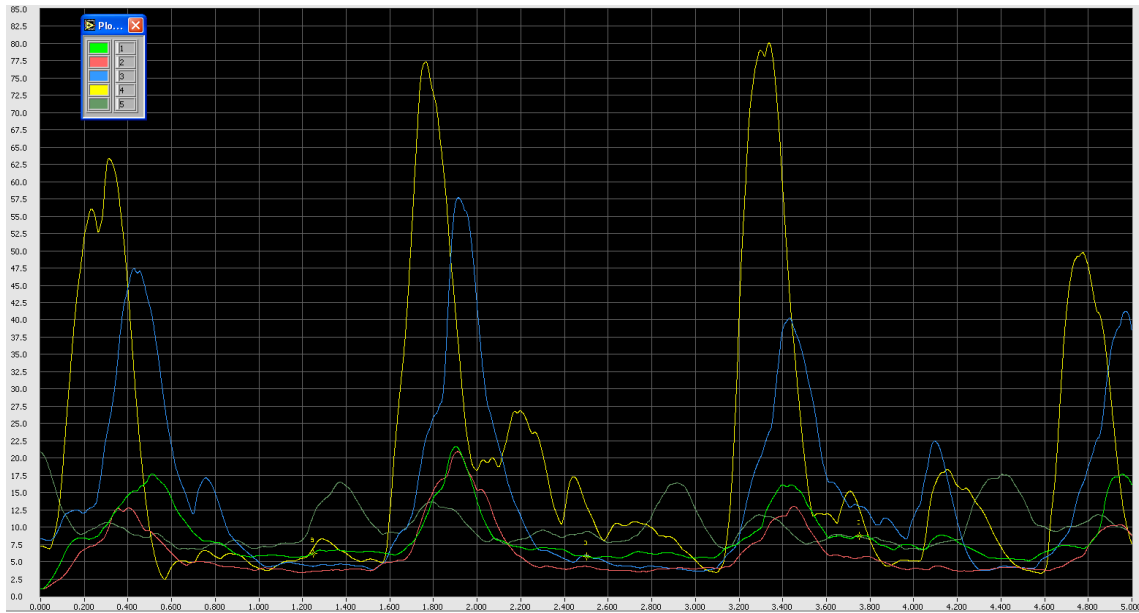
Figure 5-9: Recorded un-normalized linear envelope EMG. Channel#1: rectus femoris (light green), channel#2: vastus medialis (pink), channel #3: vastus lateralis (blue), channel#4: semitendinosus (yellow), and channel#5 adductor longus (dark green). The activation of one extra muscle (channel#2) is recorded although based on aforementioned description we do not require this signal for the inputs of the controller.
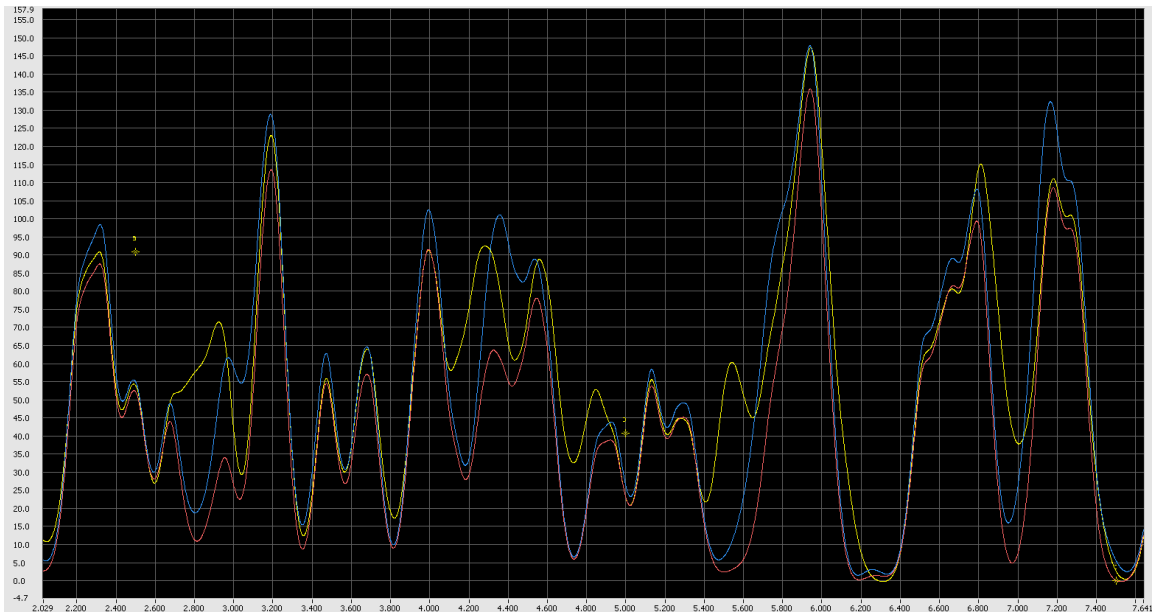
Figure 5-10: An example of cross-talk during one of the experiments

The main drawback of the EMG sensing methodology is that the position of electrodes can significantly alter the magnitude and harmonic contents of the read data. Surface electrodes are prone to cross-talk (pick up the signal from adjacent muscles). Therefore, mounting the EMG electrode at the correct position is highly crucial. Figure 5-10 demonstrates an example of cross-talk during one of the experiments. It is clear that three electrodes sense m.u.a.p's from the same active motor units.

In addition, the temperature and the fat tissue covering muscles can influence the reading EMG. Moreover, the EMG has high individual variability. Furthermore, as stated earlier, the raw EMG voltage is in the range of micro volts, which needs a very high quality amplifier and ADC to collect the data. This results in a need for bulky signal processing instrumentation. All the above makes EMG sensing not practical for our system, and therefore, we to seek for alternative methods of sensing system to extract healthy leg sensory inputs for the controller.

5.3 Lower Limb Motion (Inclination Angle)

The other harmonic characteristic of the gait cycle is the sagittal motion of the lower limbs. Figure 5-11 illustrates the inclination angle of the lower limbs (thigh and shank). Moreover, the path way of knee and hip joints are presented in this figure. This harmonic motion is repeatable and the position of the lower limb segments can be used as the inputs for the controller. The description of the lower limb joint angles is depicted in Figure 5-12.
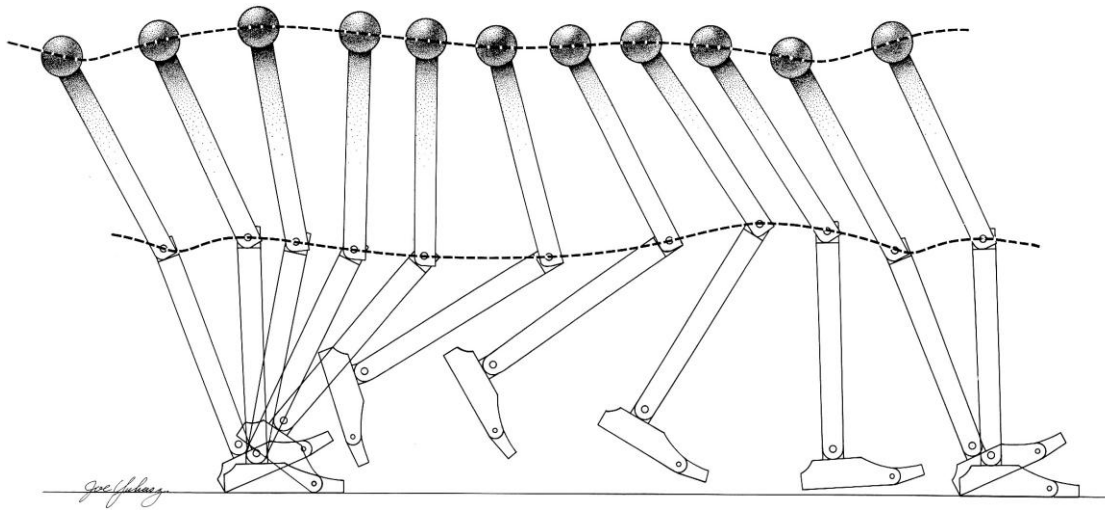
Figure 5-11: Lower limb motion during one stride

$$\theta_{\text{trunk}} \approx 90^o \quad \theta_{\text{hip}} = \theta_{\text{thigh}} - \theta_{\text{trunk}}$$

$$\theta_{\text{knee}} = \theta_{\text{thigh}} - \theta_{\text{leg}}$$

$$\theta_{\text{ankle}} = \theta_{\text{foot}} - \theta_{\text{leg}} - 90°$$

(a)   (b)
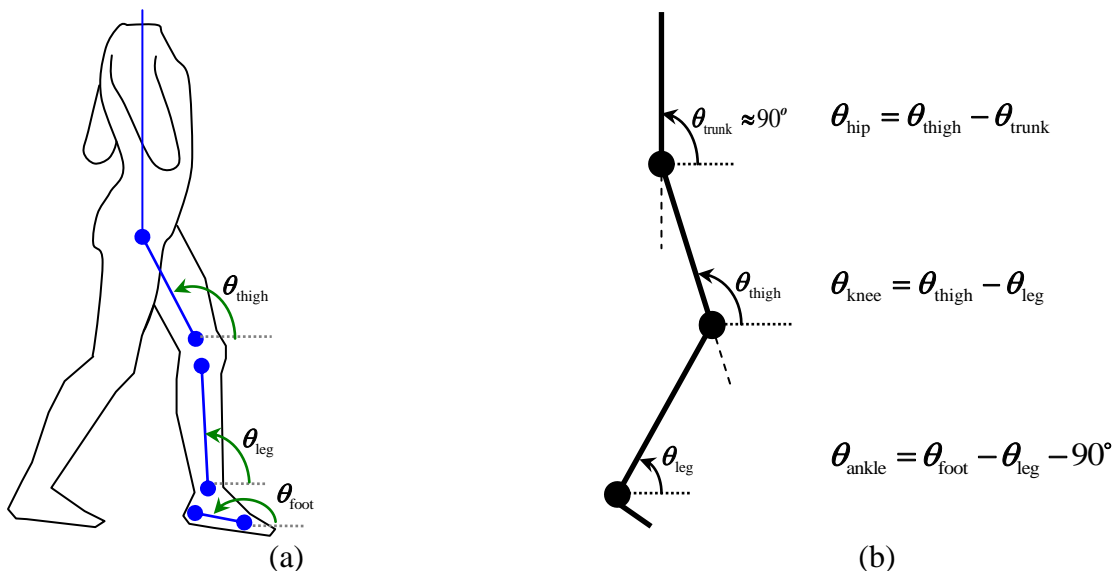
Figure 5-12: Definitions of the lower limb joint angles (a) inclination angle of thigh, shank, and foot (b) the correlation between lower limb joint angles and segments inclination angles with assumption that the joint center of rotation is a fixed position point.

The angle of the lower limb joints and segments are defined based on the reference [31] in Figure 5-12. When the knee is fully extended, it has zero degrees of flexion. When $\theta_{\text{thigh}} > \theta_{\text{leg}}$ the knee is flexed and when $\theta_{\text{leg}} > \theta_{\text{thigh}}$ the knee is extended.

60

5.3.1 Choosing Suitable Sensor for Reading Femur and Tibia Inclination Angle

This section discusses different methodologies investigated for measuring the femur and tibia inclination angles, i.e., inputs of the APK controller. The proposed systems need to be able to provide measurements in real-time that can be utilized by the control system. Technically, the system must be mobile, easily mountable, and utilizable for long term monitoring without interference to walking. To achieve this purpose, five combinations of sensors were tested: i) digital protractor, ii) combination of two accelerometer, iii) potentiometer, iv) potentiometer together with accelerometer, and v) gyroscope together with accelerometer. The advantages and disadvantages of each method are evaluated in the remainder of this section.

5.3.1.1 Digital Protractor

There are different methods to measure the kinematic values of the lower limb. The inclination angle of the femur and tibia can be measured by using a digital protractor. Two Pro 3600 Digital Protractors were mounted on each segment and the angular positions were recorded. A Pro 3600 can read all angles between 0° and 360°. It also has an RS-232 compatible digital output that interfaces with a microcomputer. The main flaw of the Pro 3600 is the low frequency of its output (15/8 Hz). Unfortunately, other digital protractors available on the market either do not cover enough range of motion or do not have high output frequency and precision. This deficiency forced the choice of another method to measure the shank and thigh inclination angles.

5.3.1.2 Combination of Two Accelerometer

Utilizing an accelerometer is a conventional industrial method for measuring inclination angle. The angular position of the plane of interest with respect to the ground can be acquired by reading the gravity component on the output axis of the accelerometer. In order to measure the femur and tibia inclination angles in the sagittal plane, one accelerometer must be mounted on each part. If the lower limb joints are fixed, the

angular position of the segments can be read precisely. As soon as the lower limbs start anterior/ posterior rotation around their joints, the normal $(r\omega^2)$ and tangential acceleration $(r\alpha)$ are applied to the sensors due to the rotary velocity and acceleration, ω and α respectively, where r is the distance between the sensor and the joint. Moreover, acceleration of the person in the direction of his/her movement during the walking cycle is applied to the sensors as well. As a result, obtaining the leg segments inclination angles during the walking cycle is far more complex than the situation of fixed lower limb joints. The difficulty in cancelling out the motion of the human body can be overcome by using two accelerometers with a one-axis methodology.

This method utilizes two accelerometers for each segment separated by a distance (D) to determine the angular acceleration and velocity. This approach is shown in Figure 5-13. Using this, the result can be integrated to find the angle travelled. The challenge in applying this method is that the leg will require occasional calibration. The methodology involves two accelerometers mounted a distance D $(r_2$-$r_1)$ apart as in Figure 5-13.
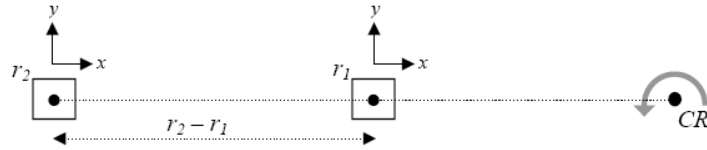
Figure 5-13: Accelerometers location on the rotary segment

If it is assumed that the human body does not have any acceleration, i.e., walking with a constant speed, the x axis of each accelerometer measures the normal acceleration as follows

$$a_{x_j} = \omega^2 r_j \tag{5.1}$$

where j is the accelerometer number index. Taking the difference between the two measurements gives

$$a_{x_2} - a_{x_1} = \omega^2 (r_2 - r_1) = \omega^2 D \tag{5.2}$$

Even if the subject does not move at a constant speed, his/her acceleration will have the same effect on both sensors. Then, equation (5.1) will be changed to

$$a_{x_j} = \omega^2 \, r_j + a_{\text{Trunk}} \cos \theta \qquad (5.3)$$

where θ is the inclination angle of the segment. The extra right-hand term in equation (5.3) is constant for both accelerometers mounted on the same segment. Therefore, subtraction of the two outputs results in cancelling out of the trunk acceleration.

From equations (5.2) and (5.3) above we can obtain the angular velocity:

$$\omega = \sqrt{\frac{\left| a_{x_2} - a_{x_1} \right|}{D}} \qquad (5.4)$$

In addition, the tangential acceleration can be determined by the y axis of each accelerometer:

$$a_{y_j} = \alpha \, r_j + a_{\text{Trunk}} \sin \theta \qquad (5.5)$$

The difference of the tangential acceleration of the output of the two sensors yields the result below:

$$a_{y_2} - a_{y_1} = \alpha (r_2 - r_1) = \alpha \, D$$

$$\alpha = \frac{a_{y_2} - a_{y_1}}{D} \qquad (5.6)$$

The only parameter needed to utilize the above method is the distance between the two sensors (D). The distance between each sensor and the joint center of rotation need not be known. A larger distance leads to better resolution of the angular measurements. Integrating ω will provide the magnitude of angle travelled, but the direction is unknown. The sign of the movement can be obtained from the integrals of the tangential accelerations. From equation (5.4), it is clear that if the angular velocity is increased, the

difference between the x axis reading of two accelerometers is increased too. In other words, for low angular velocity, the difference between the voltage outputs of two sensors is very low. This low voltage can be contaminated by noise. During the experiment, it was proved that this method is not feasible to measure leg angles for an activity like walking cycle since the anterior/posterior rotary speed of the leg segments around their joints is not fast enough.

The same deficiency applies with the y axis reading of sensors. When the leg has very low rotary acceleration, the voltage output of the y axis fluctuates around zero. Therefore, we cannot use this method for low acceleration since it relies on confidently knowing the sign (+/-) of α.

5.3.1.3 Potentiometer

The next method utilizes potentiometers to measure the shank and thigh inclination angles indirectly. Two sets of rotary potentiometer are mounted on the knee and hip joints. The two heads of the knee sensor are connected to the femur and tibia, and the hip sensor to the femur and trunk. Knee and hip flexion/extension cause the resistance to vary with respect to the travelled angle. This method provides a reliable measurement since external disturbance cannot affect the output. The main assumptions in this method are i) that the trunk is vertical (90 degree in respect to the ground), ii) that the joint center of rotation is a fixed position point, and iii) that the segments are rigid bodies.

The inclination angle of the femur and tibia can be determined from the following equations:

$$\theta_{Femur} = \theta_{Hip} + \theta_{Trunk} \tag{5.7}$$

Where $\theta_{Trunk} = 90^{o}$

$$\theta_{Tibia} = \theta_{Thigh} + \theta_{Knee} \tag{5.8}$$

This method is found to be promising; however, it is inconvenient for the user because the two links of the hip sensor must be attached to the femur and trunk.

5.3.1.4 Potentiometer together with Accelerometer

A convenient experimental setup composed of one accelerometer and one potentiometer was used for the next method. The potentiometer was used to measure the knee flexion/extension angle since attaching this sensor to the knee can be performed readily. The accelerometer was mounted on the femur to read its inclination angle. Comparing to the tibia, the femur has lower acceleration, momentum, and range of motion. As a result, there is less disturbance effect on the femur than the tibia. By assuming knee joint as a fixed point and perpendicular angle for the trunk, the tibia inclination angle can be obtained using equation(5.8).

To evaluate the disturbances of the accelerometer reading data, a comparison between accelerometer and potentiometer readings was carried out in Figure 5-14 for measuring the femur inclination angle simultaneously (the same segment for both sensors). A healthy 22-year-old male subject, whose height and weight were 180cm and 77Kg, respectively, participated in this test. To perform this experiment, the potentiometer and accelerometer were mounted on the hip joint and the femur, respectively.

At the beginning of the experiment, the subject stood for a few seconds so that the bias between the measuring angle and the reference on (Figure 5-14) could be identified. As shown in Figure 5-14, the potentiometer provides a smooth trend, whereas data read from the accelerometer has fluctuations. This oscillation becomes more distinct at the heel contact, where the impact of the ground reaction force distorts the accelerometers' reading. Moreover, it was observed that during fast walking, the oscillation of the accelerometer measurement exceeds the standard deviation of the reference line (dash lines in Figure 5-14). However, for normal and slow walking, the femur inclination angle obtained by the accelerometer is reasonable and can be used as one of the inputs to the APK control system.

It is worth noting that more precise accelerometer measurement can be obtained by selecting an accelerometer that has lower range of reading but higher sensitivity.
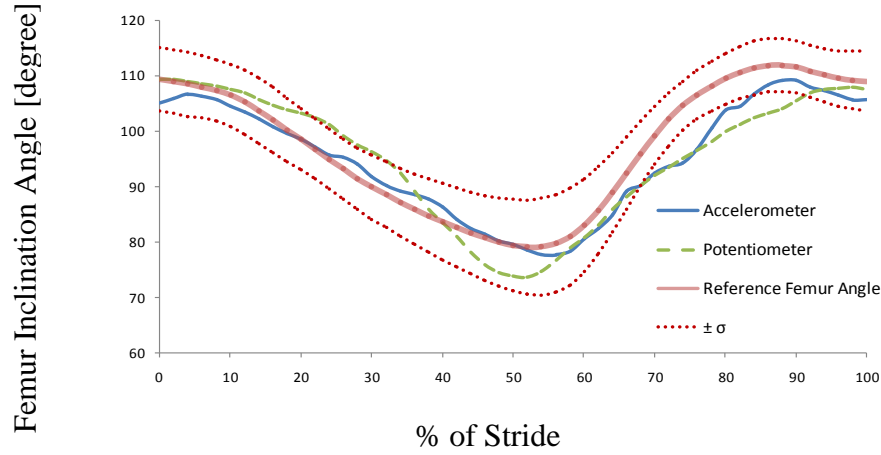
Figure 5-14: Comparison between accelerometer and potentiometer readings for femur inclination angle vs. gathered data by Winter [31]. As walking patterns differ between individuals, there are variations in data.

5.3.1.5 Gyroscope together with Accelerometer

In the last methodology, a combination of biaxial accelerometers and gyroscopes was utilized. This method was addressed first time by Aminian et al [32]. One accelerometer and one gyroscope were used for each link, so the total number of sensors used was four. Joint angles were obtained without integration and drift problems. This technique provides flexion/extension angles by estimating acceleration of the joint center of rotation. As shown in Figure 5-15, two sets of combinations of an accelerometer and a gyroscope must be placed at points P_1 and P_2 on the adjacent segments of the joint center of rotation. Then, the kinematic data of the joint center of rotation can be found by mathematically shifting the location of sensor to the joint center (point C).

The real and virtual sensor data have the following relation:

$$R_\beta \cdot \begin{bmatrix} S_{x'} \\ S_{y'} \end{bmatrix} = R_\alpha \cdot \begin{bmatrix} S_x \\ S_y \end{bmatrix} + \frac{d^2 \mathbf{r}}{dt^2} \tag{5.9}$$

66

$$\frac{d^2\mathbf{r}}{dt^2} = \frac{d}{dt}(\dot{\mathbf{r}}.\mathbf{u_r}) = -r\dot{\theta}^2.\mathbf{u_r} + r\ddot{\theta}.\mathbf{u_r} \qquad (5.10)$$

where j is the accelerometer number index, and $\dot{\theta}^2$ and $\ddot{\theta}$ are the first and second derivatives of angle of r with respect to a fixed inertial frame. To align both real and virtual coordinate systems to the direction the of PC line, the rotation matrix R_α must be applied to the real accelerometer readings, $[S_x \ S_y]^T$, and R_β must be applied to the virtual accelerometer readings, $[S_{x'} \ S_{y'}]^T$.

If the virtual sensor of each segment is shifted to the same point, center of rotation, both of them must read the same acceleration. Therefore, the joint angle (φ) can be obtained by calculating the rotation matrix (R_φ) between two virtual accelerometers. Each virtual sensor must align with its corresponding segment orientation. As with as former method, here it is assumed that the joint center of rotation is a fixed position point. In other words,

$$\begin{bmatrix} S_{x_1'} \\ S_{y_1'} \end{bmatrix} = R_\phi . \begin{bmatrix} S_{x_2'} \\ S_{y_2'} \end{bmatrix} \qquad (5.11)$$

There is no need to concern on the influence of the trunk acceleration on the accelerometers, since it applies the same effect on both sensors. In this technique, the anthropometry parameters must be recalculated for every individual prior to each measurement and fed to the model to estimate the virtual sensors data. Therefore, this model is personalized for each subject.
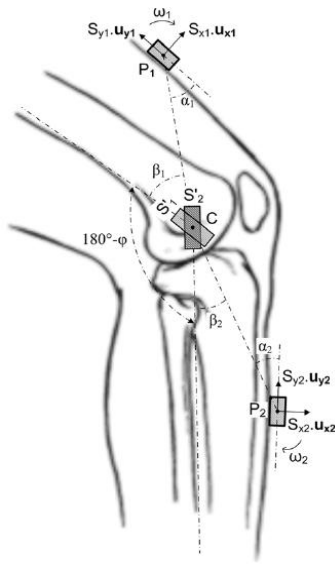
Figure 5-15: Position of sensors on femur and tibia, and their related virtual sensors on the center of rotation of knee joint [32]

It is essential to notify that for the entire aforementioned techniques skin motion artifact is a common source of error which leads to discrepancies in reading data. This flaw can be minimized by using suitable elastic bands to fix the utilized sensors to the leg.

5.4 Discussion

The intention of the sensing system is to extract signal from the user's healthy leg and send the captured data to the APK controller as the input signal. Two methods were tried: EMG and lower limb inclination angles. The assembling problem of EMG, high sensitivity to noise, and variability to temperature forced the author to look for other methods that utilize inclination angle measurement to provide input data for the controller. Different techniques were discussed to measure the thigh and shank angular positions. All those techniques are much simpler to use than the cumbersome EMG method. The EMG signal has larger variance for different people and even for day-to-day walking of one specific person than inclination angle of lower limb segments. Conversely, the method that uses potentiometer together with accelerometer shows a moderate accurate reading of data that is less prone to noise. A more accurate measurement can be attained by utilizing gyro together with accelerometer.

68

Chapter 6

COMMUNICATION

6.1 Introduction

The communication between sensory part and actuator is accomplished via wirless communication by employing two boards, the transmitter and reciever (Figure 6-1). The boards communicate through bluetooth method. The detailed design of these boards is described in the following sections.

6.2 Sensor Board (Transmitter):

The transmitter board is responsible for collecting data from the accelerometer and rotary potentiometer, converting it from analog to digital, and sending it through Bluetooth communication to the receiver board for processing. The parts of the transmitter board are listed in Table 6-1. The schematic of the transmitter board is shown in Figure 6-2.
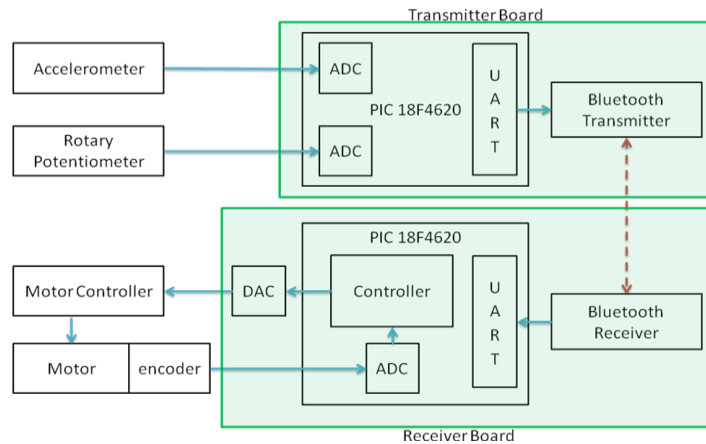
Figure 6-1: Communication diagram

Table 6-1: The components of the transmitter board

Part	Part Number	Quantity
5V Voltage Regulator	LM7805C	1
Texas Instruments Op-amp	OP07DP	2
Bourns Multi-turn Trimmer Potentiometer (10 kΩ, ¾", ± 10%)	3006P-1-103LF	4
Voltage Inverter	ICL7660CPA	1
Xicon Radial Electrolytic Capacitor (10 uF, ± 20%)	140-XRL100V10-RC	2
Resistor (1 kΩ, ¼ w, ± 10%)	-	3
LED (Green)	-	1
EZURiO BISM2 Bluetooth Module	239-TRBLU23-00200	1
Tek Gear BISM2 Expansion Board	-	1
Microchip PICmicro Flash Microcontroller	PIC18F4620	1
Accelerometer	DE-ACCM5G	1
Potentiometer (20 kΩ ± 10%)	-	1
7.2V Rechargeable Battery	-	1

The transmitter board is powered up by a 7.2V battery. A voltage inverter (ICL7660CPA) is used on the transmitter board to invert the power supply voltage and create a -7.2V rail. The +7.2V and -7.2V rails supply power to the two op-amps (OP07DP).The transmitter

board uses a voltage regulator (LM7805C) to create a 5V rail from the 7.2V battery. The 5V rail is used to power the Bluetooth module (EZURiO BISM2), an accelerometer (DE-ACCM5G), and a microcontroller (PIC18F4620).

The PIC microcontroller samples the analog voltages from the accelerometer and rotary potentiometer (angular sensors), converts them into digital values using an analog to digital converter (ADC) and sends them to the Bluetooth module via the UART protocol.

The X-axis and Y-axis output voltages from the accelerometer (DE-ACCM5G) are passed through two op-amps before being relayed to the PIC. The gain of both op-amps is set to 1.5 by employing two multi-turn potentiometers (3006P-1-103LF). To improve the resolution of the analog-to-digital conversion of the accelerometer outputs, a second pair of potentiometers is used to create voltage dividers. These variable resistors divide the +5V rail voltage to 3V and 4.5V which are the reference voltages used by the ADC in the PIC microcontroller.

Another voltage divider, composed of two 1 kΩ resistors, is used to half the voltage transmitted by the PIC to the Bluetooth module to ensure it is within the module's reading range. The supplied values are then transmitted to the receiver board via the Bluetooth module. Lastly, a green LED and a 1kΩ resistor are connected to the microcontroller and used to indicate if the board is powered up.

.
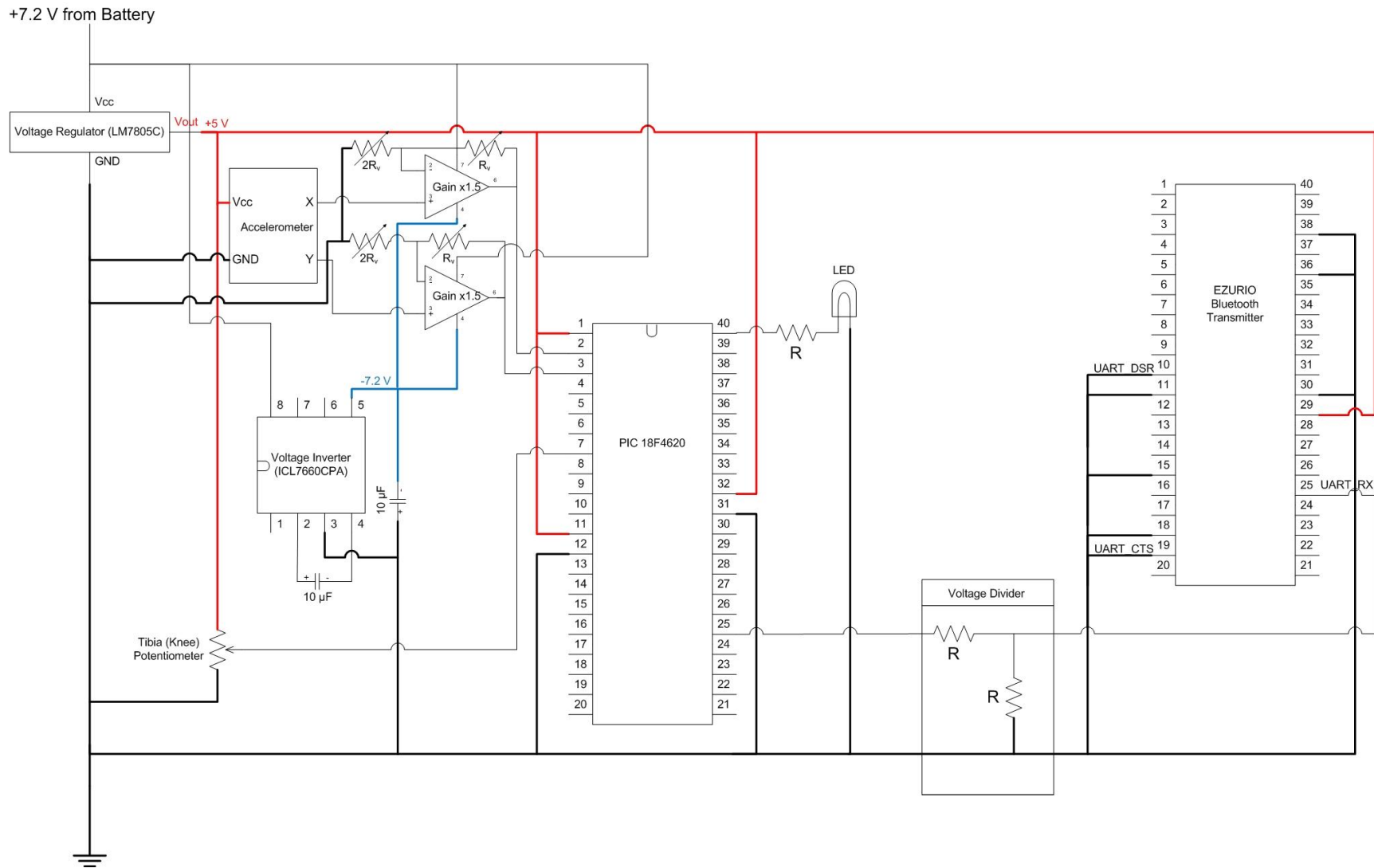
Figure 6-2: The schematic of the transmitter board

6.3 Main Board (Receiver)

The main board (receiver) is responsible for: connecting to the transmitter, receiving the sensor data, and converting it into the femur and tibia angular positions in order to provide the APK controller inputs. Moreover, the receiver board contains the controller block. The FIS output drives the motor on the prosthetic leg. The parts of the receiver transmitter board are listed in Table 6-2 and a schematic of the receiver board is available in Figure 6-3.

The receiver is powered by an external power supply which creates a 10V rail. A voltage regulator is used to create a 5V rail which powers the digital-to-analog converter (DAC - MC 4921-0648), microprocessor (PIC18F4620) and, Bluetooth modules (239-TRBLU23-00200). One Bluetooth module is mandatory and is paired with the transmitter board. It receives sensor data and sends it to the microcontroller via the UART protocol. This module's UART receive pin is permanently asserted and it acts as a receiver while the circuit is powered. A second module is present on the board to allow the sensor data to be relayed to the system monitor program. It receives the same data that is sent to the microcontroller and is used for demonstration and troubleshooting purposes.

The DAC receives a 12-bit digital value from the microcontroller (FIS output), which indicates at what speed and in which direction the motor should be driven. It converts this digital value into its analog equivalent which lies between 0V and 5V.

Driving the motor controller requires a voltage between 10 and -10V. However, the DAC, as it has been configured, generates voltages only between 0V and 5V. Therefore, two steps are taken to map the DAC output to the required voltage range. First, the DAC voltage is inverted by an op-amp (OP07DP) inverter. Both the inverted and non-inverted DAC voltages are supplied on two separate channels to the dual, 4-channel, multiplexer (MUX - CD4052BCN). The MUX's select bit is driven by the microcontroller thereby allowing it to select the direction of the motor's motion. The microcontroller's output is passed to a transistor (2N4400) which is used to drive MUX's select bit. Second, another

op-amp (OP07DP) acts as a voltage amplifier and uses two 1 kΩ resistors to double its input voltage. This op-amp receives the output of the MUX and doubles it so that it falls between +10V and -10V. The output of this op-amp is used to drive the motor controller. To power both the voltage amplifier and inverter op-amps, a voltage inverter (ICL7660CPA) is used to create a -10V rail from the 10V generated by the power supply. The 10V and -10V rails power the op-amps. The board also contains a second voltage inverter to generate -5V from the 5V rail. These are used to power a third op-amp which amplifies the output signal from the Bluetooth module before it is sent to the microcontroller.

Table 6-2: The components of the receiver board

Part	Part Number	Quantity
5V Voltage Regulator	LM7805C	1
Texas Instruments Op-amp	OP07DP	3
Bourns Multi-turn Trimmer Potentiometer (10 kΩ, ¾", ± 10%)	3006P-1-103LF	4
Voltage Inverter	ICL7660CPA	2
Xicon Radial Electrolytic Capacitor (10 uF, ± 20%)	140-XRL100V10-RC	2
Resistor (1 kΩ, ¼ w, ± 5%)	-	5
Microchip Digital to Analog Converter	MC 4921-0648	1
Dual 4-Channel Analog Multiplexer	CD4052BCN	1
50V Diode	-	1
NPN Epitaxial Silicon Transistor	2N4400	1
EZURiO BISM2 Bluetooth Module	239-TRBLU23-00200	1 (+1 optional)
Tek Gear BISM2 Expansion Board	-	1 (+1 optional)
Microchip PICmicro Flash Microcontroller	PIC18F4620	1
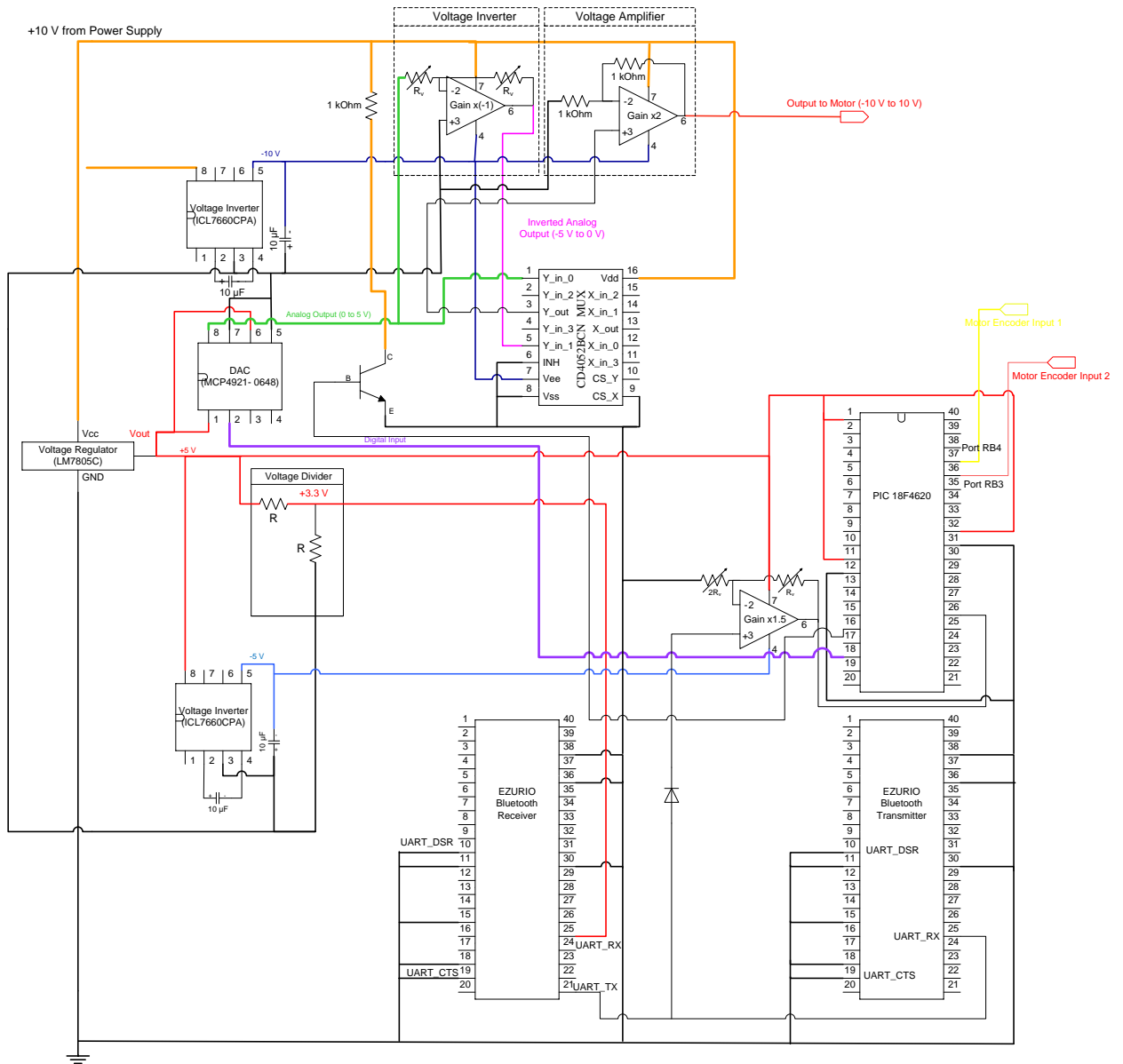
Figure 6-3: The schematic of the receiver board

Chapter 7
CONTROL

7.1 Introduction

This chapter addresses a new method of human gait phase recognition necessary for cadence control. The problem of walking cadence control has been identified as residing in lower limb prostheses or rehabilitation. Bringing back a sense of confidence and freedom to the patients who are trans-femoral amputees or have one leg paralyzed depends greatly on the functionality of the implemented control system. In the sensing system chapter, the healthy thigh and shank inclination angles are preferred rather than EMG signal to provide input signals to the controller. The motivation of this chapter is to design a controller for the APK to send a correct value of torque associated with input signals to the APK actuator.

The classical control methods are based on an available mathematical dynamic model of the process and, in most cases, on a linearized model. In the case of the walking cycle, a controller based on the locomotion dynamic model (even a linearized model) will

probably be very complex [33]. Therefore, traditional controllers alone, such as Proportional–Integral–Derivative (PID), may not be suitable for real-time control. Most of these methods, however, are influenced by the uncertainty of inputs and limited by the sampling frequency of the utilized sensors or the walking cadence. The literature reports on very few documented controlled above knee prostheses, more inevitably exist. Even in prior work that utilized an adaptive control scheme to compensate for the effect of the speed of walking on knee parameters, uncertainty of inputs or gathered information was not considered [34], [35][36]. Sup et al [16] suggested a controller based on the error and its first derivative between the angle of the prosthetic knee and its equilibrium point for four different modes of the gait cycle. However, experimental results showed that enormous adjustment for gains of the four recommended PD controllers were needed since variance of input data was not considered when designing the gains of controllers.

Unlike prior work, the approach proposed herein (Figure 7-1) to generate knee torques utilizes a knowledge-based system that considers the uncertainty of inputs and is not dependent of walking cadence dynamic model. Only one PID, as a secondary controller, accompanies the aforementioned system to correct the prosthetic position discrepancies from the desired values due to disturbances like uneven terrain.
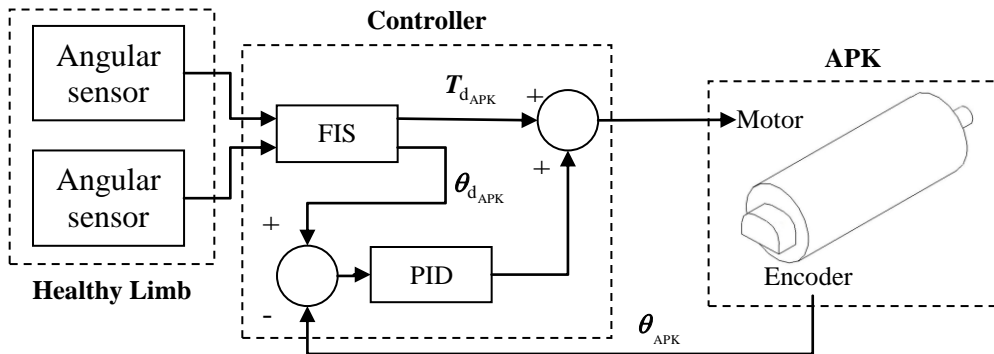
Figure 7-1: Control diagram of APK

Following is a description of the methodology utilized to achieve the desired knowledge-based system, such as the different types of Fuzzy Inference Systems (FISs) were tried and analysis comparisons are provided. Before going to details of designed fuzzy system a brief introduction to fuzzy inference systems is presented.

7.2 Preliminaries [2]

This section covers the principles of fuzzy set theory, operations and relations/compositions that provide the background required to understand Fuzzy Inference Systems[3].

Fuzzy logic was first proposed by Zadeh [38] in 1965. He introduced the concept of "linguistic variables" analogues to a variable defined as a fuzzy set. Zadeh introduced fuzzy set theory as an extension of traditional crisp set theory.

One classical set, A, is defined on a universe discourse, X, and can be described in terms of a zero-one membership function, $\mu_A(x)$.

$$\mu_A(x) = \begin{cases} 1 & if \ x \in A \\ 0 & if \ x \in A \end{cases} \tag{7.1}$$

The defined membership function above is equivalent to the set A.

Similarly, a fuzzy set, F, is defined on a universe discourse, U, and can be characterized as a membership function $\mu_F(x)$ whose membership value can be any single number in the interval [0,1].

In that sense, a fuzzy set is a generalization of a classical set by allowing the membership function to have a single value between zero and one instead of having a crisp value of

---

[2] Most of the material in this section is paraphrased from Mendel's tutorial on fuzzy logic systems [37]

[3] The reader can skip this section if he/she has already knows the fundamental of FIS.

either 0 or 1. Sometimes a fuzzy set F can be represented as a set of pairs of x and its membership function

$$F = \{(x, \mu_A(x)) | x \in U\} \tag{7.2}$$

Therefore, F presents the membership function while $\mu_F(x)$ presents the membership value or the grade of membership function. Fuzzy sets also can be expressed by the following notation

$$F = \begin{cases} \int_U \mu_F(x)/x & \text{if } U \text{ is continuous} \\ \sum_U \mu_F(x)/x & \text{if } U \text{ is discrete} \end{cases} \tag{7.3}$$

The integral sign, $\int_U$, and the summation sign, $\sum_U$, denote the collection of all points, x, and $\mu_F(x)$ denote their associated membership functions.

In a rule-based FIS, membership functions are embedded in the antecedents or consequents of rules. The most common shapes for $\mu_F(x)$ are triangular, trapezoidal, and Gaussian.

Operation fuzzy sets are similar to their crisp sets counterparts. Operation such as complement, union, and intersection, however, these operations are defined in terms of their membership functions. Assuming a fuzzy set F, the complement of F is a fuzzy set in U that is defined as

$$\mu_{\bar{F}}(x) = 1 - \mu_F(x) \tag{7.4}$$

The union of fuzzy sets A and B, is defined as

$$\mu_{AUB}(x) = \max(\mu_A(x), \mu_B(x)) \tag{7.5}$$

The intersection of fuzzy sets A and B, denoted by $A \cap B$ is defined as

$$\mu_{A \cap B}(x) = \min(\mu_A(x), \mu_B(x)) \tag{7.6}$$

The main result of above definition for complement, union, and intersection operation on fuzzy sets is crossing the law of Excluded Middle and Contradiction. In other word, as a result of aforementioned definition $A \cup \bar{A} \neq U$ and $A \cap \bar{A} \neq \varnothing$.

The min and max operators are not the only definitions that can be chosen to model fuzzy union and intersection. The fuzzy union and intersection are generally referred to as s-norm operation, denoted by $\oplus$, and t-norm operation, denoted by $\otimes$, respectively.

Any pairs of operations that satisfy monotonicity, commutativity, associativity, distributivity, and generalization of DeMorgan's law can be defined as the pairs of t-norm and s-norm [39]. In this work, the minimum or algebraic product t-norm is defined for fuzzy intersection, and maximum s-norm for fuzzy union.

7.2.1 Fuzzy Rules

A fuzzy rule-base is a collection of IF-THEN rule statements that formulate and describe the behaviour of a given system. An extended version of the fuzzy rules with multiple antecedents and single consequent is depicted here:

$\mathbf{R}_l :$ IF $\quad x_1$ is F_1^l AND/OR $\quad x_2$ is $F_2^l \cdots$ AND/OR $\quad x_p$ is F_p^l THEN $\quad y$ is G^l

where l is the rule index and $l=1,2,\ldots,M$; F_j^l are fuzzy input sets in universe discourse U and ; G^l is fuzzy output set in universe discourse V.

The IF-part of the rule is called the antecedent or premise, while the THEN-part of the rule is called the consequent or conclusion. The connective operator AND or OR are used to form the multiple antecedent fuzzy rules, which are equivalent to fuzzy intersection and fuzzy union respectively. It must be pointed out that only one type of these connectives (AND or OR) exist between two premise. The above conditional statements comprise fuzzy logic.

7.2.2 Fuzzy Inference Engine

Fuzzy logic principles are used in fuzzy inference engine to combine the rules into a mapping from fuzzy input sets to fuzzy output sets. As in the extension of crisp set theory to fuzzy set theory, the extension of crisp logic to fuzzy logic is made by replacing the two-valued membership functions of crisp logic, (0,1), with continuous-valued membership functions, [0,1].

One membership function is allocated to each fuzzy IF-THEN statement such as IF A THEN B. This membership function measures the degree of truth of the implication relation between x and y, and can be expressed as $\mu_{A\to B}(x,y)$ whose value is in [0,1] interval.

Minimum and product implications (t-norm) are used specifically in this work to describe this membership function, i.e. $\mu_{A\to B}(x,y)=\mu_A(x)\otimes\mu_B(y)$

Therefore, the membership function of the earlier multi-antecedent rule can be stated as

$$\mu_{R(l)}(\mathbf{x},y)=\mu_{A\to B}(\mathbf{x},y)=\left(\mu_{F_1^l}(x_1)*\mu_{F_2^l}(x_2)*\cdots*\mu_{F_p^l}(x_2)\right)\otimes\mu_{G^l}(y) \qquad (7.7)$$

where $*$ is $\oplus$ (s-norm) or $\otimes$ (s-norm) depends on the construction of the stated rule; and $F_1^l\times F_2^l\times\cdots\times F_p^l \ \square\ A$ and $G^l \ \square\ B$ then $R_{(l)}:A\to B$. It is worth to note that part "x is" is excluded from the above evaluation. This part is taken into account as fuzzification, which will be discussed in the following.

Interpreting an IF-THEN rule involves multiple steps: first evaluating the antecedent and second applying that result to the consequent. Evaluating the antecedent itself is divided into two sections: converting the crisp input numerical data into fuzzy sets (fuzzification) and then utilizing the fuzzy operators to evaluate the antecedent in terms of degree of membership to all input fuzzy sets.

7.2.3 Fuzzification

In any FIS, one needs to deal with fuzzy sets to be able to implement different fuzzy techniques. Therefore, mapping the crisp numerical data, $\mathbf{x} = \{x_1, \ldots, x_n\} \in U$, into fuzzy sets, $A_i^* \in U$ is the first step. This step is called Fuzzification and can be achieved by means of a fuzzifier. There are two major types of fuzzifiers (1) singleton, and (2) non-singleton.

In singleton fuzzifier with support x', the membership function that associates with A^* can be considered as crisp membership function, in other words

$$\mu_{A^*}(x) = \begin{cases} 1 & for \quad x = x' \\ 0 & otherwise \end{cases} \tag{7.8}$$

where x' is basically the crisp input.

In a non-singleton fuzzifier with support x', the membership function that associates with A^* is fuzzy membership function.

$$\mu_{A^*}(x) = \begin{cases} 1 & for \quad x = x' \\ 0 \leq \mu < 1 & otherwise \end{cases} \tag{7.9}$$

Thus, for x', $\mu_{A^*}(x') = 1$, and $\mu_{A^*}(x)$ decreases from unity as x moves away from x'.

However, the singleton fuzzifier by itself may not always be adequate, especially when input data is contaminated by noise.

7.2.4 Fuzzy Reasoning

At this time, to complete the evaluation of the antecedent of the fuzzy rule, $\mu_{A^*}(x)$ must be put into action. Hence,

$$\mu_{B'}(y) = \mu_{A_{\mathbf{x}} \square R^{(l)}}(y) = \sup_{\mathbf{x} \in A_{\mathbf{x}}} \left[\mu_{A_{x_1}}(\mathbf{x}) \otimes \mu_{A \to B}(\mathbf{x}, y) \right] \tag{7.10}$$

82

Equation (7.10) is the correlation between crisp inputs and output of one excited rule. In other words, $\mu_{B^l}(y)$ is the output of fuzzy inference engine; however, the grade of membership of inputs, $\mu_{A^*}(x)$, were defined in the fuzzifier, Substituting (7.7) in (7.10) gives

$$\mu_{B^l}(y) = \mu_{G^l}(y) \otimes \left\{ \left[\sup_{\mathbf{x} \in U} \mu_{A_{x_1}}(x_1) \otimes \mu_{F_1^l}(x_1) \right] * \right.$$
$$\left. \cdots \left[\sup_{\mathbf{x} \in U} \mu_{A_{x_p}}(x_p) * \mu_{F_p^l}(x_p) \right] \right\} \tag{7.11}$$

The final fuzzy set can be obtained by combining all the B^l from all the rules in the rule-base. One method to find the final fuzzy set is using fuzzy union or s-norm for all the attained B^l. However, most of the time, the final fuzzy set is determined during defuzzification process.

7.2.5 Defuzzification

At the end of any fuzzy mechanism, we need to convert the fuzzy set that is the output of inference engine to a crisp point. The inverse fuzzy transformation process, which is used to map the fuzzy output variable to that of a crisp one, is called defuzzification. There are many defuzzifiers in the literature, however, "there are no scientific bases for any of them"[37]. The most important criteria to select any of offered defuzzifier in the literature is the expense of the computation. Two most popular defuzzifiers are depicted here:

(i) Centroid defuzzifier:

$$\overline{y} = \frac{\int_c y \mu_B(y) dy}{\int_c \mu_B(y) dy} \tag{7.12}$$

Where c indicates the support of $\mu_B(y)$

(ii) Height defuzzifier:

$$\bar{y} = \frac{\sum\limits_{l=1}^{M} \bar{y}^l \, \mu_{B^l}(\bar{y}^l)}{\sum\limits_{l=1}^{M} \mu_{B^l}(\bar{y}^l)} \tag{7.13}$$

where $\bar{y}^l$ is the center of gravity of the fuzzy set B^l.

In the process of fuzzy inference system, the following figure demonstrates the structure of a FIS based on the aforementioned parts.
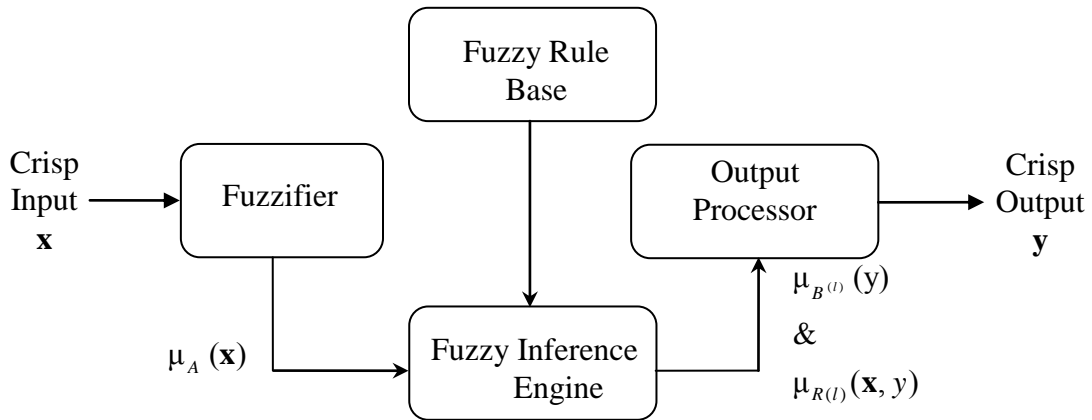
Figure 7-2: Basic configuration of the FIS [37]

7.2.6 Mamdani FIS vs. TSK FIS

According to Figure 7-2, fuzzifier maps the crisp vector of inputs to the input fuzzy sets, then fuzzy inference engine combines the rules from fuzzy rule-base and map the result of fuzzifier to the output fuzzy set.

There are two main types of FIS: Mamdani [40] and Takagi-Sugeno-Kang (TSK) [41]. The main difference of these two systems is in the output process block. The aforementioned system that utilized defuzzifier to extract crisp output from the output fuzzy sets of the inference engine is called Mamdani.

TSK FIS not only differs in the output process block of the FIS, but it also has different rule consequence structures. Instead of having output fuzzy sets and as a result the degree

of membership, $\mu_{G^l}(y)$, TSK fuzzy rules have a consequent crisp function, g, such as polynomial. The rules of the TSK FIS are expressed as

$$\mathbf{R}_l : \text{IF} \quad x_1 \text{ is } F_1^l \text{ AND/OR } x_2 \text{ is } F_2^l \cdots \text{AND/OR} \quad x_p \text{ is } F_p^l$$
$$\text{THEN} \quad y^l(\mathbf{x}) = g(x_1, x_2, \ldots, x_p)$$

Where l is the index indicating the rule number, $j=1,\ldots,p$ is the index for inputs. The output processor aggregates the outputs of the rules and computes the final output as

$$y_{\text{TSK}}(\mathbf{x}) = \frac{\sum_{l=1}^{M} f^l(\mathbf{x}) y^l(\mathbf{x})}{\sum_{l=1}^{M} f^l(\mathbf{x})} \tag{7.14}$$

where $f^l(\mathbf{x})$ is the rule firing level given by

$$f^l(\mathbf{x}) = \left(\mu_{F_1^l}(x_1) * \mu_{F_2^l}(x_2) * \cdots * \mu_{F_2^l}(x_2) \right) \tag{7.15}$$

The fuzzy inference diagrams in Figure 7-3 and Figure 7-4 display all described parts of the Mamdani and TSK fuzzy inference process, respectively. Information flows through the FIS diagram as shown below.
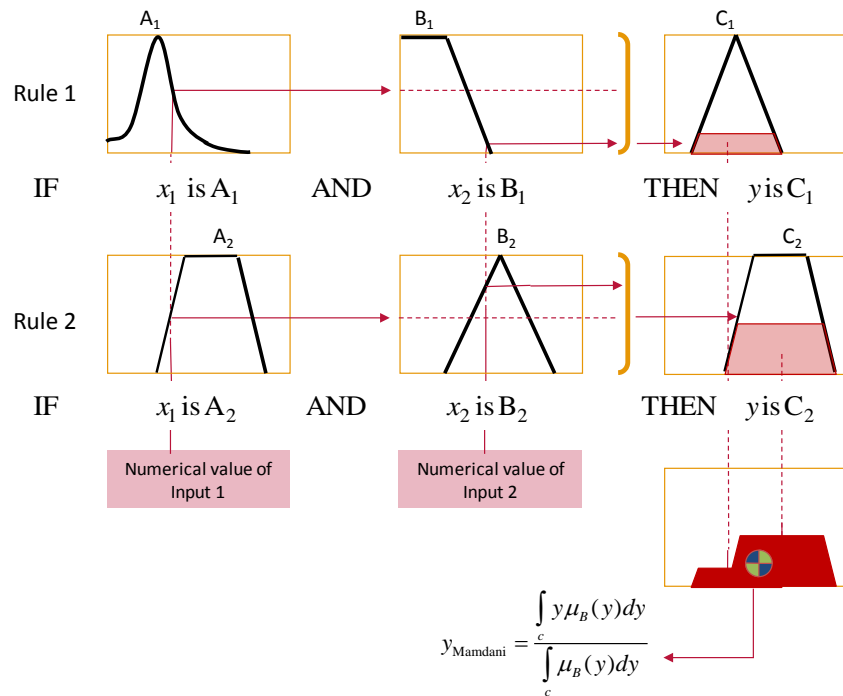
Figure 7-3: Mamdani FIS diagram, example of two-input one-output FIS, two membership functions associate with each input in this example, minimum t-norm is selected for compositions and implication, selected defuzzifier is centroid defuzzifier.
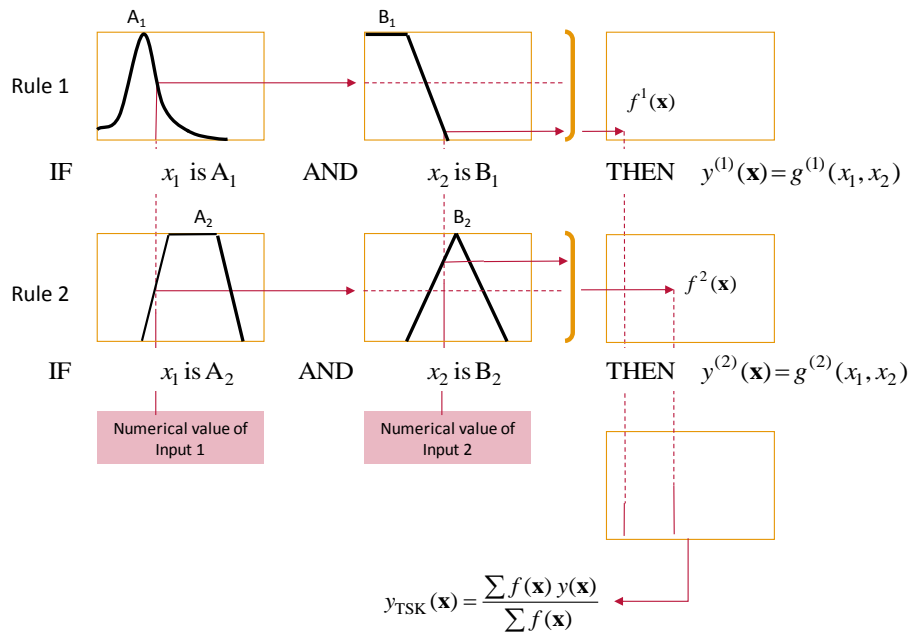
Figure 7-4: TSK FIS diagram, example of two-input one-output FIS, two membership functions associate with each input in this example, minimum t-norm is selected for compositions.

7.3 Designed Mamdani FIS

In the last section, we learned about different types of fuzzy inference systems. The first tried fuzzy methodology is a singleton type-1 Mamdani FIS. Mamdani type[4] is the most prevalent observed type of Fuzzy Inference System, and it was among the pioneers of fuzzy control systems.

The inputs of the Mamdani fuzzy inference systems are the inclination angles of the tibia and femur. Outputs are the torque and desired angle of the prosthesis. The thigh/leg angle (Figure 7-5), body-mass-normalized knee torque (Figure 7-6), and knee angle (Figure 7-7) specifications during one period of the normal gait cycle are derived from the work of Winter [31]. It is assumed that for one stride, there will be 50% phase shift between the prosthesis and the healthy leg just as for a normal person. Results are shown in Figure 7-8 and Figure 7-9.The main components of the Mamdani FIS that must be defined are i) rules ii) fuzzifier iii) inference engine iv) defuzzifier.

The repetitive inputs and outputs of training data [31], are partitioned based on seven phases of the human walking cycle described in background section. The vertical dash lines used on Figure 7-5, Figure 7-6, and Figure 7-7 to cluster the repetitive input data are chosen based on the aforementioned sub-phases of the healthy leg in section 1.2.3. Comparing to the healthy leg (Figure 7-6 and Figure 7-7), the contra-lateral leg has phase shift for 50% (Figure 7-8 and Figure 7-9). However, the partitioning of training data and generating output membership functions are based on the sub-phases of the healthy leg (Figure 7-6 and Figure 7-7).

---

[4] Preliminaries section provides more details about the principle of Mamdani's fuzzy inference method.
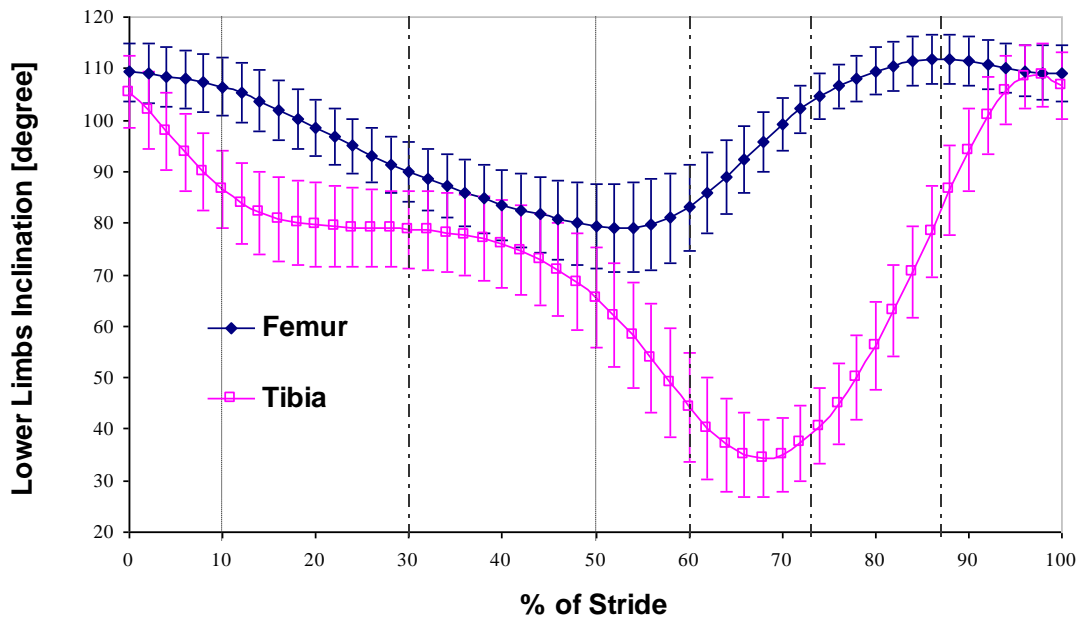
Figure 7-5: FIS inputs-healthy femur and tibia angular positions in respect to ground (normal cadence)

If it is assumed that the distribution of data in each cluster is normal and independent, the input and output membership functions are Gaussian. Please refer to Figure 7-10 to see a Gaussian distribution. To define the input and output parameters of the FIS, average and standard deviation of the data in each cluster is calculated and called mean and standard deviation of the sample mean for the cluster of interest.

88
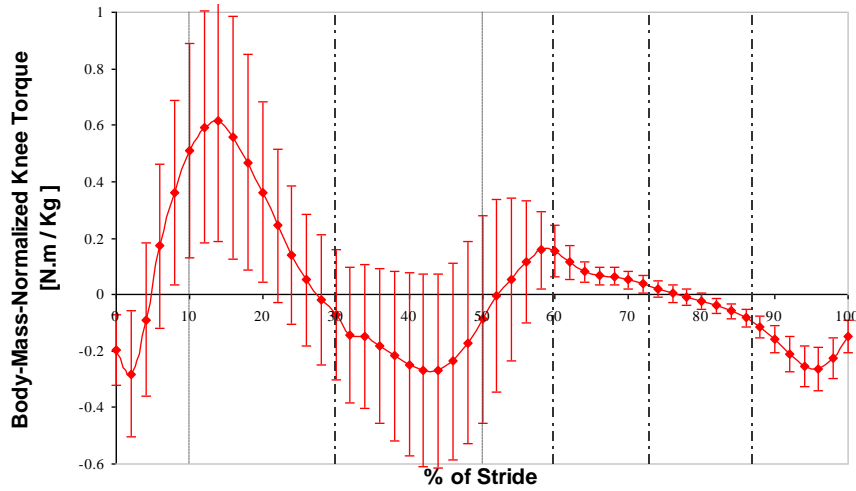
Figure 7-6: Knee torque of the healthy leg (normal cadence)
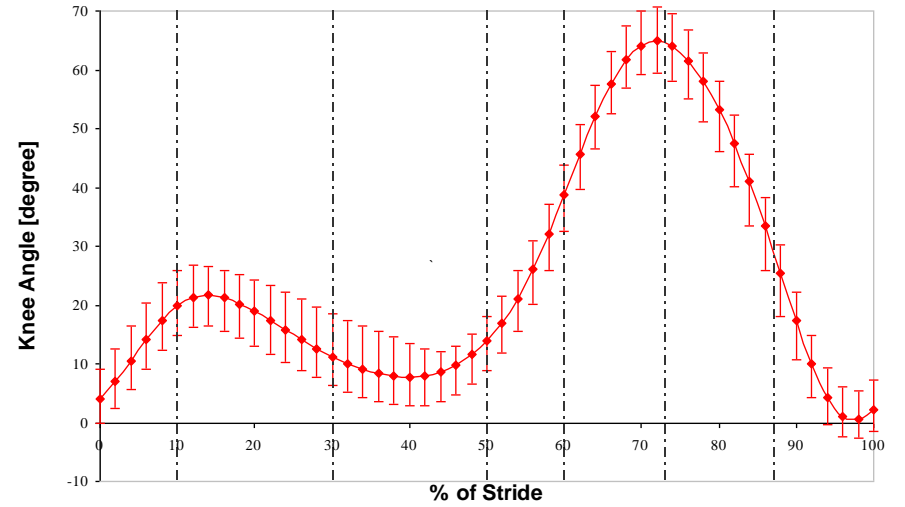
Figure 7-7: Knee angle of the healthy leg (normal cadence)
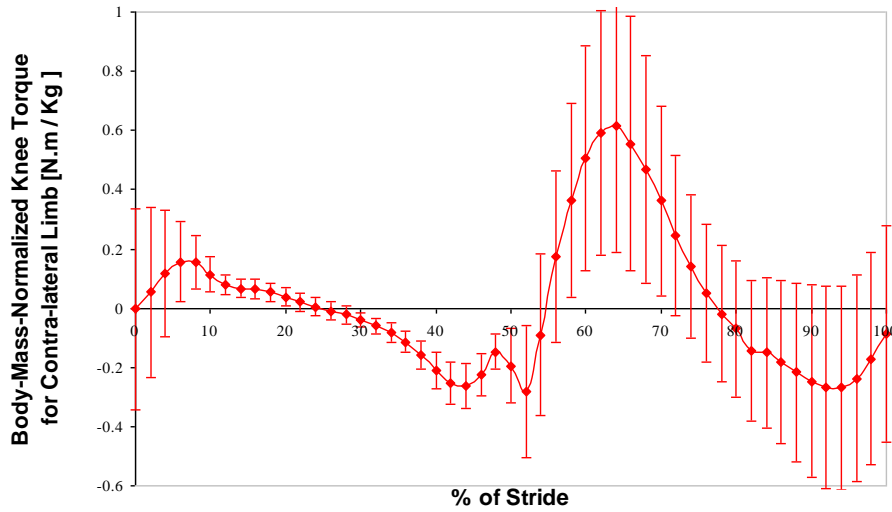
Figure 7-8: FIS first output: prosthetic knee torque; Figure 7-6 is shifted for 50% of stride.
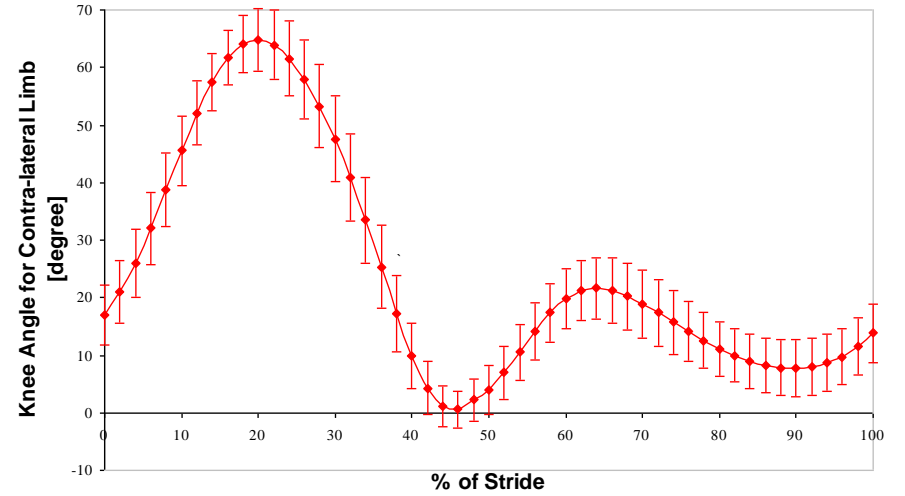
Figure 7-9: FIS second output: prosthetic knee angle Figure 7-7 shifted for 50% of stride.

89

7.3.1 Obtaining Mean and Standard Deviation of the Sample Mean for the Cluster of Interest

Let $c_1, c_2, \ldots, c_n$ be constant and let $X_1, X_2, \ldots, X_n$ be independent random variables with means $E(X_i) = \bar{X}_i, i = 1, 2, \cdots, n$ and variances $V(X_i) = \sigma_i^2, i = 1, 2, \ldots, n$. Then, the mean and variance of the linear combination $Y = c_1 X_1 + c_2 X_2 + \ldots + c_n X_n$ are

$$E(Y) = c_1 \bar{X}_1 + c_2 \bar{X}_2 + \ldots + c_n \bar{X}_n \qquad (7.16)$$

$$V(Y) = c_1^2 \sigma_1^2 + c_2^2 \sigma_2^2 + \ldots + c_n^2 \sigma_n^2 \; [9]. \qquad (7.17)$$
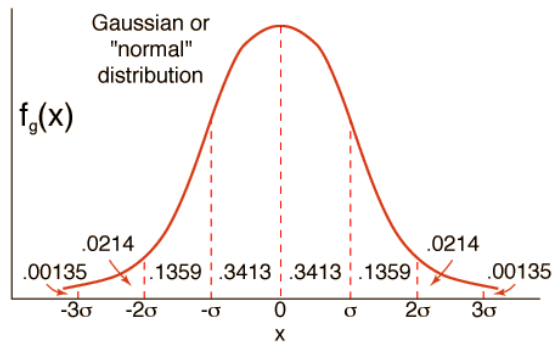
Figure 7-10: Gaussian distribution

Now consider our case. We want to calculate the mean and variance of the sample mean $\bar{X}$ of each cluster. Suppose that a sample of size 'N' is taken from the cluster of interest and each variable in this sample, say, $X_1, X_2, \ldots, X_n$, is independent with means $E(X_i) = \bar{X}_i, \; i = 1, 2, \cdots, n$ and variances $V(X_i) = \sigma_i^2, i = 1, 2, \ldots, n$. From the result on linear combination, we calculate that the sample mean of each cluster (with sample size of 'N')

$$\bar{X} = \frac{X_1, X_2, \ldots, X_n}{n} \qquad (7.18)$$

has a mean of $E(\bar{X})$ where,

$$E(\bar{X}) = m = \frac{\bar{X}_1 + \bar{X}_2 + \ldots + \bar{X}_N}{N} \tag{7.19}$$

and variance

$$V(\bar{X}) = \frac{\sigma_1^2 + \sigma_2^2 + \ldots + \sigma_N^2}{N^2} \tag{7.20}$$

Therefore the standard deviation of the sample mean is:

$$SD(\bar{X}) = \frac{1}{N}\sqrt{\sigma_1^2 + \sigma_2^2 + \ldots + \sigma_N^2} \tag{7.21}$$

The results are shown in Table 7-1. *Note:* The fuzzy sets for both inputs and output are called *Phase* #1: Loading Response (LR), *Phase* #2: Mid Stance (MST), *Phase* #3: Terminal Stance (TST), *Phase* #4: Pre Swing(PSW), *Phase* #5: Initial Swing (ISW), *Phase* #6: Mid Swing (MSW), and *Phase* #7: Terminal swing (TSW).

As explained, if it is assumed that each variable in each cluster, $X_1, X_2, \ldots, X_n$, is normally and independently distributed, we can conclude that the distribution of the sample mean is normal (Gaussian). The attained membership functions for inputs and outputs are depicted in Figure 7-11 and Figure 7-12. These illustrated fuzzy sets are based on the means and standard deviations obtained from Table 7-1.

NB Due to the shape of the Gaussian distribution (Figure 7-10), the solid lines show the variety of the mean sample up to $\pm 3\sigma$ (Figure 7-11 and Figure 7-12).

Table 7-1: Mean and standard deviation of the sample mean of each cluster for each input/output

	Femur Inclination Angle [degree]		*Tibia Inclination Angle* [degree]		*Knee Torque* [N.m/Kg]		*Knee Angle* [degree]	
	Sample mean	Sample standard deviation	Sample mean	Sample standard deviation	Sample mean	Sample standard deviation	Sample mean	Sample standard deviation
1 (LR)	108.057	2.316	95.918	3.035	0.079	0.115	12.138	1.861
2 (MST)	97.561	1.785	80.164	2.475	0.294	0.104	17.397	1.714
3 (TST)	83.405	2.236	73.965	2.717	-0.197	0.101	9.440	1.543
4 (PSW)	80.376	3.859	53.436	4.657	0.096	0.104	26.940	2.607
5 (ISW)	94.063	2.572	36.425	3.359	0.069	0.016	57.638	2.162
6 (MSW)	108.917	1.742	57.666	3.182	-0.027	0.011	51.251	2.662
7 (TSW)	110.284	1.875	101.603	2.709	-0.196	0.024	8.681	1.957

7.3.2 Rules

The maximum number of the rules allowed for a FIS is equal to the product of the number of membership functions for each input. Therefore, for the case under study, given that there are two inputs – the angular position of the femur and the tibia –and for each input, seven fuzzy sets, the maximum allowed number of rules will be 49. However, since during a walking cycle, the thigh and leg must be in the same phase at all times, the rules of the Mamdani fuzzy system can be restricted to seven. The seven obtained fuzzy rules, which consist of a collection of IF-Then rules, are summarized in a relational matrix depicted in Figure 7-13. This matrix is also referred to as a fuzzy associative memory [42]. Membership functions which are associated with healthy femur and tibia inclination angles, and torque and desired angle of the prosthesis are depicted in Figure 7-11 and Figure 7-12. This matrix in Figure 7-13 is identical for both outputs: APK's torque and angle. Therefore, entries in the matrix are fuzzy sets for prosthesis' torque/angle which are function of two states: inclination angle of femur x_1 and tibia x_2. Blank entries have no consequent associated with inputs. One example of the obtained rules by this matrix is:

$R^{(4,4)}$:   IF x_1 is Ph.4   AND x_2 is Ph.4   THEN y_1 is Ph.1, y_2 is Ph.1;
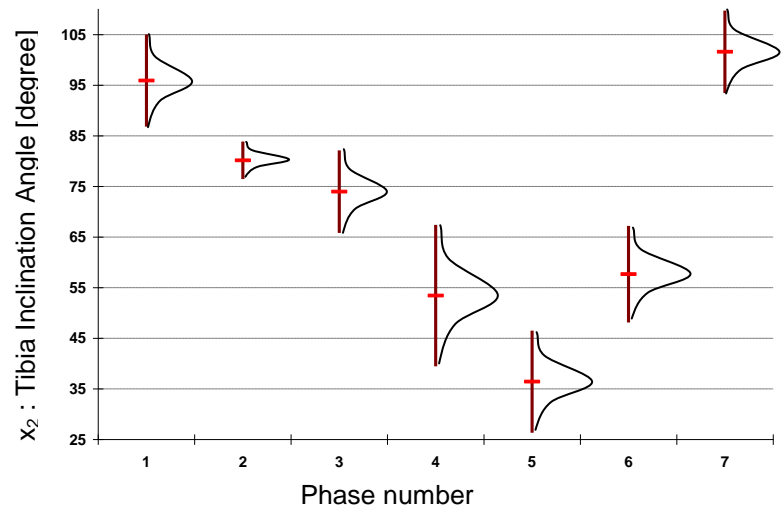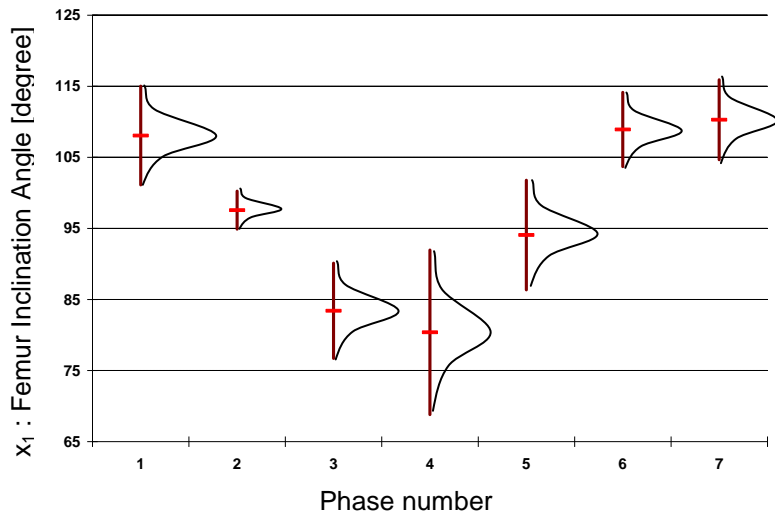
Figure 7-11: The inputs membership function plots
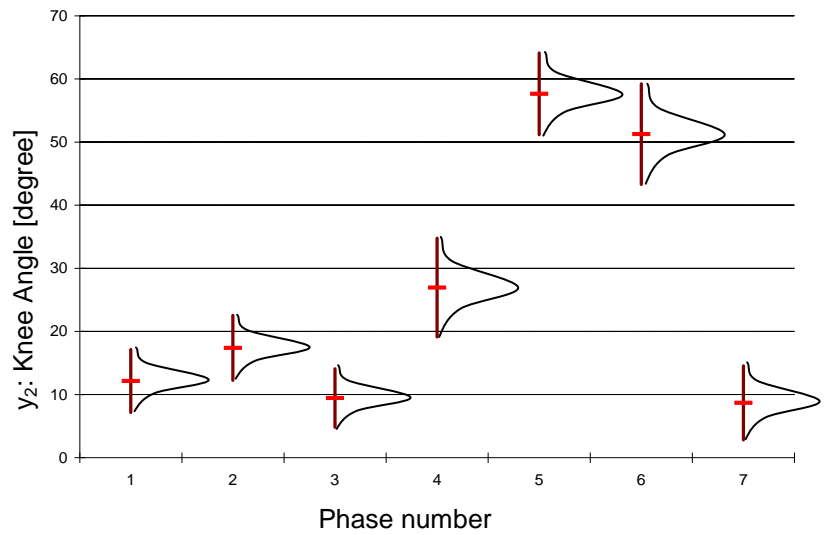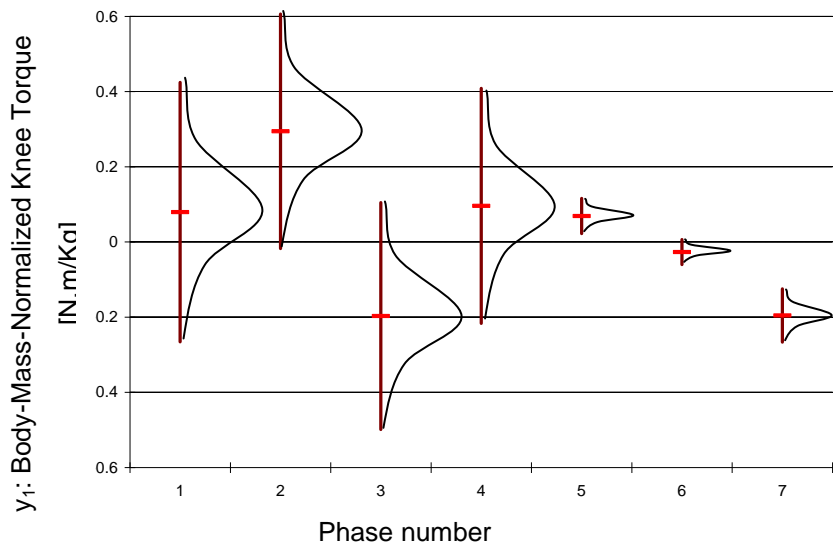
Figure 7-12: The outputs membership function plots

93

This matrix made based on the fact that when the reference leg (healthy one) starts the Initial Double Limb Support the contra-lateral leg must start the Second Double Limb Support (swing phase) and the length of these two periods are equal. In other words, the phase number of the contra-lateral leg is shifted by two or three with respect to the phase number of the reference leg. In one of the rules for the same configuration of inputs there may be possibility of two different configurations of outputs:

$R^{(2,2)}$:   IF x_1 is Ph.2   AND x_2 is Ph.2   THEN y_1 is Ph.5   OR y_1 is Ph.6,

y_2 is Ph.5   OR y_2 is Ph.6;

which we can decompose rule $R^{(2,2)}$ into two rules:

$R^{(2,2,1)}$:   IF x_1 is Ph.2   AND x_2 is Ph.2   THEN y_1 is Ph.5, y_2 is Ph.5

$R^{(2,2,2)}$:   IF x_1 is Ph.2   AND x_2 is Ph.2   THEN y_1 is Ph.6, y_2 is Ph.6

Figure 7-13: Rational matrix with the rules of the prosthetic leg controller

94

By decomposition of the second rule the total number of rules increases from seven to eight. As indicated in the defined rules, it has been assumed that antecedents are connected by ANDs, and consequently by t-norms.

7.3.3 Fuzzification and Fuzzy Reasoning

The fuzzy inference engine combines fuzzy rules to provide a mapping from fuzzy input sets to fuzzy output sets by means of fuzzy logic principles (sup-star composition). The Minimum operator was defined for the t-norm composition.

$$
\begin{aligned}
\mu_{R(l)}(\mathbf{x}, y) = \mu_{A \to B}(\mathbf{x}, y) &= \mu_{F_1^l}(x_1) \otimes \mu_{F_2^l}(x_2) \otimes \mu_{G^l}(y) \\
&= \min[\mu_{F_1^l}(x_1), \mu_{F_2^l}(x_2)] \otimes \mu_{G^l}(y)
\end{aligned}
\tag{7.22}
$$

Fuzzy singleton was applied for the fuzzifier section of the proposed FIS. The fuzzifier maps a crisp point $\mathbf{x} = \mathrm{col}(x_1, x_2) \in U = U_{x_1} \times U_{x_2}$ into a fuzzy set A^* in U, where A^* is a fuzzy singleton with support $\mathbf{x}'$ if $\mu_{A^*}(\mathbf{x}') = 1$ for $\mathbf{x} = \mathbf{x}'$ and $\mu_{A^*}(\mathbf{x}') = 0$ for all other $\mathbf{x} \in U$ with $\mathbf{x} \neq \mathbf{x}'$. The grade of the output membership function for the l-th rule would be simplified to:

$$
\mu_{B^l}(y) = \mu_{A_x \circ R(l)}(y) = \sup_{\mathbf{x} \in A_x} \left[\mu_{A_x}(\mathbf{x}) \otimes \mu_{A \to B}(\mathbf{x}, y) \right] = \mu_{A \to B}(\mathbf{x}', y)
\tag{7.23}
$$

In addition, by choosing minimum inference the above equation can be expressed as:

$$
\mu_{B^l}(y) = \mu_{A \to B}(\mathbf{x}, y) = \min \left[\min[\mu_{F_1^l}(x_1'), \mu_{F_2^l}(x_2')], \mu_{G^l}(y) \right]
\tag{7.24}
$$

where x_j' is the crisp input. By normalizing membership functions, $\mu_{G^l}(y) = 1$, we have:

$$
\mu_{B^l}(y) = \mu_{A \to B}(\mathbf{x}, y) = \min[\mu_{F_1^l}(x_1'), \mu_{F_2^l}(x_2')]
\tag{7.25}
$$

Where

$$\mu_{F_j^l}(x_j) = \exp\left\{-\frac{1}{2}\left[\frac{x_j - m_j^l}{\sigma_j^l}\right]^2\right\} \qquad (7.26)$$

where j is the input index and can be 1 or 2.

The final fuzzy set, B, is determined by all seven rules:

$$B = A_{\mathbf{x}} \circ \left[R^{(1)}, R^{(2)}, \ldots, R^{(7)}\right]$$

where the membership value of the final fuzzy set can be calculated based on (7.10).

7.3.4 Defuzzification

In this study, rules were combined as a part of defuzzification. Height defuzzifier was selected for the designed Mamdani FIS in order to generate a crisp output from the output fuzzy sets of the inference engine. The height defuzzification calculates output y as:

$$y = \frac{\sum_{l=1}^{7} \bar{y}^l \, \mu_{B^l}(\bar{y}^l)}{\sum_{l=1}^{7} \mu_{B^l}(\bar{y}^l)} \qquad (7.27)$$

where $\bar{y}^l$ is the center of gravity of the fuzzy set B^l. Regardless of whether minimum or product inference is used, the center of gravity for the Gaussian consequent membership function is at the center value of the Gaussian function. Computational simplicity was the main criteria for choosing the height defuzzifier. It is crucial to reduce computational expense as much as possible for real time systems. Moreover, the designed FIS must be run on a microcontroller which has less computational ability compared to a PC.

The output, y, of the FIS can be formulated by substituting (7.25) and (7.26) into (7.27):

$$y = \frac{\sum_{l=1}^{7} \bar{y}^l \times \min\left[\exp\left\{-\frac{1}{2}\left[\frac{x_1 - m_1^{l}}{\sigma_1^l}\right]^2\right\}, \exp\left\{-\frac{1}{2}\left[\frac{x_2 - m_2^{l}}{\sigma_2^l}\right]^2\right\}\right]}{\sum_{l=1}^{7} \min\left[\exp\left\{-\frac{1}{2}\left[\frac{x_1 - m_1^{l}}{\sigma_1^l}\right]^2\right\}, \exp\left\{-\frac{1}{2}\left[\frac{x_2 - m_2^{l}}{\sigma_2^l}\right]^2\right\}\right]} \tag{7.28}$$

This mathematical formula can describe our FIS completely. It maps a crisp input vector, $\mathbf{x}$, directly into a crisp output, y. Moreover, only this formula can be used directly on the microcontroller. Please note that it has been assumed that membership functions are normalized, so that $\mu_{G^l}(\bar{y}^l) = 1$. σ_1^l, σ_2^l, m^l, and m^l can be found from Table 7-1 for rules $l=1,\ldots,7$.

The mathematical formula obtained in (7.28) can be represented as:

$$y = \sum_{l=1}^{7} \bar{y}^l \varphi_l(\mathbf{x})$$

Where $\phi_l(\mathbf{x})$ is called Fuzzy Basis Functions (FBFs) and is given by

$$\varphi_l(\mathbf{x}) = \frac{\bar{y}^l \times \min\left[\exp\left\{-\frac{1}{2}\left[\frac{x_1 - m_1^{l}}{\sigma_1^l}\right]^2\right\}, \exp\left\{-\frac{1}{2}\left[\frac{x_2 - m_2^{l}}{\sigma_2^l}\right]^2\right\}\right]}{\sum_{l=1}^{7} \min\left[\exp\left\{-\frac{1}{2}\left[\frac{x_1 - m_1^{l}}{\sigma_1^l}\right]^2\right\}, \exp\left\{-\frac{1}{2}\left[\frac{x_2 - m_2^{l}}{\sigma_2^l}\right]^2\right\}\right]} \tag{7.29}$$

7.3.5 Results

Fifty-one pairs of data (femur and tibia inclination angles) were inserted into the designed Mamdani FIS to assess the performance of the system. Results are shown in Figure 7-14 and Figure 7-15. It is revealed that the outputs of the designed FIS cannot follow the desired ones closely. It has been verified that increasing the number of input membership functions and subsequently the number of rules can enhance the performance of the FIS. This will lead to high computational cost and change nature of partitioning training data.
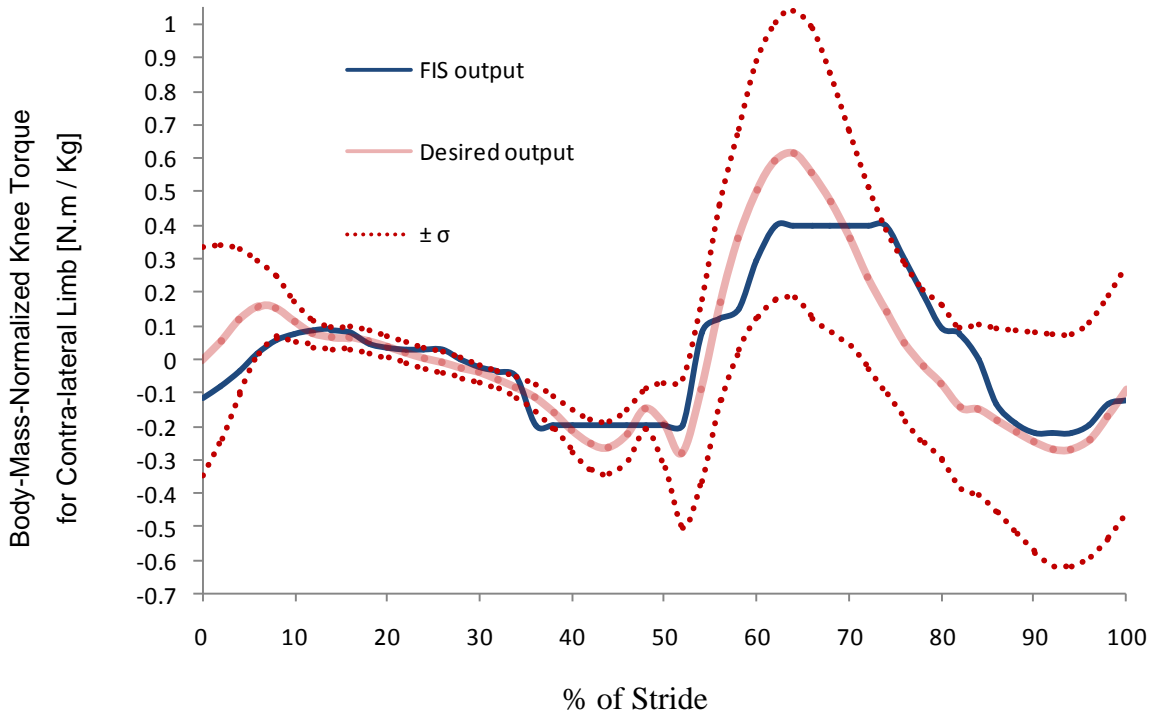
Figure 7-14: The first output of the designed Mamdani FIS
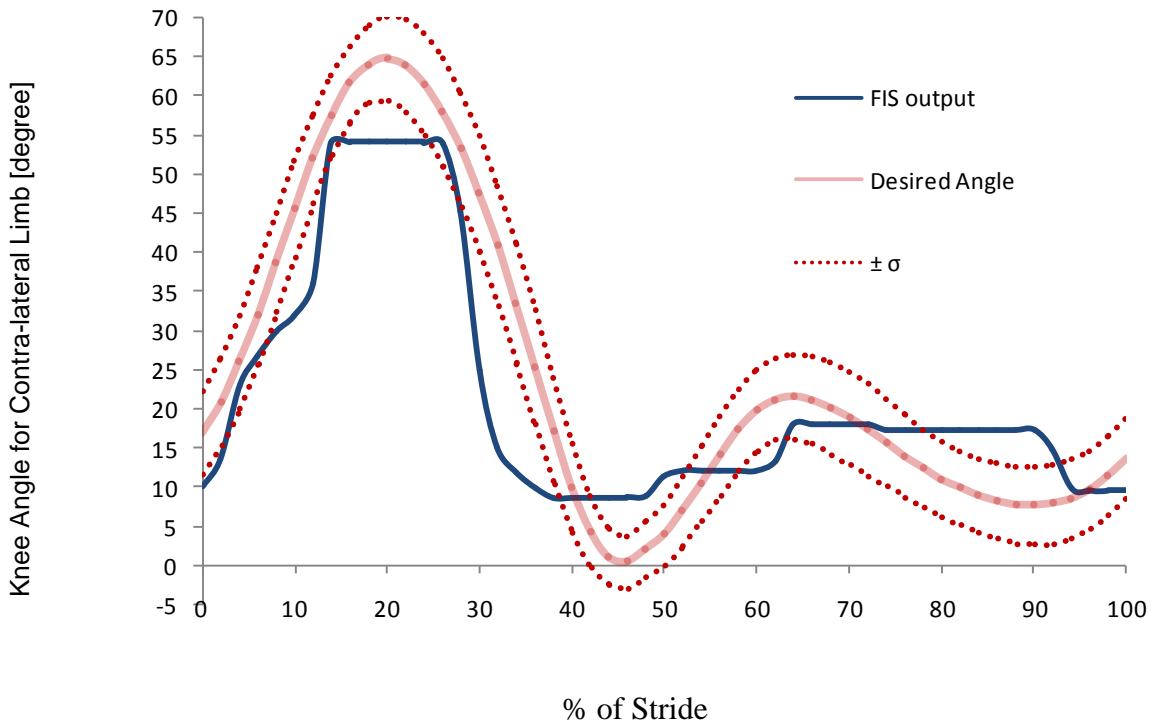
Figure 7-15: The second output of the designed Mamdani FIS

98

7.3.6 Selecting Non-Singleton Fuzzifier

When input data are corrupted by measurement noise, a non-singleton fuzzifier can handle such uncertainties.   In a non-singleton fuzzifier $\mu_{A^*}(\mathbf{x}') = 1$ and $\mu_{A^*}(\mathbf{x})$ decrease from unity as $\mathbf{x}$ moves away from $\mathbf{x}'$. A fuzzy membership function is associated with $\mathbf{x}'$. In this work, the mentioned membership functions are considered Gaussian to maintain the coherence with the type of input/output membership functions.

$$\mu_{A_{\mathbf{x}}}(\mathbf{x}) = \mu_{A_{x_1}}(x_1) \otimes \mu_{A_{x_2}}(x_2) \tag{7.30}$$

$$\mu_{A_{x_j}}(x_j) = \exp\left\{ -\frac{1}{2}\left[\frac{x_j - m_{A_{x_j}}}{\sigma_{A_{x_j}}} \right]^2 \right\} \tag{7.31}$$

where $A_{x_i} \subset U_i (i = 1,2)$ are the fuzzy sets describing the inputs. (7.23) can be re-expressed as:

$$\mu_{B^l}(y) = \mu_{G^l}(y) \otimes \left[\left[\sup_{\mathbf{x}\in U} \mu_{A_{x_1}}(x_1) \otimes \mu_{F_1^l}(x_1) \right] \otimes \left[\sup_{\mathbf{x}\in U} \mu_{A_{x_2}}(x_2) \otimes \mu_{F_2^l}(x_2) \right] \right] \tag{7.32}$$

Where the rule index $l = 1, \ldots, M$. We can define

$$\mu_{Q_j^l}(x_j) = \mu_{A_{x_j}}(x_j) \otimes \mu_{F_j^l}(x_j) \tag{7.33}$$

where j is input index. Assuming that the supremum of $\mu_{Q_j^l}(x_j)$ occurs at a single point of $x_{j,\max}^l$, (7.32) can be re-written as:

$$\mu_{B^l}(y) = \mu_{G^l}(y) \otimes \left[\mu_{Q_1^l}(x_{1,\max}^l) \otimes \mu_{Q_2^l}(x_{2,\max}^l) \right] \tag{7.34}$$

the right term in the above equation is the firing level for non-singleton type-1 FIS. Mouzouris et al [43] proved that if all membership functions are assumed Gaussian (same as this work) and t-norms as product, then (7.33) is maximum at

$$x_{j,\text{max}}^l = \frac{\sigma_{A_{x_j}}^2 m_j^l + \sigma_{l_j}^2 m_{A_{x_j}}}{\sigma_{A_{x_j}}^2 + \sigma_{l_j}^2} \tag{7.35}$$

and the maximum value of (7.33) is equal to

$$\mu_{Q_j^l}(x_{j,\text{max}}^l) = \exp\left\{-\frac{1}{2}\frac{\left(m_{A_{x_j}} - m_j^l\right)^2}{\sigma_{A_{x_j}}^2 + \sigma_{l_j}^2}\right\} \tag{7.36}$$

If the same level of uncertainty for all input points (measurements) is supposed, $\sigma_{A_{x_j}}$ in (7.36) is constant and equal to σ_A. Also, the crisp input x_j' can be considered as the mean of the fuzzy input sets. Therefore (7.35) and (7.36) can be re-expressed as:

$$x_{j,\text{max}}^l = \frac{\sigma_A^2 m_j^l + \sigma_{l_j}^2 x_j'}{\sigma_A^2 + \sigma_{l_j}^2} \tag{7.37}$$

$$\mu_{Q_j^l}(x_{j,\text{max}}^l) = \exp\left\{-\frac{1}{2}\frac{\left(x_j' - m_j^l\right)^2}{\sigma_A^2 + \sigma_{l_j}^2}\right\} \tag{7.38}$$

Moreover, Mouzouris et al [43] has shown that in the case of minimum t-norm (7.37) will be changed to

$$x_{j,\text{max}}^l = \frac{\sigma_{A_{x_j}} m_j^l + \sigma_j^l m_{A_{x_j}}}{\sigma_{A_{x_j}} + \sigma_j^l} \tag{7.39}$$

Comparing (7.26) and (7.38) reveals that for this special circumstance, the only difference between singleton and non-singleton FIS which has product t-norm and Gaussian membership functions is the variance, which becomes broader from $\sigma_{l_j}^2$ to $\sigma_A^2 + \sigma_{l_j}^2$. That means the non-singleton FIS has larger firing level. Therefore, we can

adjust σ_A to the error range of utilized sensor which is provided by the specification of sensor or supplier. Considering this uncertainty can enhance the performance of the controller.

7.4 Proposed TSK FIS

The second control system was built using the Takagi-Sugeno-Kang (TSK) fuzzy inference engine. Compared to the Mamdani system, the TSK system is more compact and efficient in terms of online computation. Many features of the two systems are analogous. Fuzzifying the inputs and obtaining rule firing-levels are absolutely similar. The systems differ in the structure of their rule consequences. The consequence of a Mamdani rule is a fuzzy set, whereas TSK output membership functions are a linear combination of the input variables. Moreover, a TSK FIS does not include a defuzzifier.[5] The TSK is not able to compensate for the uncertainties of measurement; therefore, there is no non-singleton TSK FIS. All the rules used in the proposed TSK FIS are type-1. Hence, the rules of the first-order TSK FIS are expressed as

$$R_l: \quad \text{IF} \quad x_1 \text{ is } Ph_1^l \quad \text{AND} \quad x_2 \text{ is } Ph_2^l \quad \text{THEN } y_1^l(\mathbf{x}) = c_{1,0}^l + c_{1,1}^l x_1 + c_{1,2}^l x_2$$
$$y_2^l(\mathbf{x}) = c_{2,0}^l + c_{2,1}^l x_1 + c_{2,2}^l x_2$$

where x_1 and x_2 are input 1 (femur angle) and input 2 (tibia angle); $y_1^l(\mathbf{x})$ and $y_2^l(\mathbf{x})$ represent the first output and second output of l-th rule corresponding to the knee torque and the angular position of the prosthesis; $c_{1,0}^l \cdots c_{1,2}^l$ and $c_{2,0}^l \cdots c_{2,2}^l$ are consequent parameters for the first and second output, respectively, for the l-th rule; and Ph_j^i is defined as the phase fuzzy state i for the j-th input. Therefore, for the proposed TSK FIS, all the antecedent fuzzy sets remain unchanged.

The final i-th output (i= 1, 2 associated with prosthetic knee torque and angular position, respectively) of the FIS can be achieved by following equations:

---

[5] Preliminaries section provides more details about the principle of the TSK's fuzzy inference method.

$$y_{i\,\text{TSK},1}(\mathbf{x}) = \frac{\sum_{l=1}^{M} f^l(\mathbf{x}) y_i^l(\mathbf{x})}{\sum_{l=1}^{M} f^l(\mathbf{x})} = \frac{\sum_{l=1}^{M} f^l(\mathbf{x})\left(c_{i,0}^l + c_{i,1}^l x_1 + c_{i,2}^l x_2\right)}{\sum_{l=1}^{M} f^l(\mathbf{x})} \tag{7.40}$$

where M is the number of rules, which is equal to seven for the system under study (Figure 7-16); $f^l(\mathbf{x})$ is the rule firing level and is here defined as

$$f^l(\mathbf{x}) = T_{k=1}^p \mu_{F_j^l}(x_j) \tag{7.41}$$

in which T denotes a t-norm (usually the minimum or product operator), and $\mu_{F_j^l}(x_j)$ is the membership value of the j-th input associated with the l-th rule. In (7.40) and (7.41), $\mathbf{x}$ denotes a specific input vector that is applied to the type-1 TSK FIS. As shown in (7.41), the rule firing level is identical for both final outputs of the TSK system, $y_{1\,\text{TSK},1}^l(\mathbf{x})$ and $y_{2\,\text{TSK},1}^l(\mathbf{x})$, since the input membership values, $\mu_{F_j^l}(x_j)$, are identical for both outputs. The relational matrix for the designed FIS is depicted in Figure 7-16.

Figure 7-16: The rational matrix describing the rule base of the TSK model. y_i^l: the i-th output of the i-th rule

A critical step in the design of the TSK model, is to determine the consequent parameters, $c_{i,0}^l \cdots c_{i,2}^l$ ($i=$ 1, 2). To achieve this purpose, a collection of N training pairs of input-output numerical data, ($\mathbf{x}^{(1)}$ $\mathbf{y}^{(1)}$), ($\mathbf{x}^{(2)}$ $\mathbf{y}^{(2)}$),… ,($\mathbf{x}^{(N)}$ $\mathbf{y}^{(N)}$), must be given, where $\mathbf{x}$ and $\mathbf{y}$ are the input and output vectors, respectively, and the dimension of each is two. In this thesis, the number of rules and the antecedent parameters (the mean and the standard deviation of each input fuzzy set) are fixed ahead of time, hence only consequent parameters must be designed. For the p-input, i-output, and M-rule TSK FIS, the total number of consequent parameters is (p+1)$\times i \times M$. Therefore, we have eighteen consequent parameters, (2+1)$\times$2$\times$3, for the proposed FIS. The number of training pairs must be bigger than the number of unknown parameters. Fifty one training pairs were selected from Winter's work [31]. Note that to achieve the desired input-output mapping data, the outputs of training pairs, $\mathbf{y}^{(N)}$=[y_1 y_2]$^\mathrm{T}$, are the angular position and torque of the contra-lateral leg. Therefore, the data in Figure 7-6 and Figure 7-7 must be shifted by 50% to obtain the training data (Figure 7-8 and Figure 7-9).

Two methods are introduced here to obtain the unknown parameters: Least Square and Adaptive-Network-based Fuzzy Inference System (ANFIS). In both techniques, the consequent parameters of each output were found separately. Hence, 51 training pairs , ($\mathbf{x}^{(1)}$ $\mathbf{y}^{(1)}$), ($\mathbf{x}^{(2)}$ $\mathbf{y}^{(2)}$),… , ($\mathbf{x}^{(51)}$ $\mathbf{y}^{(51)}$), were divided into two sets of 51 training pairs: ($\mathbf{x}^{(1)}$ $y_1^{(1)}$), ($\mathbf{x}^{(2)}$ $y_1^{(2)}$),… , ($\mathbf{x}^{(51)}$ $y_1^{(51)}$) and ($\mathbf{x}^{(1)}$ $y_2^{(1)}$), ($\mathbf{x}^{(2)}$ $y_2^{(2)}$),… , ($\mathbf{x}^{(51)}$ $y_2^{(51)}$), where $\mathbf{x}$ is the input vector (dimension: 2); y_1 and y_2 are the first and second scalar outputs of FIS.

7.4.1 Least Square Method

Using the training data to tune the output parameters can be achieved readily by the least square optimization method (LS) assuming the shapes and parameters of all the input fuzzy sets are fixed ahead of time. To perform the least square method, variable $\bar{f}^l(\mathbf{x})$ is introduced as

$$\bar{f}^l(\mathbf{x}) = \frac{f^l(\mathbf{x})}{\sum_{l=1}^M f^l(\mathbf{x})} \tag{7.42}$$

Then, the output equation of TSK FIS, (7.40), can be rewritten as

$$y_{i\,\text{TSK,1}}(\mathbf{x}) = \sum_{l=1}^{M} \bar{f}^l(\mathbf{x})\, y_i^l(\mathbf{x}) = \sum_{l=1}^{M} \bar{f}^l(\mathbf{x})\left(c_{i,0}^l + c_{i,1}^l x_1 + c_{i,2}^l x_2\right) \tag{7.43}$$

Rewriting equation (7.43) in a more compact form, we get

$$y_{i\,\text{TSK,1}}(\mathbf{x}) = \phi\, C_i \tag{7.44}$$

where

$$C_i = \begin{bmatrix} c_{i,0}^1 \cdots c_{i,0}^M & c_{i,1}^1 \cdots c_{i,1}^M & c_{i,2}^1 \cdots c_{i,2}^M \end{bmatrix}^T$$

$$\phi = \begin{bmatrix} \bar{f}^1(\mathbf{x}) \cdots \bar{f}^M(\mathbf{x}) & x_1\bar{f}^1(\mathbf{x}) \cdots x_1\bar{f}^M(\mathbf{x}) & x_2\bar{f}^1(\mathbf{x}) \cdots x_2\bar{f}^M(\mathbf{x}) \end{bmatrix}$$

If we have N sets of input-output as training data, ϕ will have N rows, as depicted in the following format. The notation $\bar{f}^l$ in following matrix is altered slightly to $\bar{f}_l$, i.e., $\bar{f}_l \ \square \ \bar{f}^l(\mathbf{x})$. Moreover, for the nth set of training data we have $\bar{f}_l^n$, where $n=1, \ldots, N$

$$\phi = \begin{bmatrix} \bar{f}_1^1 \cdots \bar{f}_M^1 & x_1^1\bar{f}_1^1 \cdots x_1^1\bar{f}_M^1 & x_2^1\bar{f}_1^1 \cdots x_2^1\bar{f}_M^1 \\ \bar{f}_1^2 \cdots \bar{f}_M^2 & x_1^2\bar{f}_1^2 \cdots x_1^2\bar{f}_M^2 & x_2^2\bar{f}_1^2 \cdots x_2^2\bar{f}_M^2 \\ \bar{f}_1^N \cdots \bar{f}_M^N & x_1^N\bar{f}_1^N \cdots x_1^N\bar{f}_M^N & x_2^N\bar{f}_1^N \cdots x_2^N\bar{f}_M^N \end{bmatrix}$$

x_j^n means the j-th input for the nth set of training data. The parameters vector, C, can be obtained using the following procedure:

$$\phi\, C_i = y_i$$
$$\phi^T \phi\, C_i = \phi^T y_i$$
$$C_i = \left(\phi^T \phi\right)^{-1} \phi^T y_i$$

$$C_i = \phi^+ y_i \tag{7.45}$$

where ϕ^+ is the pseudo-inverse matrix for ϕ .

7.4.2 ANFIS

The second method to find the unknown parameters of a TSK FIS is ANFIS (Adaptive-Network-based Fuzzy Inference System) technique. A type-1 TSK FIS can be considered as a network that is composed of five layers. An example of two-input two-rule one-output ANFIS structure is depicted in Figure 7-17 (two membership functions for each input). Inputs of the FIS come into the first layer where the premise parameters are stored. Membership values of inputs are calculated and will be sent to the next layer. The second layer computes the firing level of rules based on the defined t-norm. In the third layer, the ratio of each rule's firing level to the sum of all rules' firing levels will be calculated, and the results will launch the fourth stage. The forth layer gives $\bar{f}^l(\mathbf{x})\,y^l(\mathbf{x})$ for each rule based on the accumulated consequent parameters in this layer. The fifth layer computes the overall output as a summation of all incoming signals. In order to achieve the desired input-output mapping, the given training data are fed forward to the network, and consequent parameters at layer four are identified by the least square estimate. In the backward pass, while output parameters are fixed, the error rates propagate backward and premise parameters are updated by the gradient descent [44]. Therefore in this technique, although the antecedent parameters are fixed ahead of time, they will be tuned during the training process as will the consequent parameters. This iterative method continues until the sum of the squared errors over all the N training data becomes less than a predefined threshold.
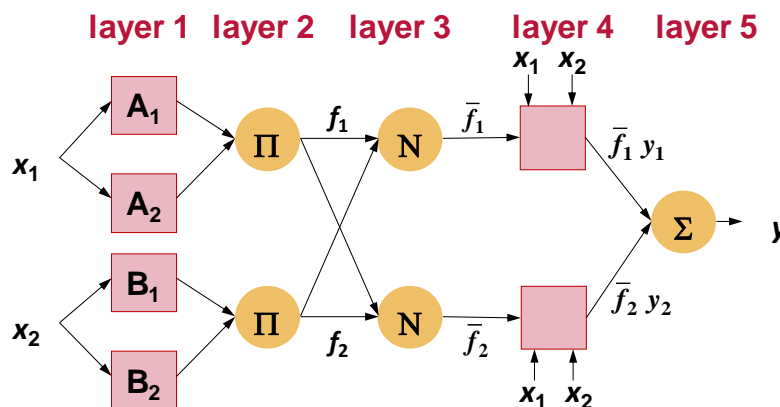

Figure 7-17: A TSK FIS structure in the form of ANFIS

105

To measure the effect of the last output (at the previous time instance) on the current output of the system, the structure of the fuzzy model was revised. For the comparison of the current state of each input with its last state, the premise will read as

$$\text{IF } x_j(k) \text{ is } \text{Ph}_j^i \quad \text{AND}\left(x_j(k-1) \text{ is } \text{Ph}_j^i \text{ OR } x_j(k-1) \text{ is } \text{Ph}_j^{i-1}\right)$$

where j is the input index, which can be 1 or 2. The above statement means that if the current state of input j is in phase i, the previous state of that input must be in the same phase or in the one before. Note that the phase number 0 is the same as phase number 7 since the input is iterative[6]. As described earlier, the femur and tibia state at any time must be at same phase. Moreover, the rules that use a combination of "AND" and "OR" connectives can be decomposed into a group of rules with just AND connectives for processing using only t-norms. As a result, the two successive rules of the new FIS can be expressed thus:

$$R_l \; : \; \text{IF} \qquad x_1(k) \text{ is } \text{Ph}_1^i \quad \text{AND} \quad x_1(k-1) \text{ is } \text{Ph}_1^{i-1} \quad \text{AND} \quad x_2(k) \text{ is } \text{Ph}_2^i \quad \text{AND} \quad x_2(k-1) \text{ is } \text{Ph}_2^{i-1}$$
$$\text{THEN} \quad y_1^l = c_{1,0}^l + c_{1,1}^l x_1 + c_{1,2}^l x_2 + c_{1,3}^l x_3 + c_{1,4}^l x_4$$
$$y_2^l = c_{2,0}^l + c_{2,1}^l x_1 + c_{2,2}^l x_2 + c_{2,3}^l x_3 + c_{2,4}^l x_4$$
$$R_{l+1} : \; \text{IF} \qquad x_1(k) \text{ is } \text{Ph}_1^i \quad \text{AND} \quad x_1(k-1) \text{ is } \text{Ph}_1^i \quad \text{AND} \quad x_2(k) \text{ is } \text{Ph}_2^i \quad \text{AND} \quad x_2(k-1) \text{ is } \text{Ph}_2^i$$
$$\text{THEN} \quad y_1^{l+1} = c_{1,0}^{l+1} + c_{1,1}^{l+1} x_1 + c_{1,2}^{l+1} x_2 + c_{1,3}^{l+1} x_3 + c_{1,4}^{l+1} x_4$$
$$y_2^{l+1} = c_{2,0}^{l+1} + c_{2,1}^{l+1} x_1 + c_{2,2}^{l+1} x_2 + c_{2,3}^{l+1} x_3 + c_{2,4}^{l+1} x_4$$

In the above expression, l indicates the rule number, where (l and $l+1$) = (1 and 2), (3 and 4), …, (13 and 14); for the l-th rule, $c_{1,0}^l \cdots c_{1,4}^l$ and $c_{2,0}^l \cdots c_{2,4}^l$ are consequent parameters for the first and second output, respectively; $x_j(k)$ and $x_j(k-1)$ (for j=1 and 2) can be considered as separated inputs that are associated with the same variable: femur or tibia angle. Hence, the membership functions related to $x_j(k)$ and $x_j(k-1)$ are the same.

---

[6] Section 1.2.3 and Figure 1-4 provide more information on gait cycle

Consequently, the FIS under consideration has four inputs, fourteen membership functions, and fourteen rules.

Fifteen percent of the data represented by Winter [31] were selected as testing data; these numbers were not introduced to TSK FIS during the training process either by ANFIS or by LS. Testing data were presented to the trained FIS in order to see how well the FIS model predicts the corresponding data set output values. Root Mean Square Errors (RSME) of the training data obtained by LS are less than that obtained by ANFIS (Equation(7.46)). However, acquired input and consequent parameters by ANFIS are chosen for TSK FIS since they showed smaller errors for the test data. This implies that for this study, the designed FIS by LS was exposed to the effect of model over-fitting. The FIS outputs for the training data are depicted in Figure 7-8 and Figure 7-9. As described before, during training, the proposed FIS was considered as two separated fuzzy systems for each output, ($y_{1\text{TSK},1}(\mathbf{x})$ and $y_{2\text{TSK},1}(\mathbf{x})$), and they were trained individually even though they have identical input membership functions. After training, both systems considered as one FIS with two outputs and two inputs. The control diagram of the designed controller is depicted in Figure 7-18.

$$\text{RMSE}=\sqrt{\frac{1}{n}\sum_{i=1}^{n}e_i} \qquad (7.46)$$
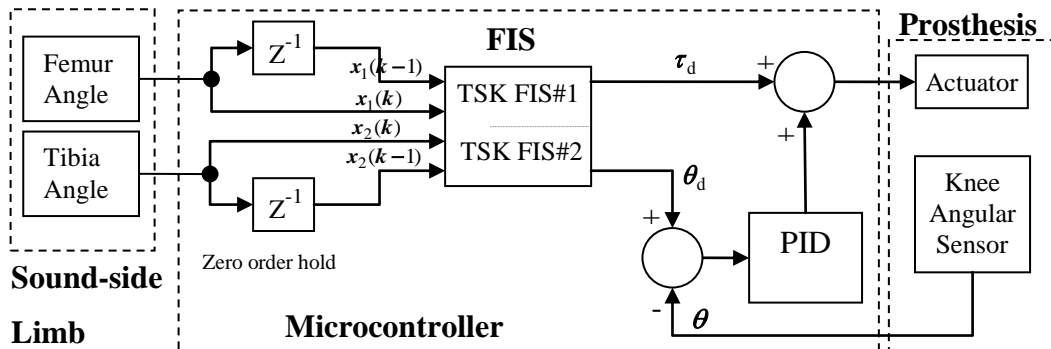
Figure 7-18: The designed control diagram based on TSK FIS, Control diagram of prosthetic knee. τ_d and θ_d **are the desired knee torque and position of prosthesis, respectively, and** τ **and** θ **are the real ones**

107
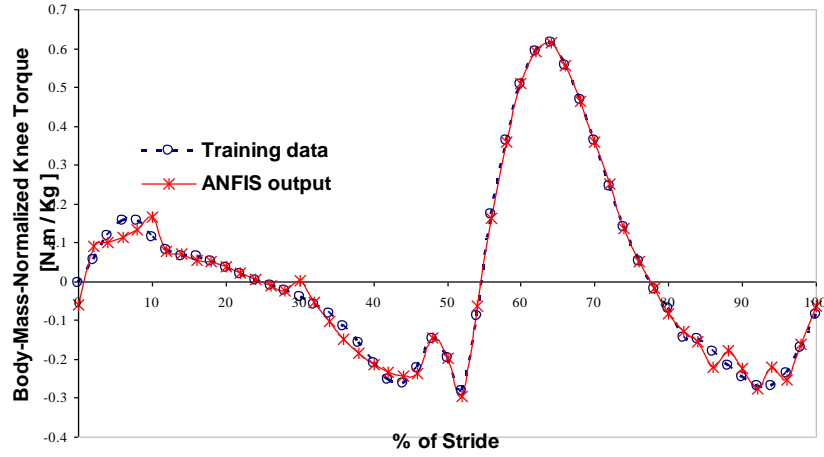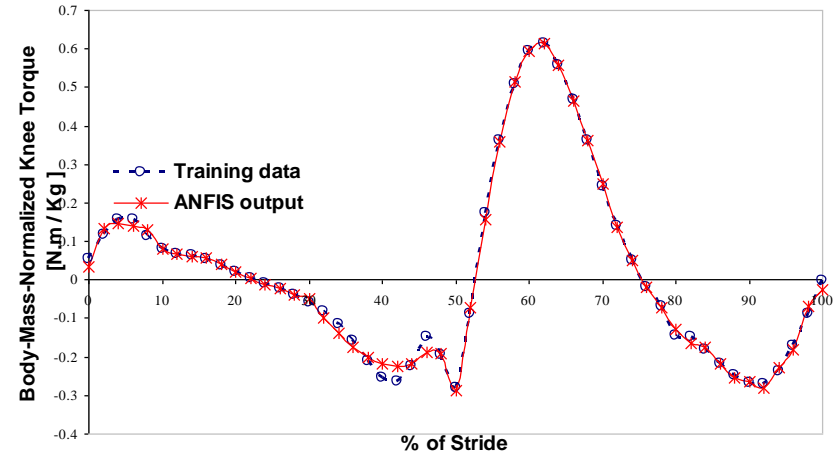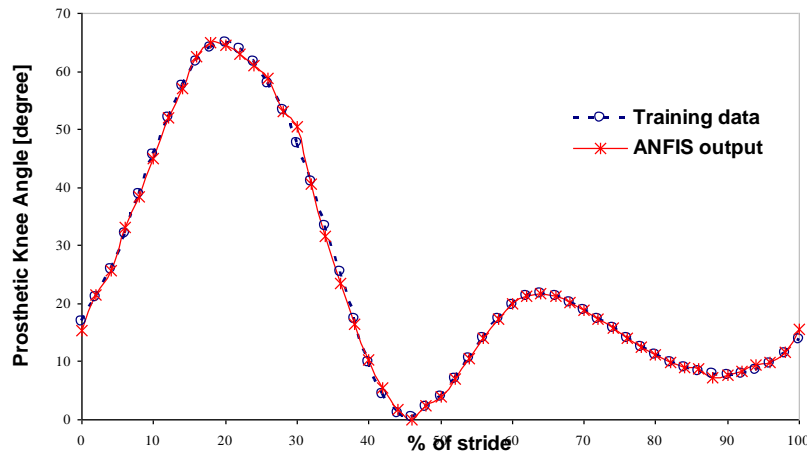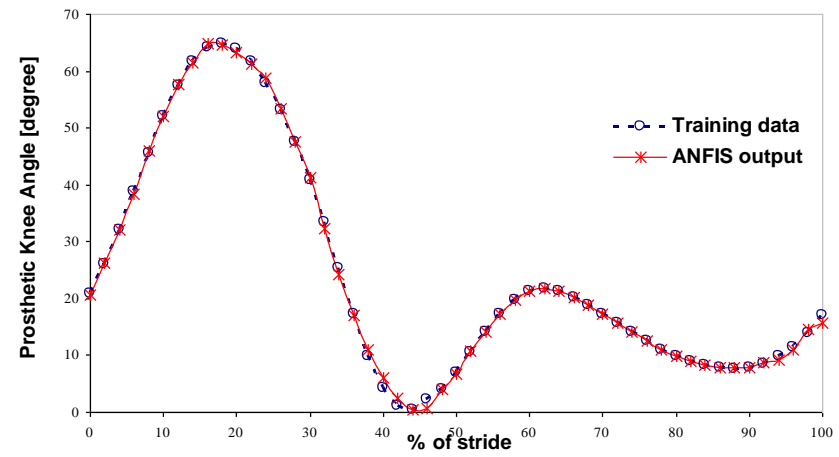
Figure 7-19: ANFIS output torque vs. training data: (a), (b) illustrate output 1; (c), (d) illustrate output 2. Current and former statuses of inputs are: (a), (c) in the same phase and (b), (d) in successive phases.

There is an expectation in the aforementioned rules that the consequent parameters of the same output must be identical for two successive rules, i.e., $c_{j,i}^{l} = c_{j,i}^{l+1}$ (for j = 1, 2 and i = 0, …, 4). In order to verify this assumption, these consequent parameters obtained after training process are plotted in Figure 7-20 and Figure 7-21.

Moreover, since in ANFIS method not only the output parameters but also the input parameters are tuned, comparisons between the input parameters of trained and untrained FIS are accomplished in Figure 7-22 and Figure 7-23.
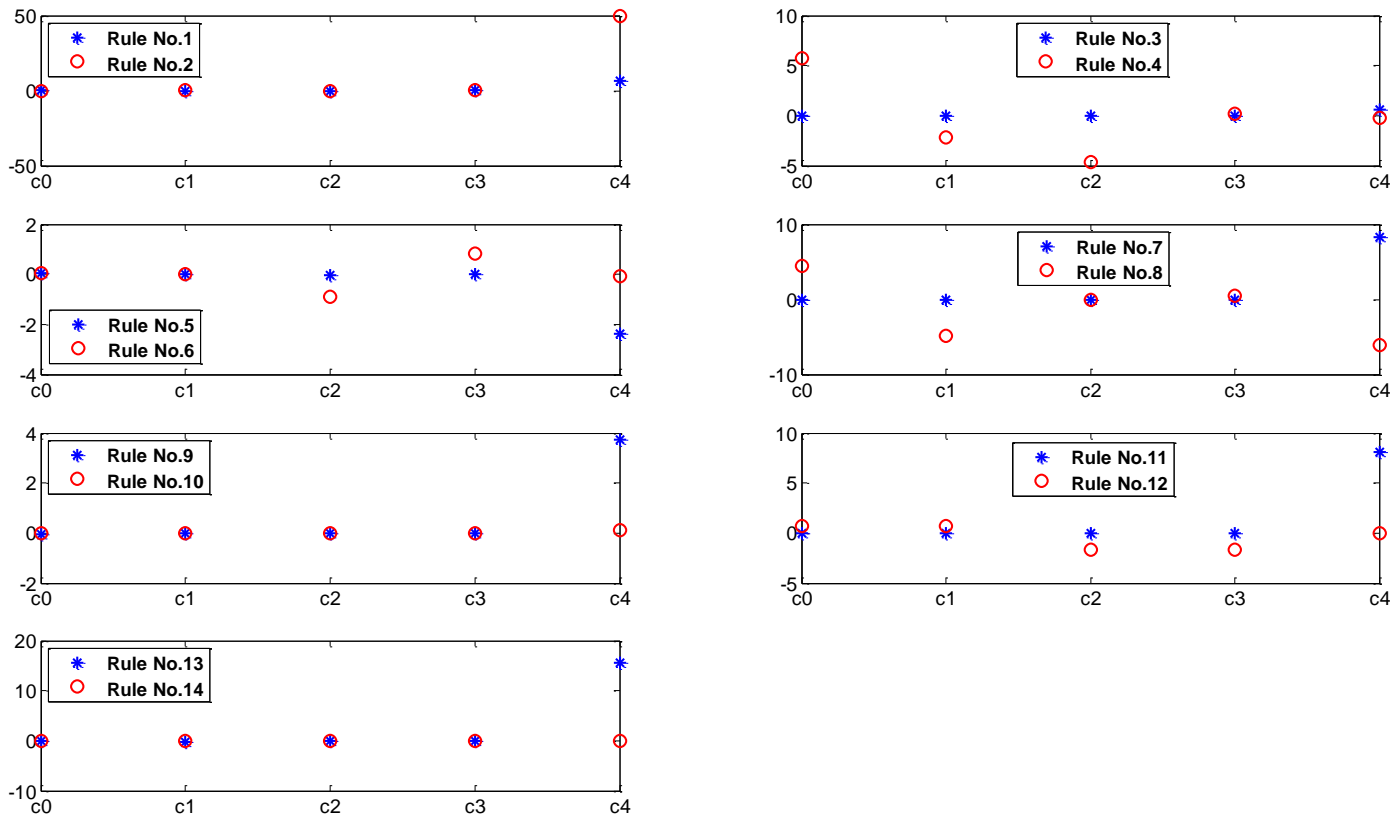
Figure 7-20: The comparison between the first output parameters of two successive rules, i.e. $c_{1,i}^{l}$ **and** $c_{1,i}^{l+1}$ **. Note that** $c_{1,i}^{l}$ **and** $c_{1,i}^{l+1}$ **are indicated by** c_i **for simplicity (i=0,..., 4).**
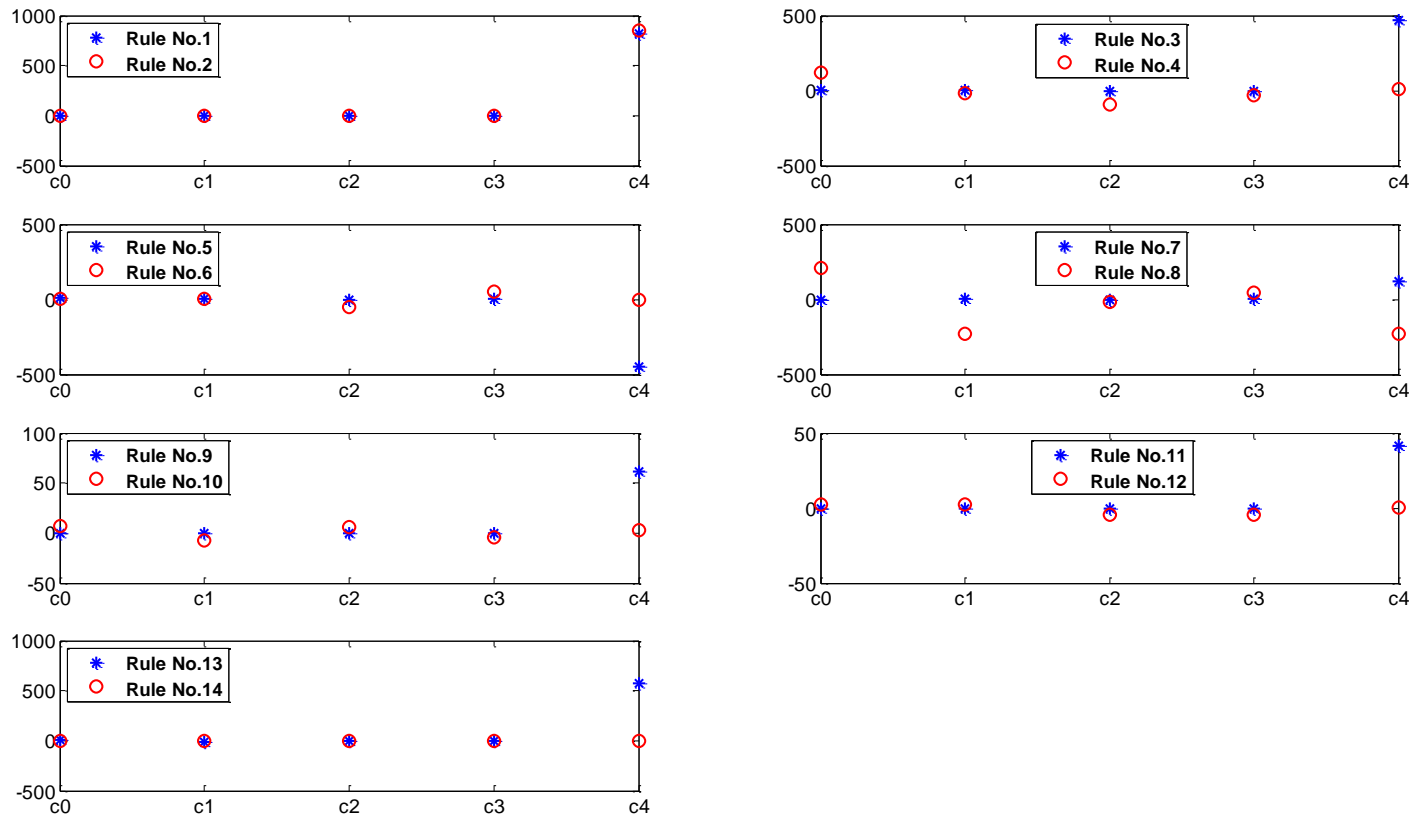
Figure 7-21: The comparison between the second output parameters of two successive rules, i.e. $c^l_{2,i}$ **and** $c^{l+1}_{2,i}$ **. Note that** $c^l_{1,i}$ **and** $c^{l+1}_{1,i}$ **are indicated by** c_i **for simplicity (i=0,…, 4).**
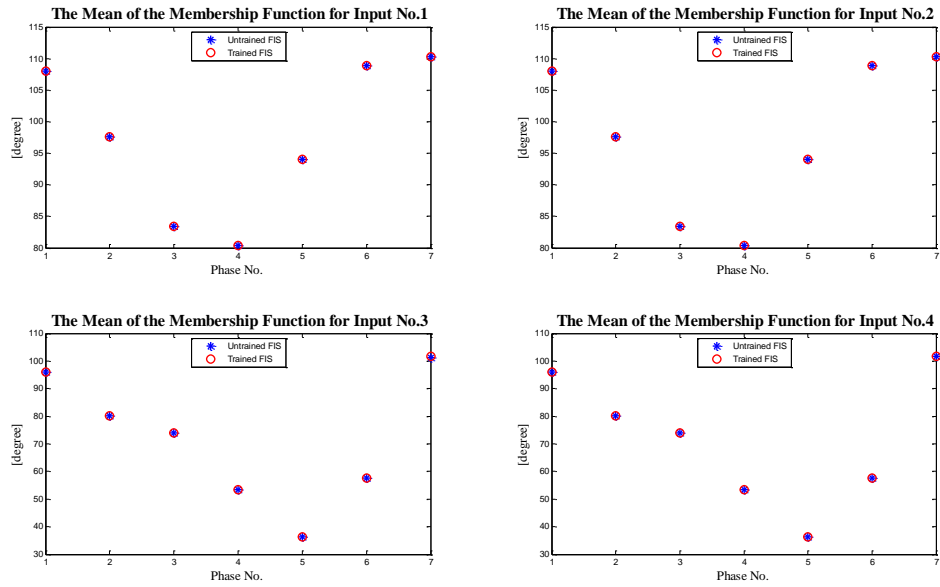
(a)
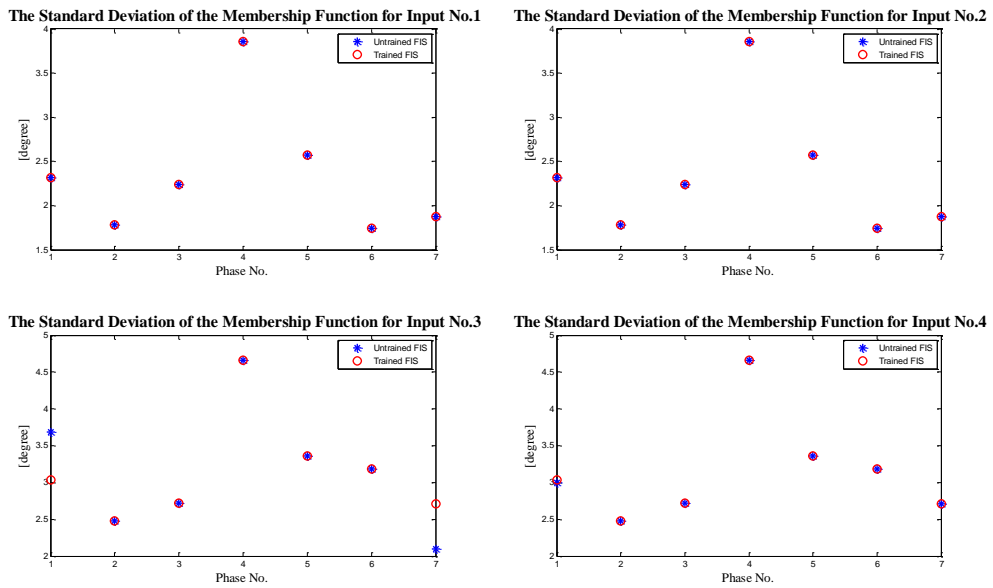
(b)

Figure 7-22: The comparison between the trained and untrained input membership function parameters for TSK FIS #1 in Figure 7-18: (a) mean (b) standard deviation

112
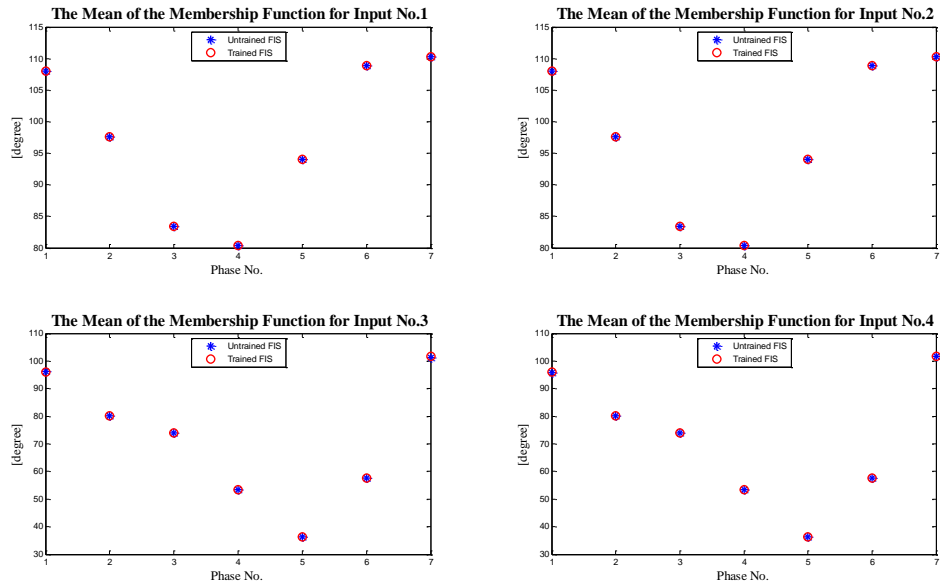
(a)
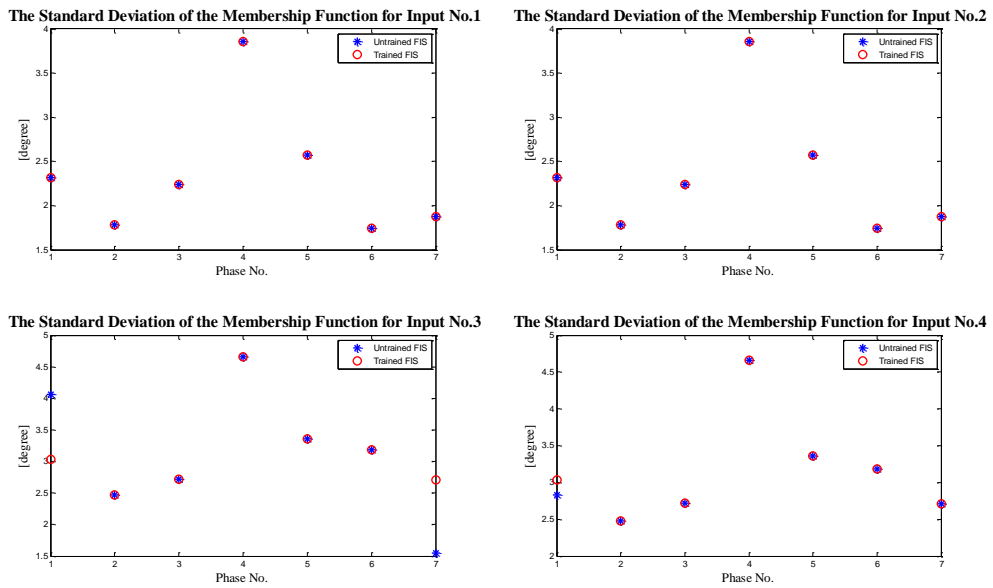
(b)

Figure 7-23: The comparison between the trained and untrained input membership function parameters for TSK FIS #2 in Figure 7-18: (a) mean (b) standard deviation

7.5 Post Processing Block and Secondary Controller

A saturation block is introduced after the FIS block in Figure 7-24 to enforce upper and lower limits on the values of command torque and angle to the prosthesis. A Post Processing Block (PBB) is used on the test data. Since human walking is a harmonic motion, the current and last states of torque/motion are correlated. A threshold, γ, is defined for the last state of each output; if the current output is not within the threshold of the last data, the case will be considered as an error, and the current output will be multiplied by a ratio, $+\alpha$ or $-\alpha$, depending on the increment or decrement of current output compared with those in the previous state. The levels of γ and α are defined based on the sample rate of the angular sensors mounted on the healthy leg. For the simulation, γ and α are chosen as 1.25 and 1.15, respectively. The error of test data is summarized in Table 7-2 for the FIS obtained by the ANFIS method. As shown, the PPB plays a significant role in reducing the magnitude of error for the test data.
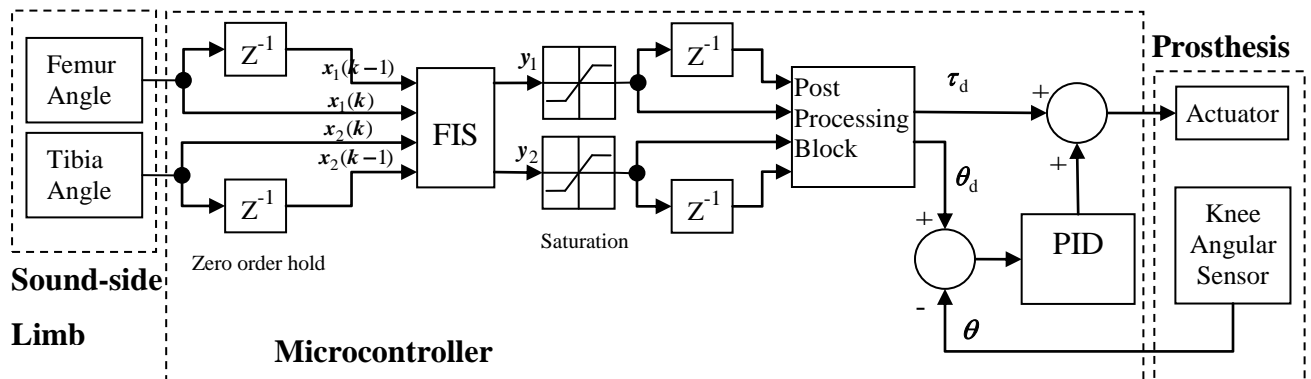
Figure 7-24: Ultimate control diagram of prosthetic knee. τ_{d} and θ_{d} are the desired knee torque and position of prosthesis, respectively, and τ and θ are the real ones

Table 7-2: Root mean square error for 10 test data

Set #	RMSE after FIS		RMSE after PPB	
	$y_1 = \tau\,[\mathrm{Nm/Kg}]$	$y_2 = \theta\,[°]$	$y_1 = \tau\,[\mathrm{Nm/Kg}]$	$y_2 = \theta\,[°]$
1	0.1269	3.2784	0.0598	3.2784
2	0.2194	17.421	0.1085	8.5574
3	0.474	13.5451	0.1903	5.4714

114

7.6 Discussion

Comparing Figure 7-19 and Figure 7-14 – Figure 7-15, the designed TSK FIS has a better performance than the Mamdani one. However, the designed Mamdani FIS was more robust since by introducing test data to the Mamdani FIS, the outputs show a lower variation from the reference data. Therefore, to increase the robustness of the designed TSK FIS against the test data, saturation blocks and PPB were offered to the control system.

Uncertainty in joint angles measurements due to the different pattern of normal walking cycle between individual or even day-to-day activity of same subject (inter- and intra-subject) are considered in designing the knowledge-based system. Moreover, uncertainty of input data corrupted by measurement noise was discussed very briefly. However, due to uncertainty of definition of slow, normal, and fast walking, uncertainty of Gaussian input membership functions must be consider to increase the robustness of the model. This leads to uncertainty about determining the membership value of the entered data (type-2 FIS). Therefore, further study is needed to develop a type-2 FIS for the APK controller.

Chapter 8
CONCLUSION AND FUTURE WORK

8.1 Conclusion

The APK project has two main goals: first, to decrease the energy expenditure of the amputees during ambulation by allowing the prosthetic to fully power the knee joint and second, to provide a low-cost effective prosthesis.

The 6-DOF complex biological knee is simplified and modeled to 1-DOF. Having a mechanically simple system leads to a very accurate control of the system. The APK is driven by one rotary motor inserted inside the knee joint. The APK actuator is reinforced by a ball-screw system. This gearing reduction increases the torque produced by the motor required for the APK. Thus, this design overcomes the problem of insufficient generated torque during the stance phase, which is common in other actives prosthetic legs. Once the APK was fabricated, the research also delved into design study of a passive ankle joint to expand the fabricated APK.

The test-bed is manufactured to replicate lower limb motion. This simulator consists of a pneumatic circuit to mimic the femur displacement at various speeds, a hip unit to simulate pelvic motion, and a treadmill to provide the ground reaction force. In other words, the main duty of the test bed is to imitate the relative motion of the entire leg in respect to the ground. Moreover, the test stand provides experimentation analysis.

Different types of sensing systems (electromyography and lower limb inclination angles) are investigated to extract signals from the user's intact leg and send the captured data to the APK controller. The methodology to measure each type of signal is described. Due to the assembling problem of EMG, high sensitivity to noise, and temperature variation, an angular position of the healthy thigh and shank was chosen as the source of input. Then, different techniques were discussed to measure the inclination. The potentiometer together with the accelerometer show moderately accurate data reading. A better measurement can be attained by utilizing a gyro together with an accelerometer.

The communication between the sensory part and actuator was established by employing two boards, the transmitter and reciever, which talk to each other through bluetooth communication.

The knowledge-based system proposed herein to generate knee torques considers the uncertainty of inputs. Different types of Fuzzy Inference Systems (Mamdani and TSK) were tried for the desired control framework and analysis comparisons were provided. The designed TSK FIS that takes advantage of ANFIS showed a better performance than the Mamdani one to control the knee torque as a function of echoing the angular state of the able leg. However, the designed Mamdani FIS was more robust. Therefore, to increase the robustness of the designed TSK FIS against the newly introduced test data, saturation blocks and PPB were offered to the control system.

8.2 Future Works

The primary fabricated APK prototype is in the testing stage. As future developments continue to improve the APK, the following directions can be helpful. The

recommendations mentioned here fall into two groups: i) low level tasks, which are suggested to improve and expand the current APK, ii) high level tasks, which are proposed to develop a new APK based on the experience gained during this work on the current APK.

8.2.1 Low-Level Tasks

Future directions for enhancing the performance of the current system include the following:

1) The motion of the ball-screw is restricted by the microcontroller only for the current prototype. To secure the ball-screw and thus the APK, a false detector must be added to the system. Many electro-mechanical mechanisms such as roller limit switches or optic/laser sensors can provide the required functionality.

2) Test-bed modification for the pelvic simulator is required to provide a perfect imitation of the gait cycle, specifically the sinusoidal motion of the pelvis. This purpose can be achieved by utilizing a piston-crank mechanism actuated by an electromotor. However, one separated controller will be required for the stated mechanism.

3) The current microcontroller is programmed based on the potentiometer together with the accelerometer; however, a more promising sensing method is addressed by utilizing a gyroscope together with an accelerometer. Unfortunately, there was not enough time to update the controller code based on the later method. Prospective students are strongly recommended to upgrade the correlated program.

4) The uncertainty of Gaussian input membership functions, due to the uncertainty about the definition of slow, normal, and fast cadence, must be consider since different words mean different things to different people. In other words, the uncertainty in the cluster data is considered; however, the uncertainty about the nature of the clusters has not been taken into account. This approach will lead to

an upper and a lower bond for the defined Gaussian input membership functions, and the created system called type-2 FIS (Mamdani or TSK). This uncertainty can increase the credibility of the model.

5) The current knowledge-based system must be advanced to provide a controller for other arbitrary activities such as sitting, standing, and etc.

6) Finally, after all experimentation is complete and the safety validation is attained, human testing is required to verify feasibility of the research.

8.2.2 High-Level Tasks

Recommendations to improve the current prototype were discussed in the low-level tasks; this section suggests a novel design of a semi-active semi-passive prosthetic knee. This prosthesis exploits the four-bar (polycentric) knee design incorporating a linear electromagnetic motor/generator. However, the similar method of control, sensing system, and communication presented in the previous chapters can be utilized for the last-proposed knee.

The main deficiency of the active/semi-active prosthetic knee, presented in prior works, is the amount of energy required for its operation. As a result, the power source is bulky, depletes quickly and adds significant weight to the system.

This section suggests using a linear electromagnetic actuator in an active knee mechanism to improve the system's power efficiency. The actuator converts physiological energy to electrical energy during one part of the gait cycle preventing its dissipation. It then uses this saved energy during another part of the gait cycle for actuation. In commercialized polycentric prosthetic knees, the actuator and hydraulic/pneumatic damper are two separated units, whereas the proposed linear motor provides the same functionality in a single package.

As described, in the first chapter-back ground section, each stride represents one gait cycle and is divided into two periods: stance and swing (Figure 1-4). Stance is the period

119

when the foot is in contact with the ground, and swing is the period when the foot is in the air. The stance phase is divided into four phases: initial double support, mid-stance, terminal stance, and second double support. The swing period can be subdivided into three phases. Initial swing, mid-swing, and terminal swing. The initial limb support is characterized by a very rapid weight acceptance onto the forward limb with shock absorption and slowing of the body's forward momentum. Mid-stance and terminal-stance are involved in the task of single limb support, when the knee is locked. Limb advancement is performed during the pre-swing phase and throughout the first two sub-phases of the swing period, while an actuation force is required. In the terminal swing, the limb is decelerated and finally strikes the ground for the second time, so damping force is needed during this stage. As a result, damping action is only essential during the first and last phases of the gait cycle.

Four-bar linkage knees make up the majority of prosthetic knees (Figure 8-1). Through different designs and linkage geometries, these knees provide varying level of stability. Commercialized 4-bar knees such as: Total Knee 2100 (Össur hf.), TK-4P0C (Teh-Lin Prosthetic Co.), and 1M12 (Proeteor Group) utilize hydraulic damper, pneumatic damper, and mechanical friction, respectively, to provide the resistive torque. These prostheses are not intelligent, and the level of damping is adjusted manually.

Conversely, in a microcontroller based semi-passive knee joint, the controller varies the resistive torque provided by a hydraulic, pneumatic, or Magneto-Rheological (MR) damper by means of a servo valve. Further details of semi-passive knees were presented in Section 1.4.1 (Passive Knees). The existence of a low level stiffness in all phases of gait cycle is the main disadvantage of hydraulic based knees. Moreover, physiological energy is dissipated without being used. MR dampers are prone to degradation of the MR fluids and sealant failure. The high cost of MR fluids is the other problem of associated knees.

There have been just few efforts to develop a self energizing prosthetic knee. Wang et al [18] proposed a hydraulic system, which compresses the fluid in an accumulator during

stance, and then energizes and controls the knee during swing by using a needle valve. The problems of low efficiency and large size are the main flaws of the aforementioned system. Andrysek et al [45] developed a rotary electromagnetic generator for a four-bar linkage knee to harvest energy during swing phase. However, this system was passive and in the case of using the generator as an actuator (motor), a gearbox, or another linkage mechanism, is needed to convert the rotary to linear motion.
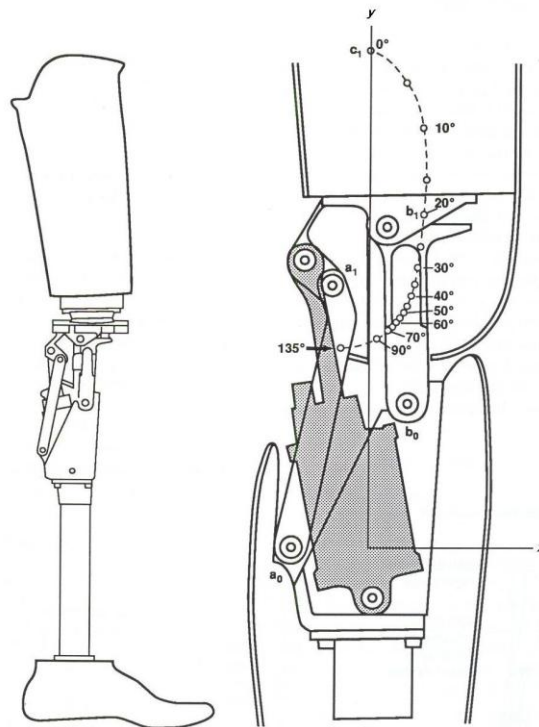
Figure 8-1: Four-bar linkage knee mechanism and its path of instant center of rotation.

The use of electromagnetic linear actuators is an alternative implementation for the active four-bar prosthetic knee, which has the advantage of energy recovery. An active suspension prosthetic knee has the ability to dissipate, store and, introduce, energy to the system.

Some authors have proposed linear electric power generators by means of electromagnetic motors. Merritt et al [46] proposed a linear electrical generator with a reciprocating armature with rectangular permanent magnets, which were coupled to a source of relative motion. The device does not appear to fully utilize the magnetic field

generated by the permanent magnets, since the generator uses only single magnetic pole-coil interaction, which causes the efficiency reduction of the device. Konotchick [47] proposed several designs of linear electric power generators consisting of a cylindrical assembly of rare earth magnets (NdFeB) and coils positioned to move reciprocally relative to each other. The device is most likely designed for relatively large amplitude motions such as wave energy generation. Goldner and Zerigian [48] proposed a new assembly of magnet and coil winding arrays to maximize the radial magnetic flux density in a linear generator acting as a shock absorber. The damper does not appear to be controlled actively.

Figure 8-2 depicts the schematic view of the proposed electromagnetic shock absorber. The novel linear motor functions as position sensor and actuator simultaneously. The spring effect can be added to the system by means of electromagnets and permanent magnets. Moreover, electromagnetic motors can work under very low static friction. In addition, the damping coefficient is controlled rapidly and reliably through electrical manipulations.
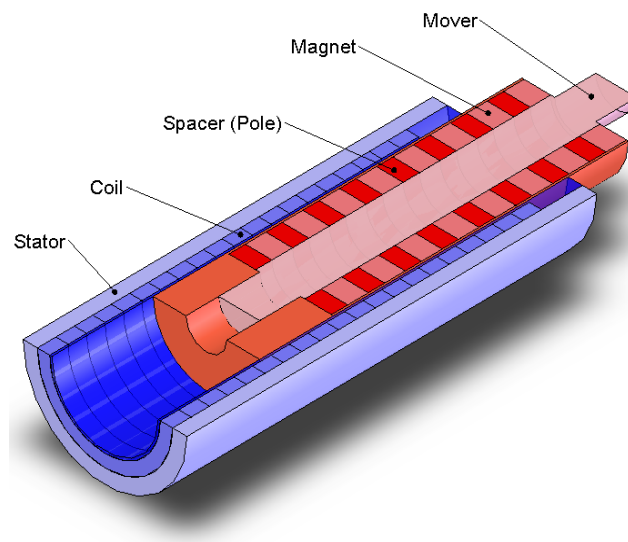
Figure 8-2: The schematic view of the proposed damper.

This proposal utilizes magnetic circuit principles to optimally design a regenerative electromagnetic motor. The damper is also cost-effective, using several permanent magnets in combination with electromagnets as its major components, and a straightforward fabrication process. Utilizing a linear motor simplifies the mechanical design and eliminates the complex process of linear-to-rotary motion. The assembly is comprised of a tubular design as shown in Figure 8-2, which has less leakage flux and vastly is better in utilizing the magnetic flux, leading to higher electromotive force (in generator mode) and a higher thrust force (in motor mode). Axially magnetized permanent magnets in the mover allow for a higher force to volume ratio than radially magnetized ones.

The proposed linear electromagnetic motor/generator provides the required damping force, harvesting the dissipated energy, and supplies the force required to flex/extend the leg in the limb advancement task.

REFERENCES

[1]   Cairo, A.; "Orthopaedic Project in Afghanistan", The International Committee of the Red Cross (ICRC) Geneva, Fact Sheet, 2005.

[2]   Machel, G.; "Impact of armed conflict on children- Land-mines: A deadly inheritance," United Nations Department for Policy Coordination and Sustainable Development (DPCSD) and UNICEF, 1996.

[3]   Lim, J.; "The Mechanical Design and Analysis of an Active Prosthetic Knee," Master of Applied Science thesis, University of Waterloo, Ontario, Canada, May 2008.

[4]   (2008) Human Anatomy Online website. [Online]. Available: http://www.innerbody.com/htm/body.html

[5]   (2008) [Online]. Available: http://training.seer.cancer.gov/module_anatomy/unit1_3_terminology2_planes.html

[6]   Rose, J.; Gamble, J.G.; "Human Walking," 3rd ed., Philadelphia: Lippincott Williams & Wilkins, 2005.

[7]   (2008) [Online]. Available: http://www.univie.ac.at/cga/history/modern.html

[8]   Winter, D.; "Biomechanics and motor control of human movement," 3rd ed., John Wiley & Sons Inc., 2005.

[9]   (2008) Otto Bock Healthcare [Online]. Available: http://www.ottobock.com

[10] Peizer, E.; Wright, D. W.; "Human Locomotion," 1969.

[11] Zlatnik, D.; Steiner, B.; Schweitzer, G.; "Finite-State Control of a Trans-Femoral (TF) Prosthesis," IEEE Transaction on Control Systems Technology, vol. 10, no. 3, pp. 408-420, May 2002.

[12] Carlson, J.D.; Matthis, W.; Toscan, J.R.; "Smart prosthetics based on magnetorheological fluids," Proceedings of SPIE'01: The International Society for Optical Engineering, vol. 4332, pp. 308-316, 2001.

[13] Kim, C.; Lee, J.; Xu, X.; "Design of biped robot with heterogeneous legs for advanced prosthetic knee application," SICE-ICASE International Joint Conference, pp. 1852-1855, 2006.

[14] Flowers, W. C.; Mann, R. W.; "Electro-hydraulic knee-torque controller for a prosthesis simulator," ASME Journal of Biomechanical Engineering, vol. 99, no.4, pp. 3–8, 1977.

[15] Stein, J. L.; Flowers, W. C; "Stance phase control of above-knee prostheses: knee control versus SACH foot design," Journal of Biomechanics, vol. 20, no.1, pp. 19–28, 1988.

[16] Sup, F.; Bohara, A.; Goldfarb, M.; "Designed and Control of a Powered Transfemoral Prosthesis," The International Journal of Robotics Research, vol. 27, no. 2, pp. 263-273, Feb. 2008.

[17] Buckley J.G.; Spence W.D.; Solomonidis S.E.; "Energy cost of walking: comparison of "Intelligent Prosthesis" with conventional mechanism," Archives of Physical Medicine and Rehabilitation, vol. 78, no.3, pp. 330-33, 1997.

[18] Wang, T. K.; Ju. M. S.; Tsuei, Y. G.; "Adaptive control of above knee electro-hydraulic prosthesis," Journal of Biomechanical Engineering, vol. 114, issue 3, pp. 421-424, 1992.

[19] Saito, Y.; Kikuchi, K.; Negoto, H.; Oshima, T.; Haneyoshi, T.; "Development of externally powered lower limb orthosis with bilateral-servo actuator," Proceedings of ICORR 2005: IEEE 9th International Conference on Rehabilitation Robotics, pp. 394 – 399, 2005.

[20] Sawicki, G.S.; Gordon, K.E.; Ferris, D.P.; "Powered lower limb orthoses: applications in motor adaptation and rehabilitation," Proceedings of ICORR 2005: IEEE 9th International Conference on Rehabilitation Robotics, pp. 206- 211, 2005.

[21] Kapti, A. O.; Yucenur, M. S.; "Design and control of an active artificial knee joint," Mechanism and Machine Theory, vol. 41, no. 12, pp. 1477-1485, 2006.

[22] Popović D.; Oguztöreli, M. N.; Stein, R. B.; "Optimal control for an above-knee prosthesis with two degrees of freedom," Journal of Biomechanics, vol. 28, no. 1, pp. 89-98, 1995.

[23] Shigley, J. E.; Mischke, C. R.; "Mechanical Engineering Design," 6th ed., Boston, MA, McGraw Hill, 2001.

[24] Molian, S.; "Mechanism design: an introductory text," Cambridge, Cambridge University Press,1982.

[25] Asada, H.; Slotine, J.-J. E.; "Robot Analysis and Control," New York, NY, USA, John Wiley & Sons Inc., 1986.

[26] Lee, S.; Sankai, Y.; "Power assist control for leg with HAL-3 based on virtual torque and impedance adjustment," Proceedings of SMC'02: IEEE International Conference on Systems, Man and Cybernetics, vol. 4, Oct. 2002.

[27] (2008) [Online]. Available:
http://academic.wsc.edu/faculty/jatodd1/351/ch6outline.html

[28] Shiavi, R.; Bugle, H. J.; Limbird, T.; "Electromyographic gait assessment, part 1: Adult EMG profile and walking cycle," Journal of Rehabilitation Research & Development, vol. 24, pp. 13-23, 1987.

[29] Hof, A. L.; Pronk, C. N. A.; Van Best, J. A.; "Comparison between EMG to force processing and kinetic analysis for calf muscle moment in walking and stepping," Journal of Biomechanics, vol. 20, pp. 167-178, 1987.

[30] Inman, V.T.; Ralston, H. J.; Saunders, J. B.; Feinstein, B.; Wright, E. W.; "Relation of human electromyogram to muscular tension," EEG & Clin. Neurophysical. 4:187-194, 1952.

[31] Winter, D. A.; "The Biomechanics and motor control of human gait: Normal, Elderly, and Pathological," 2nd ed., Waterloo, ON, Canada, University of Waterloo Press, 1991.

[32] Dejnabadi, H.; Jolles, B. M.; Aminian, K.; "A New Approach to Accurate Measurement of Uniaxial Joint Angles Based on a Combination of Accelerometers and Gyroscopes," IEEE Transactions on Biomedical Engineering, vol. 52, no. 8, pp. 1478- 1484, Aug. 2005.

[33] Popovic, D.; Oguztoreli, M. N.; Stein, R. B. "Optimal control for an above-knee prosthesis with two degrees of freedom," Journal of Biomechanics, vol. 28, issue 1, pp. 89–98, 1995.

[34] Aeyels, B.; Peeraer, L.; Vander Sloten, P.; Van der Perre, G.; "Development of an above-knee prosthesis equipped with a microcomputer controlled knee joint: First test results," Journal of Biomedical Engineering, vol. 14, pp. 199–202, May 1992.

[35] Tsai, C. S.; Mansour, J. M.; "Swing phase simulation and design of above knee rosthesis," Journal of Biomechanics Engineering, vol. 108, pp. 65–72, Feb. 1986.

[36] Wang, T. K.; Ju, M. S.; Tsuei, Y. G. "Adaptive control of above knee electro-hydraulic prosthesis," Journal of biomechanics engineering, vol. 114, pp. 421–424, Aug. 1992.

[37] Mendel, J. M.; "Fuzzy Logic Systems for Engineering: A Tutorial," Proceedings of the IEEE, vol. 83, pp. 345-377, March 1995.

[38] Zadeh, L.A.; "Fuzzy sets," Information and Control, vol. 8, pp. 338-353, 1965.

[39] Zimmermann, H. J.; "Fuzzy Theory and Its Applications," 2nd ed., Boston, MA, Kluwer Academic Publication, 1991.

[40] Mamdani, E. H.; Assilian, S.; "An experiment in linguistic synthesis with a fuzzy logic controller," International Journal of Man-Machine Studies, Vol. 7, No. 1, pp. 1-13, 1975.

[41] Sugeno, M.; Kang, G. T.; "Structure identification of fuzzy model," Fuzzy Sets Systems, vol. 28, pp. 15-33, 1988.

[42] Kosko, B.; "Neural Network and Fuzzy Systems: A Dynamical Systems Approach to Machine Intelligence," Englewood Cliffs, New Jersey, Prentice Hall, 1992.

[43] Mouzouriz, G. C.; Mendel, J. M.; "Non-Singleton Fuzzy Logic Systems: Theory and Applications," IEEE Transaction on Fuzzy Systems, vol. 5, pp. 56-71, Feb. 1997.

[44] Jang, J.-S. R.; "ANFIS: Adaptive-Network-based Fuzzy Inference Systems," IEEE International Conference on Systems, Man and Cybernetics, vol. 23, no. 3, pp. 665-685, May 1993.

[45] Andrysek, J.; Chau, G.; "An electromechanical swing-phase-controlled prosthetic knee joint for conversion of physiological energy to electrical energy: feasibility study," IEEE Transaction on Biomedical Engineering, vol. 54, no.12, pp. 2276-83, Dec. 2007.

[46] Merritt, T. D.; Pasichinskyj, M. J.; "Linear reciprocating electrical generator," US. Patent no. 4500827, 1985.

[47] Konotchick, J. A.; "Linear motion electric power generator," US. Patent no. 5347186, 1994.

[48] Goldner, R. B.; Zerigan, P.; "Electromagnetic linear generator and shock absorber," US. Patent no. 6952060, 2005.